**POLYTECHNIQUE MONTRÉAL**
affiliée à l'Université de Montréal

# Advancement in Biomedical Imaging through the Development of Photonic Lanterns: A Study on Light-Matter Interactions

**MARTIN POINSINET DE SIVRY-HOULE**
Département de génie physique

Thèse présentée en vue de l'obtention du diplôme de *Philosophiæ Doctor*
Génie physique

Mars 2024

© Martin Poinsinet De Sivry-Houle, 2024.

**POLYTECHNIQUE MONTRÉAL**
affiliée à l'Université de Montréal

Cette thèse intitulée :

**Advancement in Biomedical Imaging through the Development of Photonic Lanterns: A Study on Light-Matter Interactions**

présentée par **Martin POINSINET DE SIVRY-HOULE**
en vue de l'obtention du diplôme de *Philosophiæ Doctor*
a été dûment acceptée par le jury d'examen constitué de :

**Frédéric LEBLOND**, président
**Caroline BOUDOUX**, membre et directrice de recherche
**Nicolas GODBOUT**, membre et codirecteur de recherche
**Sean MOLESKY**, membre
**Hongki YOO**, membre externe

# DEDICATION

*This journey, albeit solitary, has been a testament to the fact that sometimes the best guidance comes from within. A tip of the hat to my colleagues and friends, the unofficial committee of moral support and comic relief. Here's to the silent nods of understanding, the shared groans over failed experiments, and the collective eye-rolls at academic hurdles. You've been the unsung heroes in the footnotes of this quest.*

# ACKNOWLEDGEMENTS

This thesis marks the culmination of an intense period of research and personal growth. While the journey has been uniquely mine, there are acknowledgements to be made for the support and contributions that have mitigated the laborious completion of this work.

I extend my gratitude to the lab colleagues, whose camaraderie and shared dedication to our collective scientific endeavors have provided a stimulating and enriching work environment. The discussions, debates, and witty (or not so) jokes have enhanced my research and made the daily challenges more manageable and often enjoyable. Your expertise, willingness to assist, and mutual respect have been invaluable.

On a personal note, this thesis also represents a journey of individual perseverance and self-discovery. It has been a testament to the idea that progress and fulfillment can be found even in solitude and despite adversities.

This thesis would not have been possible without the environment and the individuals who, in various capacities, have contributed to its completion. For that, I am thankful.

# RÉSUMÉ

Cette thèse doctorale présente le développement et l'application des lanternes photoniques pour générer des champs lumineux structurés et leur utilisation dans des applications d'imagerie biomédicale. Les lanternes photoniques, une classe de composante de fibre optique, ont traditionnellement été considérées comme des outils puissants en télécommunication et astronomie ; pourtant leur potentiel d'application à l'imagerie biomédicale a été largement sous-exploré. Cette thèse met en lumière les capacités de transformation et d'innovation offertent par les lanternes photoniques modallement spécifique, une sous-classe spécialisée de lanternes photoniques présentant des attributs intéressants tels que l'invariance en longueur d'onde sur une large bande passante et une correspondance un-à-un avec les modes linéairement polarisés (LP) de la fibre optique.

Des études récentes ont montré la promesse d'exploiter divers modes de propagation des fibres multimodes pour déverrouiller de nouveaux mécanismes de contraste, marquant un changement émergent dans le domaine. Cependant, ces efforts pionniers n'en sont qu'à leurs débuts, puisque ne disposant pas de contrôle modal efficace des modes de propagation de la fibre ni d'un modèle robuste expliquant le mécanisme de contraste sous-jacent.

Pour combler ces lacunes, je propose une exploration complète de l'intégration verticale d'une lanterne photonique spécifiquement modale récemment conçue. Le travail de recherche a commencé par la conceptualisation théorique de la lanterne photonique spécifiquement modale, progressant vers sa fabrication méticuleuse, et a culminé dans le développement d'un modèle robuste pour comprendre les mécanismes de contraste. Pour étayer nos intuitions théoriques, nous présentons également la mise en œuvre expérimentale de la lanterne photonique spécifiquement modale dans un cadre d'un système de tomography par cohérence optique (OCT, de l'anglais "optical coherence tomography").

Un examen critique de la littérature existante constitue un élément essentiel de cette thèse. Il examine l'histoire et le développement des lanternes photoniques, leur utilisation dans les télécommunications, et les tentatives préliminaires de les utiliser en imagerie biomédicale. Cet examen met en évidence les lacunes dans la base de connaissances actuelles, notamment dans la compréhension et le contrôle des modes de propagation et le développement d'un modèle de mécanisme de contraste complet. Cette exploration prépare le terrain pour l'introduction de la lanterne photonique spécifiquement modale et souligne la nécessité de ce travail.

Dans la première partie de cette thèse, nous introduisons "SuPyMode", un logiciel complet développé pour la conception de composants en fibre optique. SuPyMode permet l'analyse

et la conception détaillées de composants en fibre optique fusionnés et coniques, y compris les lanternes photoniques spécifiquement modales. La bibliothèque montre comment la fibre optique structurée peut conduire à la fabrication de composants plus robustes, réduisant le couplage modale et les pertes, qui sont des considérations clés en imagerie biomédicale et en détection où le maintien d'un rapport signal sur bruit élevé est primordial.

La seconde partie de cette thèse se tourne vers notre nouvel outil logiciel "PyMieSim", un solveur puissant de diffusion de Mie qui intègre de manière unique le schéma de détection comme métrique de calcul. PyMieSim facilite la résolution des problèmes de diffusion de Mie pour une large gamme de paramètres définissant la triade source-diffuseur-détecteur. En utilisant cette bibliothèque, nous explorons le mécanisme de contraste offert par les schémas de détection cohérente, tels que les modes de propagation de fibre optique. Ce travail de fond nous a permis de développer un modèle de contraste robuste pour l'imagerie biomédicale utilisant des lanternes photoniques spécifiquement modales. En particulier, notre modèle démontre que la détection de diffuseurs uniques de dimensions inférieures à la résolution du système est réalisable en utilisant les champs structurés des modes de propagation de fibre optique.

Dans la troisième partie de cette thèse, nous présentons une validation expérimentale de notre modèle développé grâce à l'incorporation d'une lanterne photonique spécifiquement modale dans un système d'OCT. Les résultats présentés mettent en évidence un mécanisme de contraste sur les diffuseurs uniques en fonction de leurs propriétés géométriques, et valident surtout le comportement général de l'interaction de la lumière structurée avec les échantillons biologiques. Cette validation expérimentale conforte nos hypothèses théoriques, illustrant le potentiel de l'approche des lanternes photoniques spécifiquement modales dans des scénarios d'imagerie biomédicale pratiques.

Les révélations découvertes à travers ce travail suggèrent l'immense potentiel des lanternes photoniques spécifiquement modales pour, à la fois, enrichir notre compréhension des interactions lumière-matière, et pour faire avancer de manière significative les capacités de la technologie d'imagerie biomédicale. Cette thèse représente une étape importante, fournissant la pierre angulaire pour la recherche future dans l'exploitation des lanternes photoniques, spécifiquement des lanternes photoniques spécifiquement modales, pour les futures applications biomédicales. Les conclusions ici ouvrent la porte à une amélioration de la résolution, du contraste et de la profondeur de l'imagerie, promettant d'améliorer considérablement la précision du diagnostic et de potentiellement transformer les soins aux patients dans le domaine médical.

Dans l'ensemble, cette thèse établit la base pour le développement et l'utilisation de lan-

ternes photoniques dans la génération de champ lumineux structurés pour les applications d'imagerie biomédicale. Les résultats de la recherche contribuent au domaine de l'imagerie lumineuse structurée et procurent des perspectives précieuses pour les avancées futures dans les techniques d'imagerie biomédicale.

# ABSTRACT

This doctoral thesis presents the development and application of photonic lanterns for generating structured light fields and their utilization in biomedical imaging applications. Photonic lanterns (PLs) have traditionally been regarded as powerful tools in the telecommunication and astronomy spaces, yet their potential for application within biomedical imaging has been vastly underexplored. This thesis elucidates the capacity for transformation and innovation offered by modally-specific photonic lanterns (MSPLs), a specialized subclass of photonic lanterns exhibiting interesting attributes such as wavelength independence across an extensive bandwidth and a one-to-one mapping with fiber optic linearly-polarized (LP) modes.

Recent studies have shown promises in harnessing various propagation modes of multi-mode fibers (MMFs) to unlock new contrast mechanisms, marking an emergent shift in the field. However, these pioneering efforts remain in their infancy, lacking in efficient modal control of fiber propagation modes and lacking a robust model delineating the underlying contrast mechanisms.

Addressing these gaps, this work provides a comprehensive exploration into the vertical integration of a newly designed MSPL. This research journey commenced with the theoretical conceptualization of the MSPL, progressing towards its meticulous manufacture, and culminated in the development of a robust model to understand the contrast mechanism it enables. To substantiate our theoretical insights, we also present experimental implementation of the MSPL within an optical coherence tomography (OCT) framework. A critical review of the existing literature forms an essential component of this thesis. It examines the history and development of PLs, their use in telecommunications, and the preliminary attempts to utilize a similar techniques in biomedical imaging. This review uncovers gaps in the current knowledge base, particularly in the understanding and control of propagation modes and the development of a comprehensive contrast mechanism model. This exploration sets the stage for the introduction of the MSPL and underlines the necessity of this work.

In the first part of this thesis, I introduce "SuPyMode", a comprehensive software developed for designing fiber optics components. SuPyMode permits the intricate analysis and design of fused and tapered fiber optics components, including MSPLs. The library showcases how peculiar fiber optics structure can lead to the fabrication of more robust components, reducing modal cross-talk and losses, which are key considerations in biomedical imaging and sensing where maintaining a high signal-to-noise ratio (SNR) ratio is paramount.

The second part of this thesis pivots on our novel software tool "PyMieSim", a powerful Mie

scattering solver that uniquely incorporates the detection scheme as a computation metric. PyMieSim facilitates solving Mie scattering problems for a broad range of parameters defining the source-scatterer-detector triad. Employing this library, we explore the contrast mechanism offered by coherent and structured detection schemes, such as fiber optic propagation modes. This deep dive allowed us to develop a robust contrast model for biomedical imaging using MSPLs. In particular, our model paves the way for sub-resolution single scatterer sensing is achievable using the structured fields of fiber optic propagation modes.

In the third part of this thesis, we present experimental validation of our model through the incorporation of a MSPL into an OCT system. The presented results highlight a unique contrast on single scatterers based on their geometrical properties, and importantly, validate the general behavior of structured light interactions with biological samples. This experimental validation lends credence to our theoretical developments, illustrating the potential of the MSPL approach in practical biomedical imaging scenarii.

The revelations uncovered through this work suggest a great potential for MSPLs to not only enrich our understanding of light-matter interactions, but also to significantly advance the capabilities of biomedical imaging technology. This thesis stands as a milestone, providing a stepping stone for further research exploiting PLs, specifically MSPLs, for future biomedical applications. The findings herein illuminate the path towards enhanced imaging resolution and contrast mechanism, holding substantial promise for improving diagnostic accuracy and potentially transforming patient care in the medical field.

Overall, this thesis establishes the foundation for the development and utilization of PLs in generating structured light fields for biomedical imaging applications. The research findings contribute to the field of structured light imaging and offer valuable insights for future advancements in biomedical imaging techniques.

# TABLE OF CONTENTS

DEDICATION . . . . . iii

ACKNOWLEDGEMENTS . . . . . iv

RÉSUMÉ . . . . . v

ABSTRACT . . . . . viii

TABLE OF CONTENTS . . . . . x

LIST OF TABLES . . . . . xiv

LIST OF FIGURES . . . . . xv

LIST OF SYMBOLS AND ACRONYMS . . . . . xxi

LIST OF APPENDICES . . . . . xxiii

CHAPTER 1 INTRODUCTION . . . . . 1
- 1.1 Background . . . . . 1
- 1.2 Problem Statement . . . . . 2
- 1.3 Objective of the Research . . . . . 3
- 1.4 Thesis Outline . . . . . 4

CHAPTER 2 LITERATURE REVIEW . . . . . 7
- 2.1 Photonic Lanterns : Development and Applications . . . . . 7
- 2.2 Structured Light Fields : Harnessing Complex Light . . . . . 9
- 2.3 Optical Coherence Tomography : A Powerful Imaging Modality . . . . . 10
- 2.4 Mie Scattering : A Key Physical Process . . . . . 11

CHAPTER 3 ARTICLE 1 : SUPYMODE : AN OPEN-SOURCE LIBRARY FOR DESIGN AND OPTIMIZATION OF FIBER OPTIC COMPONENTS . . . . . 13
- 3.1 Author Contribution . . . . . 13
- 3.2 Chapter Context . . . . . 13
- 3.3 Introduction . . . . . 14
- 3.4 The Library . . . . . 15

3.4.1 Code Architecture . . . 15
3.4.2 Compute Time Optimization . . . 15
3.4.3 User Interface . . . 17
3.5 Theory . . . 17
3.5.1 Fiber Coupler Structure . . . 17
3.5.2 Eigenmodes Expansion . . . 19
3.5.3 Coupled-Mode Theory . . . 20
3.5.4 Validation . . . 22
3.6 Applications . . . 24
3.6.1 Mode-Specific Photonic Lantern Design . . . 24
3.6.2 Mode Skipping . . . 27
3.7 Discussion . . . 29

CHAPTER 4 DESIGN OF PHOTONIC LANTERNS COMPONENT USING SUPYMODE, AN OPEN-SOURCED PYTHON LIBRARY . . . 31
4.1 Chapter Context . . . 31
4.2 Introduction . . . 31
4.3 Method . . . 32
4.4 Photonic Lantern Design . . . 33
4.5 Conclusion . . . 35

CHAPTER 5 ARTICLE 2 : PYMIESIM : AN OPEN-SOURCE LIBRARY FOR FAST AND FLEXIBLE FAR-FIELD MIE SCATTERING SIMULATIONS . . . 36
5.1 Author Contribution . . . 36
5.2 Chapter Context . . . 36
5.3 Introduction . . . 37
5.3.1 Lorenz-Mie Theory Applications . . . 38
5.4 Theory . . . 39
5.4.1 Optical Setup . . . 39
5.4.2 Lorenz-Mie Theory . . . 40
5.4.3 Scattering Properties . . . 42
5.4.4 Coupling Mechanism . . . 42
5.5 Main features of PyMieSim . . . 44
5.5.1 Architecture . . . 44
5.5.2 Compute Time . . . 44
5.5.3 User Interface . . . 47
5.6 Validation . . . 47

5.7 Application . . . . . 48
5.7.1 Flow-Cytometry Optimization . . . . . 48
5.7.2 Coherent Imaging Analysis . . . . . 52
5.8 Conclusion . . . . . 52

CHAPTER 6 ARTICLE 3 : ALL-FIBER FEW-MODE OPTICAL COHERENCE TOMOGRAPHY USING A MODALLY-SPECIFIC PHOTONIC LANTERN . . . . 57
6.1 Author Contribution . . . . . 57
6.2 Chapter Context . . . . . 57
6.3 Introduction . . . . . 58
6.4 Contrast mechanism . . . . . 59
6.4.1 Coupling model . . . . . 60
6.4.2 Coupling mechanism in a biological tissue . . . . . 64
6.5 Materials and methods . . . . . 67
6.5.1 Photonic lantern design . . . . . 67
6.5.2 Optical system . . . . . 67
6.5.3 Data acquisition and post-processing . . . . . 68
6.5.4 Sample preparation . . . . . 69
6.6 Results . . . . . 69
6.6.1 Modally-specific photonic lantern validation . . . . . 70
6.6.2 Phantom imaging . . . . . 71
6.6.3 Rat lung imaging . . . . . 72
6.7 Discussion . . . . . 72

CHAPTER 7 STRUCTURED FIELD INTERACTION WITH TURBID MEDIA : A STUDY THROUGH THE LENS OF THE BORN APPROXIMATION . . . . . 78
7.1 Chapter Context . . . . . 78
7.2 Introduction . . . . . 78
7.2.1 Light Field Generation . . . . . 79
7.2.2 Born Approximation . . . . . 79
7.2.3 Modeling of Turbid Media . . . . . 83
7.3 Coupling Mechanism . . . . . 85
7.3.1 Model predictions . . . . . 88
7.3.2 Challenges and Future Directions . . . . . 89

CHAPTER 8 GENERAL DISCUSSION . . . . . 90
8.1 Achievement of Research Objectives . . . . . 90

8.1.1 Fiber Component Software and Hardware Design . . . . . 90
8.1.2 Structured Light-Field and Matter Interaction . . . . . 91
8.1.3 Experimental Validation . . . . . 92
8.2 Ongoing and Future Research . . . . . 93
8.2.1 Manufacturing Higher-Order Modes MSPLs . . . . . 93
8.2.2 Modeling Light-Tissue Interaction . . . . . 93
8.2.3 Toward Super-Resolution . . . . . 94

CHAPTER 9 CONCLUSION . . . . . 96
9.1 Summary of Work . . . . . 96
9.2 Outlook . . . . . 97

REFERENCES . . . . . 98

APPENDICES . . . . . 113

# LIST OF TABLES

Table 3.1: Fiber models, used for the design optimization. The double-clad fiber (DCF) fibers were also used in [33] and graded-index fiber (GIF) are extracted from [160]. . . . . 26

Table 5.1: Scattering parameters computed by PyMieSim for spherical particles. PyMieSim also computes scattering parameters for infinite cylinders using equations found in [22] and reproduced in [126], but not included here for conciseness' sake. . . . . 43

Table 5.2: Features of open source Lorenz-Mie scattering theory (LMT) packages. Features were deduced from an in-depth analysis of each project. . . 55

# LIST OF FIGURES

Figure 1.1: Thesis structure . . . . . 6

Figure 2.1: Depiction of a coupler manufacturing station. (a) Picture of the fusion station setup. Highlighted in red is the flame nozzle, in yellow the pulling section, on which lies the fused fiber structure. (b) Schematic of the main components of the manufacturing process . . . . . 8

Figure 3.1: Illustration of the architectural arrangement and user interface of the SuPyMode library. (a) Depiction of the structure, pipeline, and computing capabilities of the library. The entire definition of the optical structure is comprised in the FiberFusing package. The entire data-extraction pipeline is encompassed in the workflow framework. (b) Code snippet for 2x2 asymmetric coupler simulation using the aforementioned workflow framework. The considered design employs two different fibers (SMF28 and HP630) to break the *top-bottom* symmetry, enabling the lifting of mode degeneracy. . . . . 16

Figure 3.2: Depiction of an optical coupler model in transverse (a) and longitudinal (b) sections. (a) Four predefined transverse profiles with, from left to right, 2, 3, 4, and 7 fibers, with the location of the core in black and the cladding in blue, for two degrees of fusion : 0.3 (top row) and 0.8 (bottom row), where 0 corresponds to the fibers adjacent to one another and 1 corresponds to a complete fusion. Longitudinal profile of a 2×2 structure (b) with a taper corresponding to the manufacturing process defined in [153]. The red dotted lines correspond to the selected cross-sections used for eigenmode computation. Insets show cross-sections at the locations indicated by the black arrows, with a degree of fusion of 0.8. . . . . 18

Figure 3.3: Profile (a), adiabatic criterion (b), and ITR (c) of a 4x4 hybrid coupler. (a) The section shows 4 fibers placed in a glass capillary with a degree of fusion of 0.8. (b) Adiabatic criterion of for the computed modes. The black dotted lines represent the coupling factor for coupler profiles computed for different initial heating length ranging from 2 mm to 20 mm. The simulated heat-processing time is 1600 seconds and the alpha parameter (defined as the rate of change of the heating length [153]) is zero. (c) Representation of the coupler inverse taper ratio (ITR) as a function of the propagation direction. . . . . 21

Figure 3.4: Comparison of simulated and analytical results for propagation constant (a), normalized coupling (b), field distribution at ITR of 1.0 (c) and 0.3 (d) of a single SMF28$^{TM}$ fiber taper. . . . . 23

Figure 3.5: Design of a 2x1 MSPL based on an A-B structure using SuPyMode. (a) The configuration of the simulated structure highlights the position of each of the fibers : Fiber A and Fiber B. (b) The field structure of the computed modes. For visualization purposes, only four modes are depicted here. (c) The adiabatic criterion of the taper structure. The blue area represents a standard in-lab feasible region with coupler length varying from 1 mm to 30 mm. Comparison of the different 2x1 MSPL designs using fibers from Table 3.1. (a) Adiabatic curves for each design in the ITR region ranging from 0.05 to 0.4. (b) Comparison of the minimum adiabatic values in the same region. The higher the figure, the more robust the component to modal cross-talk. . . 25

Figure 3.6: Depiction of the mode-skipping process. (a) 2x1 asymmetric optical structure that allows for $LP_{01}$ and $LP_{21}$ generation. (b) Depiction of the mode propagation constant and coupling behavior as a function of the ITR. The mode-leaking line separates the coupling vs. no-coupling region. The black dots on the orange curves indicate points of interest. (c) Adiabatic criterion for the optical structure, six first propagation modes. Subset (vi) highlights an avoided crossing, which signifies strong coupling, while (i-iii) are non-interacting crossings that do not account for mode-coupling as the crossing occurs before any mode-leaking can take place. . . . . 28

Figure 4.1: Fiber taper parametrization. (a) Depiction of different taper fiber profiles as a function of the heating length. (b) Adiabatic criterion of propagation mode couple and the adiabatic factor associated with each heating length. Within this subfigure, particular attention is directed towards the LP01-LP11$a$ adiabatic criterion due to its lower magnitude in comparison to other criteria. . . . . 34

Figure 4.2: Comparison of simulation and experimentation for MSPL design. (a) Simulation of the modes field for the 4-mode configuration depicted in (d) at different localization in the tapered component (MSPL) which are associated to different inverse taper ratios (ITR). The two modes dimmed are higher-order excitation of the DCFs, and are usually disregarded. (b) Experimental measurements of the mode field generated by a 3– and 4–mode MSPL ; (c, d) Optical structure employing three (and four) different DCF and an outer capillary tube for the 3– and 4–mode configurations, respectively. . . . . 35

Figure 5.1: Representation of a scattering event configuration. An incident planewave (wavelength $\lambda_0$, polarization and electric amplitude $\vec{E}_0$, and wavevector $\hat{k}$) interacts with a homogeneous spherical scatterer (diameter $d$, and index, $m_{\text{sca}}$) immersed in a medium (index $m_{\text{med}}$). The resulting scattered wave (not shown) is projected onto an incoherent detector (numerical aperture NA, and angular location $\gamma$ and $\phi$) through a polarizing filter (not shown). Alternatively, PyMieSim allows replacing the incoherent detector with a coherent detection scheme (not shown) such as a single- or few-mode optical fiber (defined as a superposition of the scattered field onto several LP propagation modes). . . . . 39

Figure 5.2: Representation of the structure and computing capabilities of the PyMieSim library, highlighting the numerous attributes defining the optical configurations. . . . . 45

Figure 5.3: Library bench-marking presenting the computing time for scattering coefficient $An$ for scatterer with refractive index (RI) of 4, size ranging from 400 to 1000 nm and a source with a wavelength of 800 nm. . . 46

Figure 5.4: Results from the scattering experiment presented in Fig. 1 with $\lambda_0 =$ 1200nm, $d = 2000$nm, and a particle composed of BK7 glass. Coupling power is evaluated for four different detector NA's displaced along the $\phi$ angle (and for $\gamma = 0$). . . . . 48

Figure 5.5: Images obtained using the PyMieSim library for scattering simulations of various scatterer sizes illuminated with a 1000 nm planewave. (a) The non-null scattering matrix element $S_1$ and $S_2$ ; (b) Scattering phase function ; (c & d) Scattering far-field in the $\hat{\phi}$ and $\hat{\gamma}$ direction, respectively. The real and imaginary parts are depicted in the right and left parts of the sub-figure ; (e) Stokes parameters defining the polarization state using I (intensity), Q (linearly polarized, 0°), U (linearly polarized, 45°) and V (circularly polarized) ; (f) Detector far-field representation for a photodiode, $LP_{01}$, $LP_{11}$ and $LP_{21}$. . . . 49

Figure 5.6: Simulation of the scattering cross-sections for an infinite cylinder as a function of diameter. The simulation parameters are chosen to replicate the results presented in Fig.(8.7 & 8.8) of [22], which are here represented by the black dashed lines. . . . . 50

Figure 5.7: Parameter space optimization for a flow-cytometry experiment. (a-b) Coupling power of scattered light with a typical flow-cytometry system composed of two orthogonal detectors : (a) detector 0 $\{\phi_0 = 0°, \gamma_0 = 0°, \text{NA} = 0.15\}$ (b) detector 1 $\{\phi_1 = 90°, \gamma_1 = 0°, \text{NA} = 0.15\}$. (c-d) Iso-contour projections of a specific scatterer measurement (RI : 1.48, diameter : 472 nm, dashed lines) with a measurement error of 5% (shaded areas) for the typical (c) and optimized (d) flow-cytometer, where optimized detectors are placed at : detector 0 $\{\phi_0 = 0°, \gamma_0 = 42.3°, \text{NA} = 0.38\}$ and detector 1$\{\phi_1 = 133.2°, \gamma_1 = 68.0°, \text{NA} = 0.38\}$, respectively. $\Delta D$ and $\Delta n$ represent the diameter and refractive index uncertainty, respectively. 51

Figure 5.8: Simulating few-mode optical coherence tomography (FM-OCT) imaging at $\lambda_0 = 930nm$ and $\Delta\lambda = 100nm$ with 3 LP modes. (a) Mean (solid lines) and standard deviation (shaded areas) of the power coupled back into each mode as a function of the scatterer diameter for LP01 (b), LP02 (c), and LP03 (d), represented in the far-field. Inset shows the overlap of the three coupling powers in the Rayleigh regime. 53

Figure 6.1: Schematic of a modally-specific photonic lantern. (a) The top single-mode fiber (SMF) LP mode, $|LP_{01}^{top}\rangle$, maps the $LP_{01}$ mode of an FMF. (b) The bottom SMF mode, $|LP_{01}^{bot}\rangle$, maps the $LP_{11+}$ mode of the FMF. Mapping from the FMF to the SMF is reciprocal. The equation shows the mapping relation with $A$ and $B$ being amplitude coefficients, and the + sign (as opposed to $\times$) represents one of the two orthogonal $LP_{11}$ mode (the two modes ($LP_{11+}$, $LP_{11_\times}$) are similarly structured but for a $\pi/2$ rotation). . . . . 59

Figure 6.2: (a, b & c) Lambert projection of simulated parallel far-field, overlap with LP modes ($LP_{01}$ : blue, $LP_{11+}$ : orange) and simulated modal footprints for scatterers of diameter 500 nm, 5 µm and 10 µm. (d) Mean modal coupling for $LP_{01}$ (blue) and $LP_{11+}$ (orange), and their ratio (black), averaged for the wavelength range of OCT ($\lambda_0 =$ 930 nm, $\Delta\lambda = 50$ nm) ; The x-axis is divided into two sections representing the two scattering regimes, Rayleigh ($\alpha < 1$) and Mie ($\alpha > 1$). . . . . 63

Figure 6.3: Theoretical prediction of modal mean coupling in liver sample $\tilde{\boldsymbol{\eta}}_{l,m}$ (blue & orange) and their ratio $\boldsymbol{\Gamma_{11+}}$ (black). . . . . 65

Figure 6.4: FM-OCT experimental setup. $R_1'$ and $R_2'$ are the free-space propagation distance, while $R_1$ and $R_2$ are the fiber propagation distances in each branch. SLD stands for superluminescent diode PC stands for polarization controller, galvo stands for galvanometer-mounted mirrors, and 3dB is for 50 :50 fiber couplers. . . . . 69

Figure 6.5: Validation of the demultiplexing scheme. (a) Optical setup consisting of the MSPL, an imaging lens and tilted mirror for illumination (left) and detection (right). (b) Theoretical (solid lines) and experimental (dashed lines) coupling efficiencies for $LP_{01}$ (blue) and $LP_{11+}$ (orange). (c) Simulated and experimental intensity profiles of the output face of the MSPL, for each mode. The asterisk highlights a notch in the left lobe of the experimental coupling $\eta_{0,1\to1,1}$. . . . . 70

Figure 6.6: FM-OCT scans of a microbead optical phantom using $LP_{01}$ (top) and $LP_{11+}$ (bottom). (a) Maximum intensity projection (MIP) of *en-face* view. (b) B-scans obtained using $LP_{01}$ and $LP_{11+}$ with enlarged insets (i & ii). (c-d) Oversampled and zoomed C-scan obtained using disperse $TiO_2$ microbeads (0.3-10 µm) and mono-disperse borosilicate glass beads (8.3 µm), respectively. Sub-figures (d) are presented with their respective logarithmic scale bars. . . . . 73

Figure 6.7: Adult rat lung imaged with FM-OCT (dB scaling). (a) B-scan of a rat lung using $LP_{01}$ (top row) and $LP_{11+}$ (bottom row). (b) *En-face* view maximum intensity projection (MIP) of a rat lung with insets (i-iv) enlarged. Inset (v), reproduced to the right, shows the speckle pattern. (c) Auto-correlation function of speckle pattern with the predicted pattern integrated of the OCT wavelength range (inset). . . . . 74

Figure 7.1: Representation of the different element composing the scattering setup. 82

Figure 7.2: (a) Scattered far-field for a $\chi_e$ distribution characterizing a small spherical scatterer for an incident field polarized on the blue arrow axis and using the Born approximation (BA). (b & c) scattered far-fields orthogonal projections for a spherical scatterer significantly smaller (ratio of 0.1) than the wavelength using Mie theory. . . . . 83

Figure 7.3: Depiction of Whittle-Matérn (W-M) field generated using Eq. 7.8 for three different values of correlation length. All two other parameters are kept at a fixed value of $D = 3$ and $N_c = 1$. . . . . 85

Figure 8.1: STED microscopy. (a) Comparison of STED microscopy with confocal. Figure extracted from [54]. (b) Depiction of the two necessary source structures (Gaussian and donut-shaped) for STED microscopy. (c) Simulation and experimental of the mode generated with a 3-mode photonic lantern. . . . . 95

Figure E.1: SuPyMode code snippet and simulation for 2x2 coupler. The considered design employs two SMF28 fibers in a symmetrical (left-right) configuration. The boundary condition is defined such as to compute both symmetric and antisymmetric supermodes. . . . . 120

# LIST OF SYMBOLS AND ACRONYMS

| | |
|---|---|
| SLM | spatial light multiplexer |
| WDM | wavelength division multiplexing |
| ITR | inverse taper ratio |
| FC | fiber coupler |
| DCF | double-clad fiber |
| GIF | graded-index fiber |
| MMF | multi-mode fiber |
| PL | photonic lantern |
| MSF | micro-structured fiber |
| BPM | beam propagation method |
| EME | eigenmode expansion |
| FDTD | finite-difference time domaine |
| CMT | coupled-mode theory |
| API | application programming interface |
| CPU | central process unit |
| FMF | few-mode fiber |
| FM-OCT | few-mode optical coherence tomography |
| GPU | graphical process unit |
| GUI | graphical user interface |
| GLMT | generalized Lorenz-Mie scattering theory |
| PSF | point spread function |
| LP | linearly-polarized |
| LMT | Lorenz-Mie scattering theory |
| LSS | light scattering spectroscopy |
| MSPL | modally-specific photonic lantern |
| MIP | maximum intensity projection |
| NA | numerical aperture |
| OCT | optical coherence tomography |
| OS | operating system |
| ROI | region of interest |
| RI | refractive index |
| SMF | single-mode fiber |
| SSD | source-scatterer-detector |

| | |
|---|---|
| SPF | scattering phase function |
| VSH | vector spherical harmonics |
| SDM | space division multiplexing |
| SNR | signal-to-noise ratio |
| GMS-PL | groupe-mode-specific photonic lantern |
| STED | Stimulated emission depletion microscopy |
| W-M | Whittle-Matérn |
| BA | Born approximation |

# LIST OF APPENDICES


| | | |
|---|---|---|
| Appendix A | SCIENTIFIC CONTRIBUTION | 113 |
| Appendix B | PROOF # 1 : PROPERTY OF THE FOURIER TRANSFORM OVER LAPLACIAN OPERATOR | 115 |
| Appendix C | DERIVATION OF THE ADIABATIC CRITERION | 116 |
| Appendix D | MODE COUPLING : ANALYTICAL SOLUTION | 118 |
| Appendix E | CODING EXAMPLE FOR MODE PROPAGATION | 119 |

# CHAPTER 1 INTRODUCTION

## 1.1 Background

Biomedical imaging technologies are crucial to contemporary medicine, offering detailed views into the intricate structures and functions of biological systems. Over several decades, continuous endeavors have been pursued to advance these techniques. When contrasting optical microscopy with other types of microscopy, such as electron microscopy or ultrasound techniques, it has become evident that each technique offers its characteristic set of strengths and limitations.

As an example, optical microscopy, when empowered by fiber optics, offers the advantage of being minimally invasive and is capable of capturing dynamic cellular events in real time [45, 118]. However, optical microscopy might not achieve the high resolution seen with other techniques such as electron microscopy.

In addition to the miniaturization of the imaging probes using fiber optics, fiber optics-based components—including wavelength division multiplexing (WDM), couplers, and circulators—have significantly advanced the capabilities of imaging systems, enabling enhancements in the accuracy, sensitivity, and precision of observations. These enhancements can be attributed to the refined manufacturing processes for fiber optics that have evolved over recent decades, leading to more precise and efficient optical components. This technological evolution in fiber optics manufacturing has been instrumental in elevating the performance and application scope of modern imaging systems. Following this, fiber optics have carved out a unique niche in the biomedical imaging field as optical probes and system building blocks.

Among the recent developments by the scientific community, there has also been a growing interest in exploring the potential of space division multiplexing (SDM) in the field of biomedical imaging. This potential can be attributed not only to SDM's potential for deeper penetration and enhanced resolution [106], but also due to its ability to address the limitations inherent to some traditional optical techniques, such as optical abberation correction [163], imaging speed, [76] or achieve unprecedented feature such as multifoci Raman hyperspectral imaging [95] or spatially encoded fluorescence spectroscopic imaging [61].

Over the years, spatial light multiplexers (SLMs) have evolved into highly adaptable tools for manipulating generated fields, and their applications span numerous research areas. Those devices, create structured fields by applying phase delays using micro-structured optical

components. However, despite the potential of this method, the precise control over the field structure that SLM can currently attain is limited by the resolution of the fabricated microstructures [105]. Additionally, such technique, relying on free-space phase delays are intrinsically wavelength-dependent, which can be a hindrance for some applications.

To overcome the limitations inherent to SLMs, a promising solution has emerged in the form of photonic lantern (PL) – a fiber-based component that maps single-mode fiber (SMF) to modes of a multi-mode fiber (MMF). Originally designed for astronomy technologies, PLs have recently demonstrated their capability to effectively multiplex light field structures with precise control, thereby addressing the shortcomings of SLM in engineering applications. These fiber optic components, which rely on (de)-multiplexing modal content, offer remarkable efficiency and reliability within embedded optical systems. By incorporating PLs into imaging setups, researchers have achieved enhanced control over the field structure, allowing for more accurate and detailed imaging [29].

While PLs have shown their potential in the field of imaging, they harbor some shortcomings when jointly used with coherent light sources. Attributable to their design, the optical behavior of PLs is intrinsically wavelenght-dependent. This implies a weak control on the modal amplitude, limiting the detailed analysis from modal content and prohibiting the use of large-bandwidth light sources. Additionally, PLs require a stable arrangement, as strain and bending affects the light propagation behavior [17].

However, recently, a new class of PL has emerged, featuring a design that removes the previously stated hindrance. This new type of optical component, namely modally-specific photonic lantern (MSPL), offers a stable optical response over a considerable bandwidth ($> 100$ nm) enabling the control of the light field generated extended to the relative phase of the modal content. These component differs from standard PLs through their asymmetric design enabling a one-to-one mapping between the mode of the input SMF and output MMF. This attribute makes them particularly advantageous for broad bandwidth imaging methodologies like optical coherence tomography (OCT) or spectroscopy, wherein capturing an extensive spectrum of wavelengths is essential for a precise analysis [64]. Utilizing the intrinsic characteristics of MSPLs, scientists can harness the novel contrast mechanism emerging from a meticulous examination of the modal content.

## 1.2 Problem Statement

While MSPLs have demonstrated substantial promises in the realm of fiber optic communications, their design and incorporation into biomedical imaging remains in its infancy. Several

instances of MSPLs have been developed through different designs yet, the process for manufacturing the components remains a subject of intensive research. Currently, there exists no established design methodology for the production of these components, necessitating an initial phase of rigorous, resource-intensive, and detailed exploration to establish a design framework.

Regarding the implementation of the MSPL in the imaging field, the fundamental challenge lies in deciphering the interactions between structured light fields and biological samples. This includes understanding and effectively utilizing the contrast mechanisms inherent in these interactions. To date, there exists no comprehensive model describing the interactions of coherent and structured light sources with turbid media. The absence of such a model has been a significant factor contributing to the observed stagnation in advancements within this specific area of study.

### 1.3 Objective of the Research

This thesis focuses on the development of a novel fiber optic component, specifically MSPLs, for biomedical imaging applications and more specifically optical coherence tomography (OCT). The primary aim is to demonstrate how MSPLs can be employed to generate structured light fields for enhanced imaging, whilst simultaneously developing models and numerical tools to emulate light-matter interaction and subsequently extract valuable predictions. This research aims to :

**Specific objective 1** : Designing and producing an MSPL suitable for OCT imaging.

- Developing the numerical tools for fiber optic component design simulation and analysis ;
- Developing a recipe for conception of a very-short (robust) and broad-band MSPL centered at a suitable wavelength for OCT ;
- Manufacturing and characterizing the MSPL.

**Specific objective 2** : Elucidating the contrast mechanism associated with structured light interaction with biological samples.

- Developing a numerical library for Lorenz-Mie scattering theory (LMT) single scattering processes, including a model for detection scheme ;
- Validating the simulation results with other models found in the scientific literature ;
- Evaluating prediction for single scattering event coupling with a coherent detection scheme ;

— Assessing the different contrast mechanisms enabled by structured and coherent coupling scheme in the context of biological imaging.

— Establishing a second model using Born approximation for multi-scattering events

— Forming predictions from the multi-scattering model and corroborate the prediction of LMT.

**Specific objective 3** : Devising an MSPL based OCT system and validating the predicted contrast mechanism.

— Devising a new bench-top system integrating a MSPL ;

— Developing the signal processing tools for such a system ;

— Validating the contrast mechanism with microbeads ;

— Exploring the contrast channel for biological sample

## 1.4 Thesis Outline

As presented in Figure 1.1, this thesis is divided into several chapters, each addressing a distinct aspect of the research.

— In **Part 1 : Introduction**, Chapter 1 introduces the problem statement, and Chapter 2 offers an extensive literature review. The review covers essential technologies and modeling strategies relevant to this dissertation, including fiber optic components, light-matter interactions via Lorenz-Mie scattering, and OCT techniques. A significant emphasis is directed towards the design and optimization of the PL, the principal technological focus of this research.

— **Part 2 : Structured light engineering** elaborates on the design and development of MSPLs through the use of simulation tools. More specifically, Chapter 3 expands on the development of a simulation library, designated as SuPyMode, enabling efficient design of fiber optics component such as MSPLs through the use of the adiabatic criterion metric.

— **Part 3 : Light-matter interaction** addresses the formulation of a light-matter interaction model for coherent and structured light fields, specifically those produced by PLs. This section delves into the diverse methodologies facilitating the modeling of interactions between structured fields and turbid media, like biological samples. Initially, Chapter 5 describes the Lorenz-Mie scattering software engineered to explore these interactions from a fundamental perspective, yielding notable outcomes. Subsequently, the Chapter 7 delves into the light-matter interaction description utilizing the Born approximation, aiming to ascertain critical scattering characteristics.

— **Part 4 : Few-mode imaging** addresses the incorporation of an MSPL into an OCT system. Within Chapter 6, a detailed explanation of the system's implementation is presented, alongside empirical data which is then contrasted with a previously established model. Conclusively, Chapter 6 expounds upon the ramifications of the garnered results, prospective utilities of the PLs, and the subsequent advantages conferred to the realm of biomedical imaging.

— **Part 5 : Discussion and conclusion** encompasses a systematic evaluation of the research presented. In Chapter 8, salient insights, recommendations, and persisting queries are deliberated upon. Chapter 9 concludes the thesis, summarizing the achievements of this research and suggesting future directions for this field.

All published scientific articles are incorporated into this thesis as independent chapters. A complete list of scientific contributions is provided in the appendix.

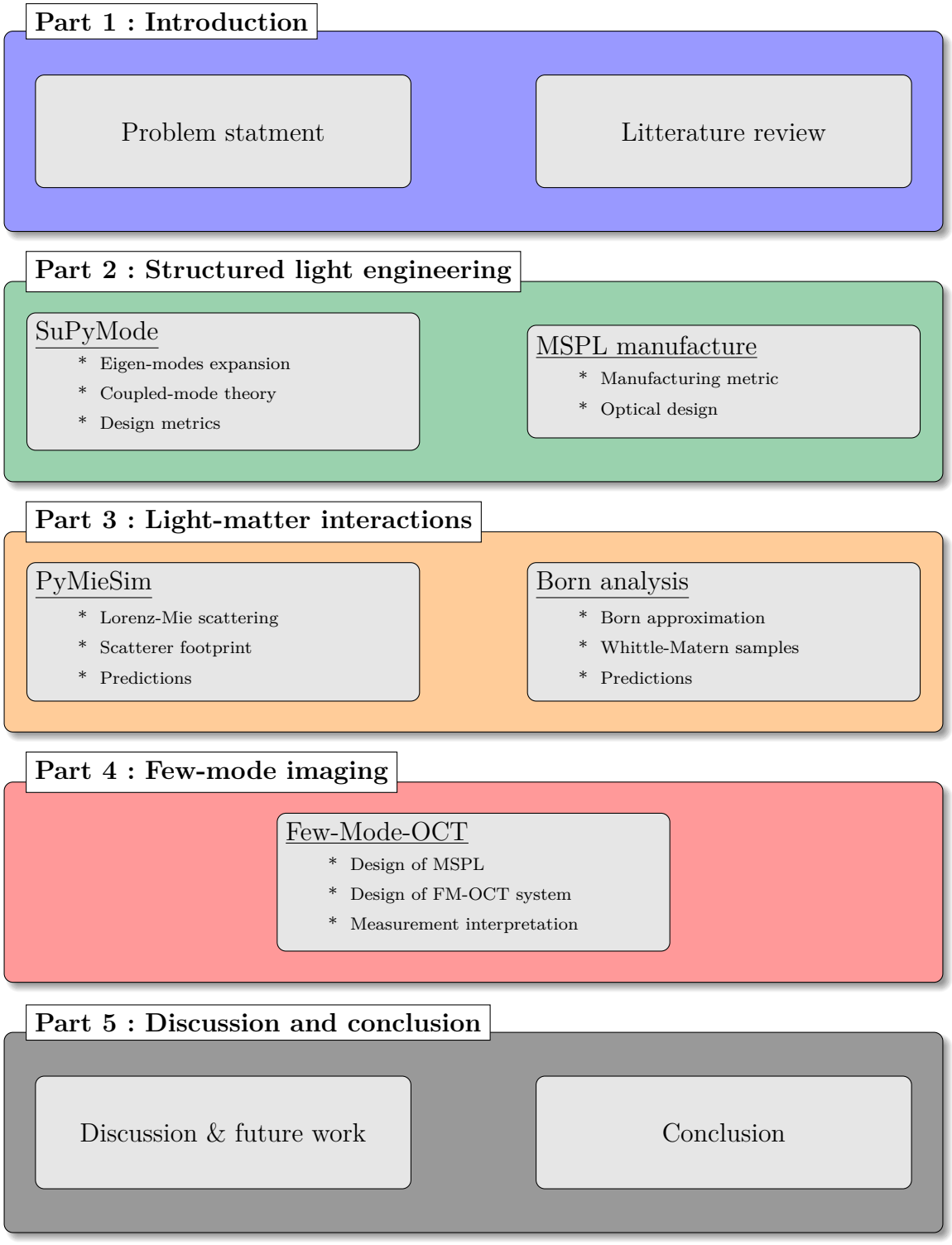



FIGURE 1.1 Thesis structure

# CHAPTER 2 LITERATURE REVIEW

This chapter provides a comprehensive overview of the previous and concurrent developments in the relevant fields underpinning this thesis. It primarily focuses on the historical and contemporary advancements in the domains of photonic lanterns (PLs), multi-mode imaging, optical coherence tomography (OCT), structured light fields, Mie scattering, and their applications in biomedical imaging. A careful examination of these domains underscores the existing knowledge gaps and highlights the potential for the innovative usage of MSPLs in advancing biomedical imaging technology.

## 2.1 Photonic Lanterns : Development and Applications

In recent years, the demand for efficient and high-capacity optical communication systems, advanced sensing technologies, and precise astronomical instrumentation has fueled the need for innovative photonic devices. PLs, also known as mode multiplexers, have emerged as a promising solution to address the challenges associated with efficient light manipulation in such applications. These devices provide a passive and elegant means to convert and multiplex optical modes, enabling seamless integration of various photonic components.

The design of a PL significantly influences its operational subcategories, leading to the development of distinct subclasses within the domain of PL technology. Notably, the literature identifies three principal variants : the conventional PL, the modally-specific photonic lantern (MSPL), and the groupe-mode-specific photonic lantern (GMS-PL). These variants exhibit unique characteristics in terms of modal crosstalk management.

Specifically, the MSPL is designed to eliminate modal crosstalk entirely, facilitating a direct and isolated correspondence between each single-mode fiber (SMF) input and the few-mode fiber (FMF) output. This one-to-one mapping is critical for applications requiring high fidelity in mode transmission. Conversely, the standard PL architecture does not prioritize the mitigation of modal crosstalk, which can lead to mode mixing and potential signal degradation. The GMS-PL variant introduces a nuanced approach by constraining modal crosstalk within predefined groups of modes, allowing for controlled interaction among specific mode sets while maintaining separation from others.

This hierarchical categorization of PL technology underscores the adaptability of PLs in tailoring light propagation characteristics to specific application requirements, ranging from complete crosstalk suppression to selective mode grouping.

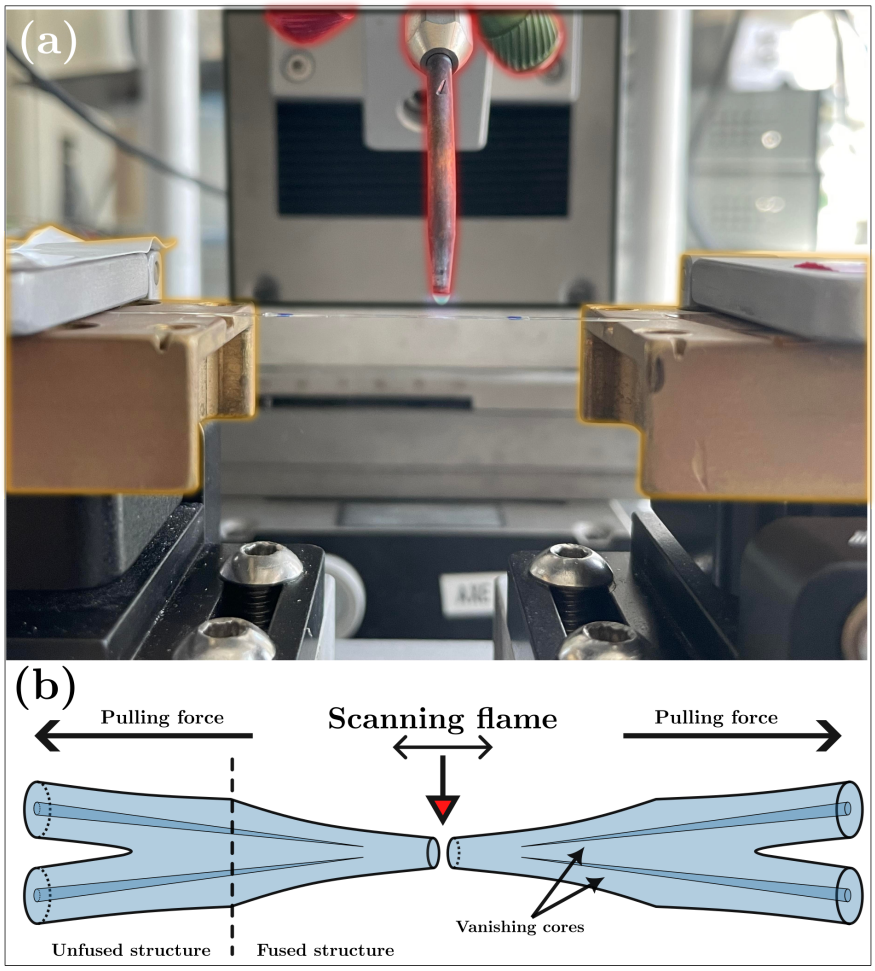



FIGURE 2.1 Depiction of a coupler manufacturing station. (a) Picture of the fusion station setup. Highlighted in red is the flame nozzle, in yellow the pulling section, on which lies the fused fiber structure. (b) Schematic of the main components of the manufacturing process

Across all those designs, PLs are typically based on a set of SMF that transitions into a multimode fiber [15, 20, 90, 116] through a fusion and tapering process, as depicted in Figure 2.1. The design parameters of the manufacturing process are carefully engineered to facilitate a low-loss mode conversion between the multimode and single-mode ends. This feature is regarded as paramount in the development process and can only be achieved through a meticulous tapering of the structure. To this end, various design were investigated, notably using graded-index fiber (GIF) [66, 160] or double-clad fiber (DCF) [57].

A key advantage of MSPLs lies in their efficient conversion of optical modes across a broad bandwidth. This efficiency stems from an asymmetric design that allows selective coupling of various modes into distinct single-mode fibers. Such design facilitates the extraction of specific modes from a multimode input, enabling mode-selective signal processing. The low-loss and minimal cross-talk characteristics of MSPLs are crucial for enhancing photonic system performance, simplifying downstream analysis.

Despite significant scientific interest in the past decade, the numerical modeling of the manufacturing process for MSPLs remains largely unexplored. The development of these components relies almost entirely on experimental validation, which can be a resource intensive and tedious process.

This thesis primarily emphasizes on the development and utilization of MSPLs in the context of biomedical imaging. The relevance of MSPLs methodologies is pervasive throughout the document, with particular significance accorded to Chapters 3, 4 which discuss the development of numerical tools for developing components and 6 which present an application of imaging technique using MSPL.

## 2.2 Structured Light Fields : Harnessing Complex Light

Structured light fields, characterized by the spatial modulation of light's amplitude, phase, or polarization, have garnered significant interest in optical physics and photonics due to their vast potential applications, including optical trapping [162], high-resolution imaging [93], enhanced contrast [39], optical communication [137], and 3D reconstruction [146]. Originating from early discoveries in light interference and diffraction, the precise and dynamic control over these light fields became possible with technological advances like spatial light modulators (spatial light multiplexers (SLMs)) and computer-generated holography [53, 152].

Recent advancements in optics have introduced few-mode fibers (FMF) into optical systems, offering controlled mode distribution for new functionalities beyond their primary data transmission capabilities, notably in imaging [132]. However, integrating multimode fibers (MMF)

into contemporary imaging systems presents challenges. The very aspect of multiple mode propagation, while being a strength, also introduces complexities. Mode dispersion, where various modes travel at different velocities, can potentially distort an image, challenging the integrity of data being transmitted [80]. Moreover, complex modal interactions can affect the imaging system's robustness and reliability [120].

As multimode fibers increasingly become integral to imaging, fully understanding their capabilities and complexities is essential. Likewise, the complex interplay between structured fields, used for either illumination or light collection, and turbid media presents a significant challenge in understanding contrast mechanisms. It is crucial to comprehend the implications of these interactions to evaluate the value of such multimodal imaging techniques.

The topic of light turbid-matter interaction is explored in the context of single particle scattering in Chapter 5 and in the context of turbid media in Chapter 7.

## 2.3 Optical Coherence Tomography : A Powerful Imaging Modality

Often likened to an "optical ultrasound", OCT captures high-resolution, cross-sectional images of the internal structure of tissues, achieving detail near the cellular level that many other imaging methods cannot [68]. Since its design in the early 1990s, OCT has emerged as a cornerstone in specialties such as ophthalmology, where it has significantly enhanced our understanding of retinal diseases and their management [44]. However, its applicability stretches beyond the retina, extending into cardiology, dermatology, oncology, and even material science [74].

The foundation of OCT lies in its ability to infer depth-discriminated scattering and absorption properties from internal tissue structures. By emitting a beam of light onto a tissue and analyzing the backscattered light coupling from different layers, OCT can create a detailed, depth-resolved map of that tissue.

Over the years, innovations and advancements in OCT technology have broadened its potential, paving the way for enhanced diagnostic precision, more targeted treatments, and better patient outcomes [1]. Its non-invasive nature, combined with the ability to offer real-time, *in situ* imaging, positions OCT as a gold standard in many clinical scenarios [136]. This subject matter is pertinent to comprehending the content of Chapter 6, which delineates an enhanced adaptation of the OCT system.

## 2.4 Mie Scattering : A Key Physical Process

Scattering is a fundamental physical process through which the propagation direction of waves or particles is altered due to their interaction with a given medium. This phenomenon can be observed across a broad range of systems, from photons scattering off atomic particles in gases, to the diffraction of X-rays in crystallography, and even to the scattering of sound waves in various materials. Scattering plays a pivotal role in various scientific and engineering disciplines, contributing to our understanding of atomic and molecular structures, atmospheric optics, oceanography, acoustics, and numerous other fields.

The theoretical foundations and mathematical formulations of scattering have been extensively studied and developed over the past century. Pioneering works by Rutherford [138] in the early 20th century shed light on the behavior of alpha particles scattered by atomic nuclei. This was soon followed by significant contributions by scientists such as Rayleigh [147], who explored the scattering of light by small particles, explaining phenomena like the blue color of the sky. Gustav Mie's 1908 work on light scattering clarified the process, distinguishing two regimes : Rayleigh and Mie. The Rayleigh regime applies to scatterers much smaller than the wavelength, easily modeled. The Mie regime, for larger scatterers, requires complex modeling but has no size limit for the scatterers it can model. The Mie solution, expressed as an infinite series of vector spherical harmonics, is a general model [110]. In the realm of biomedical imaging, understanding of light scattering has become indispensable. The interactions of light with tissues result in various scattering patterns, which can provide crucial information about the structural and functional aspects of biological samples. Techniques such as OCT, light scattering spectroscopy (LSS), and flow-cytometry leverage the properties of light scattering to extract information from subsurface layers of tissues, offering insights that are not achievable with traditional microscopy methods [68]. Furthermore, the analysis of how light scatters off biological tissues can aid in the early detection of diseases, such as cancer, by identifying irregularities or changes in tissue morphology [8]. While, single-particle interaction (as described per Mie scattering) with light cannot render the full picture of light-matter interaction in biological tissues, it is a stride in the direction of understanding some peculiarities when it comes to the general optical behavior. Hence, understanding and harnessing the principles of light scattering through Mie scattering, are of paramount importance for advancements in biomedical imaging.

Understanding the intricacies of light scattering is not only pivotal to advancing scientific knowledge but also holds implications for various technological applications. As we delve deeper into this topic in the later sections, we will explore the fundamental concepts, the governing equations, and the various applications of scattering in modern biomedical imaging

technology. In particular, Chapter 5 explores the different contrast mechanisms that can be exploited through the design of light scattering experiments, providing us with a more profound understanding of light-matter interactions process involved in coherent imaging systems.

# CHAPTER 3 ARTICLE 1 : SUPYMODE : AN OPEN-SOURCE LIBRARY FOR DESIGN AND OPTIMIZATION OF FIBER OPTIC COMPONENTS

This chapter was adapted from : **Martin Poinsinet de Sivry-Houle**, Rodrigo Itzamna Becerra Deana, Stéphane Virally, Nicolas Godbout, and Caroline Boudoux, "SuPyMode : An open-source library for design and optimization of fiber optic components," submitted to Optics Continuum on November 20, 2023.

## 3.1 Author Contribution

The article on which this chapter is based was submitted to Optics Continuum, submitted on the 4th of October 2023. Martin Poinsinet de Sivry-Houle is the first author of the publication and contributed to 90% of the work. Nicolas Godbout and Caroline Boudoux were senior investigators and assisted in the manuscript revision.

## 3.2 Chapter Context

This chapter delves into the specifics of SuPyMode, a software tool devised to design new fiber optic components. Notably developed to cater for the manufacturing of modally-specific photonic lantern (MSPL), the library demonstrates how structured fiber component helps to lower the adiabatic criterion of tapered structure. Thus enabling more robust components featuring lower cross-talk and losses. SuPyMode enables an in-depth analysis of simulated components with featuring visualization and predictive tools for design exploration. The prediction of the simulation was exploited to develop a new component which features wavelength independence on a large bandwidth and low modal cross-talk.


## Abstract

Recent advancements in photonic lantern design have stirred interest in computational tools to develop fiber-based components. Addressing the complex design challenges, we introduce SuPyMode, a Python package that enables comprehensive fiber component design analysis. This study details its mathematical framework and verifies its accuracy and reliability through simulation results. We demonstrate its practicality using a design study on modally-specific photonic lanterns, underlining the tool's versatility and efficacy. SuPyMode is instrumental for researchers and engineers in the design and optimization of fiber components, thereby

advancing photonics technology.

### 3.3 Introduction

Fused fiber optics components are of paramount importance to various applications, including optical communications [171], laser generation [75], and biomedical sensing [31]. Catering to the diverse demands of such applications, components have exploited several fiber types including single-mode fibers (SMFs), multi-mode fibers (MMFs), and few-mode fibers (FMFs) to produce wavelength division multiplexings (WDMs), fiber couplers (FCs), and photonic lanterns (PLs), thus enabling a wide range of functionalities. These components are typically manufactured using a fusion and tapering process [153], which involves a transversally homothetic transformation of the waveguide structure. Several numerical techniques have been developed to simulate the optical behavior of fiber optic components, including the beam propagation method (BPM) [84], finite-difference time domaine (FDTD) [4], and eigenmode expansion (EME) [48]. Accordingly, multiple numerical libraries were developed, such as BeamLab [131] and Lumerical [103] exploiting BPM, GMES [30] and GprMAX [50] employing FDTD, and, finally, EMEPy [60] using EME. Among these numerical techniques, EME, described in Section 3.5.2, is the preferred method for computing modal propagation inside fiber optic components because it offers speed and the insight associated with separately following individual modes [48]. The library EMEPy provides a foundation for solving Maxwell's equations for a predefined waveguide. However, it does not allow for generating the fused waveguide geometry, but, instead, relies on user input. Furthermore, EMEPy does not exploit the numerical advantages provided by the homothetic transformations of tapered structures. Among such advantages is the capability to compute the adiabatic criterion, which describes modal propagation independently of the tapering process. The adiabatic criterion—derived from the inter-modal coupling factor— holds paramount significance in the manufacturing process as it allows choosing the proper tapering process to ensure well-behaved components (i.e., minimal coupling between non-degenerated modes). Despite renewed scientific interest in designing complex fused component structures, there is currently no fully integrated pipeline for simulating fiber optic components. This lack of framework precludes design optimization, thereby resulting in a tedious manufacturing process. To address this shortcoming, we developed SuPyMode : a flexible and integrated Python library that provides EME computation combined with coupled-mode theory analysis for fiber optic component design and optimization. In this manuscript, we present the architecture of SuPyMode, the theoretical framework upon which it is built, and validate its numerical output against known analytical solutions. We then showcase its performance through representa-

tive simulation scenarios, including the design of MSPL with and without mode skipping. We conclude this paper with a discussion on the limitations of this open-source library.

## 3.4 The Library

The source code of SuPyMode is built around a C++ computing core wrapped into a flexible Python user interface, providing reduced computing time compared to a pure Python package.

### 3.4.1 Code Architecture

Figure 3.1 depicts the architecture of SuPyMode, which utilizes the object-oriented nature of Python and C++ to define four primary classes : OpticalStructure, EigenSolver, SuperSet, and SuperMode. These classes interact as illustrated in Figure 3.1 (a). As the code consists of a Python wrapper for C++ , it needs to be compiled, making it dependent on the operating system (OS). This constraint potentially limits the widespread use of the library. To address this limitation, SuPyMode leverages the Python package manager, which includes pre-compiled code to ensure extensive portability. At present, the Python package is available on the main operating systems, including Linux, macOS, and Windows, for Python versions 3.10 and later. It is important to note that users can manually install the package for most system configurations. Additionally, SuPyMode is accessible on the online Google Colab platform, which requires no installation and is compatible with all operating systems.

### 3.4.2 Compute Time Optimization

The EME computation can become prohibitively slow for finely detailed mesh. However, the scales involved in the fiber structure fusion process require high resolution to approximate adequately the fiber optic mode solutions. This effect becomes even more significant for complex structures requiring larger meshes. To mitigate this problem, SuPyMode uses different strategies, including scaling up the light source wavelength instead of scaling down the optical structure ; using a predictive eigenvalue pre-solution ; exploiting the symmetries of the structure to reduce the computation time ; implementing all the computation-intensive steps in a parallelized C++ core.

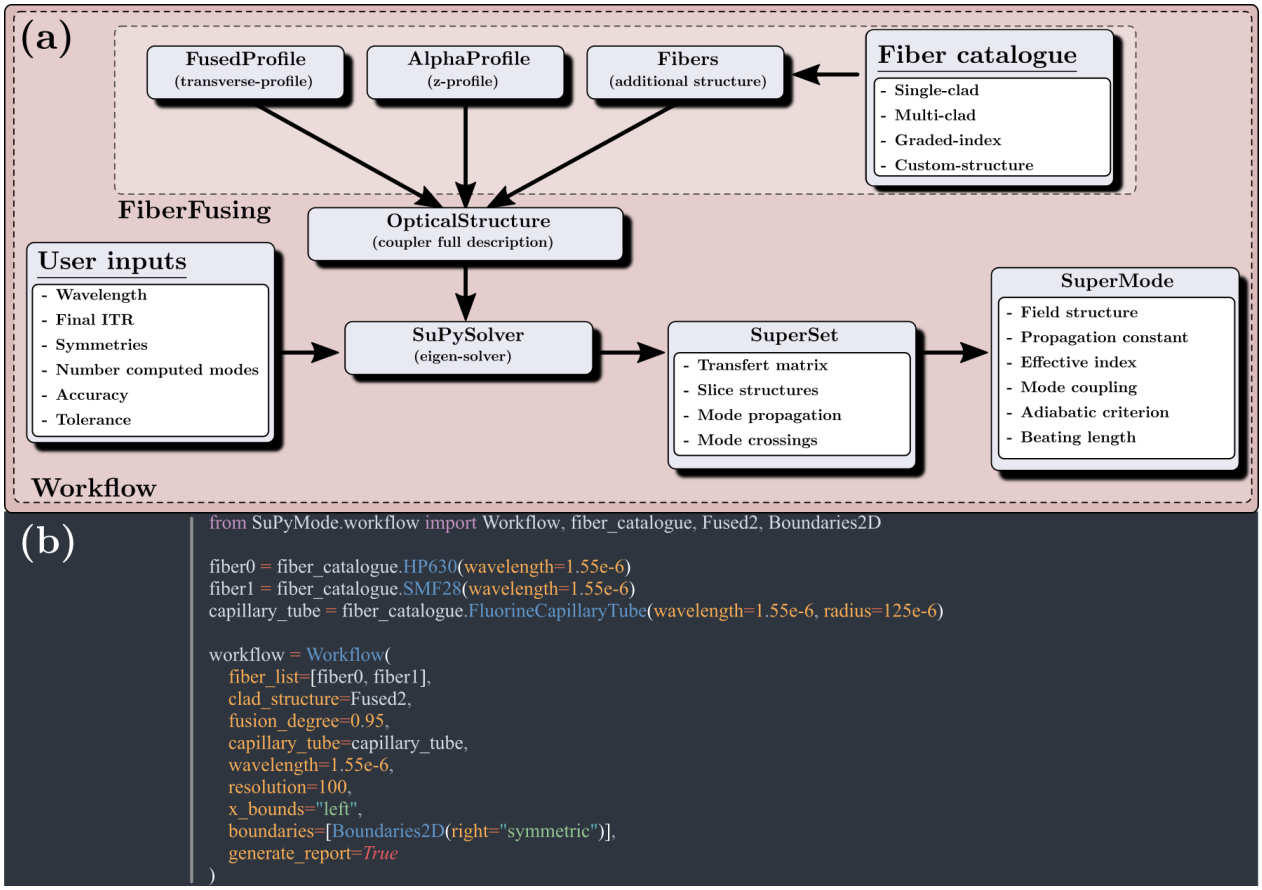



FIGURE 3.1 Illustration of the architectural arrangement and user interface of the SuPyMode library. (a) Depiction of the structure, pipeline, and computing capabilities of the library. The entire definition of the optical structure is comprised in the FiberFusing package. The entire data-extraction pipeline is encompassed in the workflow framework. (b) Code snippet for 2x2 asymmetric coupler simulation using the aforementioned workflow framework. The considered design employs two different fibers (SMF28 and HP630) to break the *top-bottom* symmetry, enabling the lifting of mode degeneracy.

### 3.4.3 User Interface

SuPyMode offers a Python application programming interface (API) and a suite of visualization and analysis tools, providing an intuitive overview of the computational process. It also includes a collection of self-contained numerical tools that can be integrated into other projects. SuPyMode generates data in the NumPy format [62], which facilitates integrating its C++ -generated data into any Python project. The computation pipeline was devised to facilitate optical design analysis and optimization. In that regard, the workflow class shown in Figure 3.1 (a)integrates the full computation and analysis within an intuitive interface and predefined properties. The intuitive nature of the SuPyMode library is illustrated in Figure 3.1 (b) through a code snippet used to simulate a 2x1 MSPL, discussed in Section 3.6.1. This particular example produces the full analysis of an asymmetric coupler. Documentation including the installation directives and examples of the code used to produce the figures in this paper can be found at `https://SuPyMode.readthedocs.io/en/latest/`.

## 3.5 Theory

The specialized Python library SuPyMode has been engineered to provide an extensive toolkit for the precise design of fiber optic components. This package amalgamates advanced EME and coupled-mode theory (CMT) frameworks, thereby offering an interactive user interface. This software package facilitates the simulation of fiber optic mode propagation, the analysis of modal coupling, and the deduction of necessary coupler properties to mitigate this coupling, thereby enhancing the performance of the fiber optic components.

### 3.5.1 Fiber Coupler Structure

The initial tool offered by SuPyMode is a simulation framework designed to compute the transverse structure of a multi-fiber fusing process. The algorithm utilized to simulate the fusion process is based on the work of [83] and has been generalized to accommodate more than two fibers. The FiberFusing component of the library formulates and solves the fusion step as a geometrical optimization problem incorporating physical constraints such as core position, area conservation, and the existence of derivatives at all points. Seven predefined configurations are already included in FiberFusing, encompassing the most commonly observed structures found in the literature [139,160] : $(2\times2), (3\times3), (4\times4), (5\times5), (7\times7), (10\times10), (15\times15)$. Figure 3.2 (a) shows the transverse profile of four predefined coupler structures for two different degrees of fusion : 0.3 (top row) and 0.8 (bottom row). Each of the predefined configurations can be adjusted for an arbitrary degree of fusion (as defined in [83]), an important design

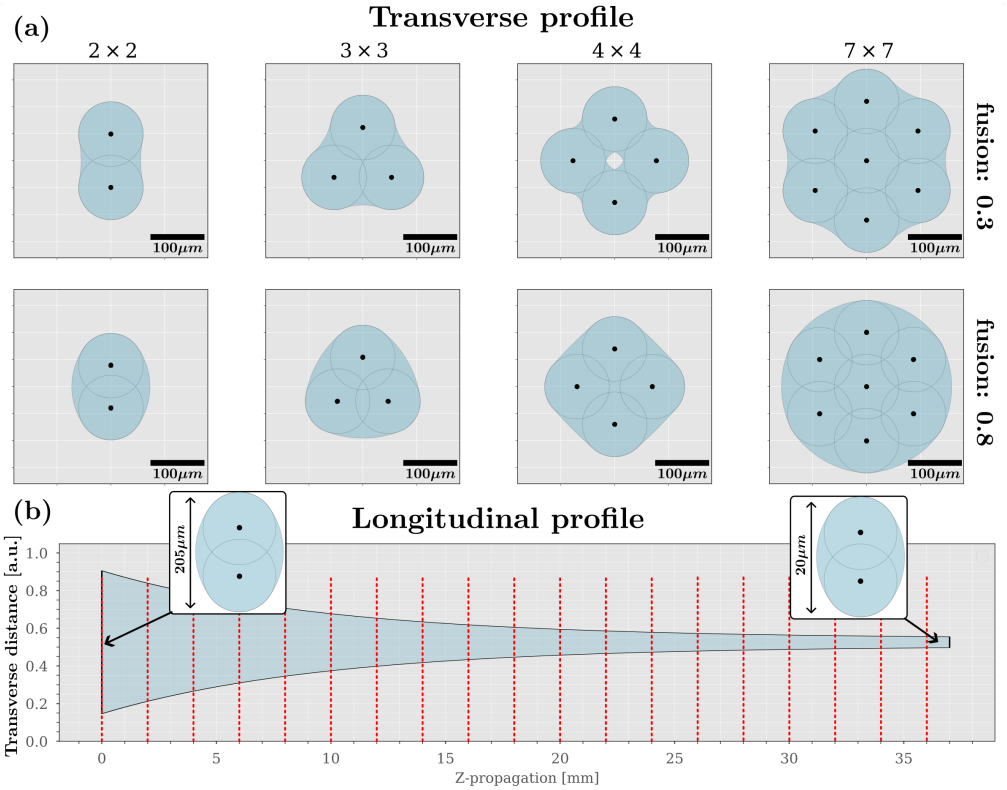



FIGURE 3.2 Depiction of an optical coupler model in transverse (a) and longitudinal (b) sections. (a) Four predefined transverse profiles with, from left to right, 2, 3, 4, and 7 fibers, with the location of the core in black and the cladding in blue, for two degrees of fusion : 0.3 (top row) and 0.8 (bottom row), where 0 corresponds to the fibers adjacent to one another and 1 corresponds to a complete fusion. Longitudinal profile of a 2×2 structure (b) with a taper corresponding to the manufacturing process defined in [153]. The red dotted lines correspond to the selected cross-sections used for eigenmode computation. Insets show cross-sections at the locations indicated by the black arrows, with a degree of fusion of 0.8.

parameter for the manufacturing process. The library enables the simulation of custom mesh configurations for non-standard manufacturing processes, for instance, where hollow capillary tubes are used to configure the spatial arrangement of the fibers.

### 3.5.2 Eigenmodes Expansion

SuPyMode divides an optical structure longitudinally into segments. For instance, Figure 3.2 (b) shows the longitudinal profile of the taper of a $2 \times 2$ structure with 19 segments (illustrated by the red dotted lines). The cross-section of each segment is obtained by homothetic transformation of the initial cross-sectional index of refraction, defined in polar coordinates as $n_0(r, \theta)$. The homothetic transformation of a particular segment is characterized entirely by a length scale $\rho$, the distance between the center of the homothecy, and a particular point on the cross-section. The index-of-refraction profile of the tapered cross-section is

$$n(r, \theta) = n_0\left(r\,\frac{\rho_0}{\rho}, \theta\right), \tag{3.1}$$

where $\rho_0$ is the length scale of the untapered initial segment. The length scales $\rho$ and $\rho_0$ are not absolute and depend on the point that is chosen initially. Only their ratio is physically relevant. We thus define the inverse taper ratio (ITR) as the homothetic ratio $\rho/\rho_0$. Along with the initial cross-section $n_0(r, \theta)$, it completely defines the local geometry.

EME solves for the eigenmodes and eigenvalues of the local scalar Helmholtz equation

$$\left(\nabla_\perp^2 + k^2 n^2(r, \theta, z)\right)\, \psi(r, \theta, z) = \beta^2 \psi(r, \theta, z), \tag{3.2}$$

where $\nabla_\perp^2$ is the transverse Laplacian. The eigenmodes of a fused superstructure are usually referred to as supermodes, which is the term used throughout the remainder of the text. Supermode $i$ is defined by its scalar electric field L2-normalized amplitude (eigenstate) $\psi_i(r, \theta)$ and its propagation constant (eigenvalue) $\beta_i$.

Equation (3.2) can be transformed into a numerical problem by utilizing the finite-difference method to approximate the derivatives. SuPyMode provides the option of using either the second or third-order finite-difference method, allowing the end-user to reach a compromise between desired precision and compute time. For each segment, the software calculates the first $n$ (user-defined) solutions to the local eigenvalue problem. The eigen-decomposition is performed using the Eigen [56] and Spectra libraries, which are based on Arpack [87] for sparse-matrix linear algebra algorithms. Furthermore, a series of tests and sorting operations are conducted to ensure adequate mode-matching from one segment to the next. The data

structure that encapsulates the collection of calculated supermodes is formatted in a manner that enables its export as a serialized object, thereby facilitating its utilization by external users.

### 3.5.3 Coupled-Mode Theory

The longitudinal propagation within a segment is computed using CMT [24]. Compared to other simulation methods, the combination of EME and CMT possesses the advantage of not relying on initial illumination conditions. Optical dynamics are entirely encapsulated in the supermodes that are computed at every segment of the coupler. They depend, on one hand, on the local geometry of the segment : the index-of-refraction profile $n_0$ of the fused cross-section and the ITR$= \rho/\rho_0$. On the other hand, they also depend on the local slope of the taper, represented by the logarithmic derivative of the characteristic length scale

$$s(z) = \frac{1}{\rho(z)} \frac{\mathrm{d}\rho(z)}{\mathrm{d}z}. \tag{3.3}$$

Here again, the relative nature of the length scale $\rho$ plays a key role : the only physically relevant quantity is its logarithmic derivative and not its absolute derivative.

Given a set of supermodes $\psi_i$ and their respective propagation constants $\beta_i$, CMT derives the coupling coefficient [1]

$$C_{ij} = \frac{\pi k^2}{(\beta_i - \beta_j)\sqrt{\beta_i \beta_j}} \left\langle \psi_i \middle| \frac{\partial n^2}{\partial z} \middle| \psi_j \right\rangle, \tag{3.4}$$

for each pair of supermodes $i$ and $j$. In this equation, $k$ is the wavenumber, and $n(r, \theta, z)$ is the index-of-refraction profile of the tapered structure. The sesquilinear product is given by

$$\langle \psi_i | f | \psi_j \rangle = \int r \, \mathrm{d}r \, \mathrm{d}\theta \;\; \psi_i^*(r, \theta) \, f(r, \theta) \, \psi_j(r, \theta), \tag{3.5}$$

where the integral is taken over the infinite transverse plane. Each coupling coefficient $C_{ij}$ is of the form

$$C_{ij}(z) = \frac{\tilde{C}_{ij}(z)}{s(z)}, \tag{3.6}$$

where $\tilde{C}_{ij}(z)$ is the normalized coupling coefficient, which depends only on the local geometry of the segment, and not on the slope. Equation (3.4) highlights the fact that modes harboring opposite transverse symmetries with respect to the optical structure $n(r, \theta)$ do not

1. See supplementary material for a detailed derivation.

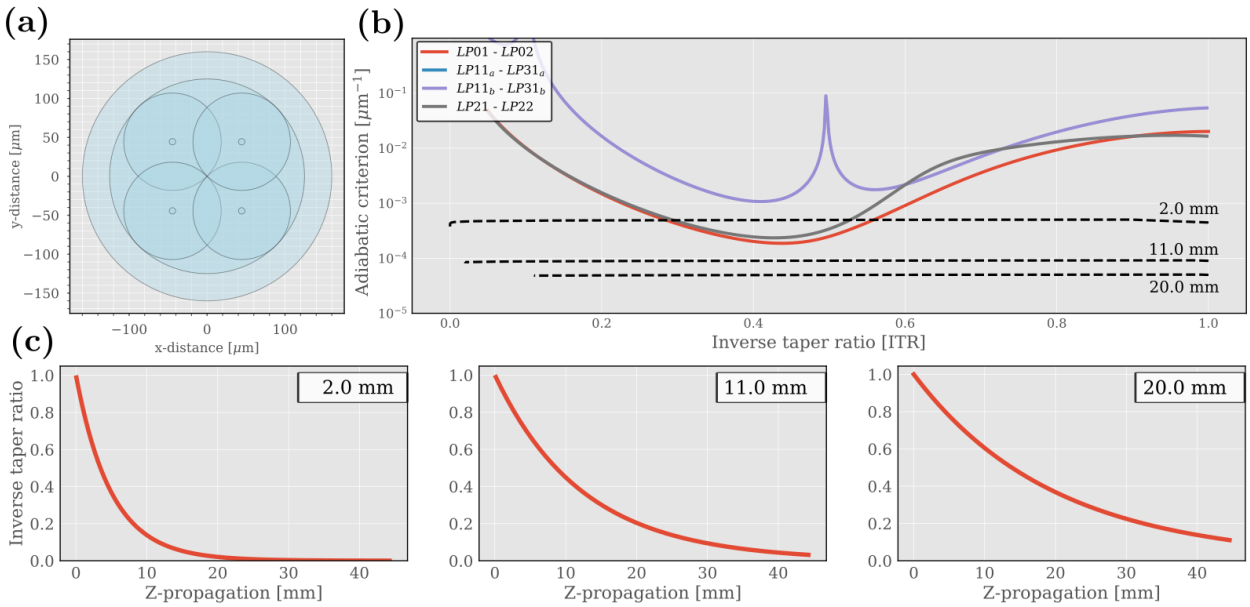



FIGURE 3.3 Profile (a), adiabatic criterion (b), and ITR (c) of a 4x4 hybrid coupler. (a) The section shows 4 fibers placed in a glass capillary with a degree of fusion of 0.8. (b) Adiabatic criterion of for the computed modes. The black dotted lines represent the coupling factor for coupler profiles computed for different initial heating length ranging from 2 mm to 20 mm. The simulated heat-processing time is 1600 seconds and the alpha parameter (defined as the rate of change of the heating length [153]) is zero. (c) Representation of the coupler ITR as a function of the propagation direction.

couple together. This particularity can be used to focus the simulation results onto specific symmetries, as it was experimentally implemented in [160]. Propagation within the segment is given by the equation

$$\frac{\mathrm{d}}{\mathrm{d}z}\begin{bmatrix} a_1 \\ \vdots \\ a_n \end{bmatrix} = i\begin{bmatrix} \beta_1 & C_{12} & \cdots & C_{1n} \\ -C_{21} & \beta_2 & \cdots & C_{2n} \\ \vdots & \vdots & \ddots & \vdots \\ \cdots & \cdots & \cdots & \beta_n \end{bmatrix}\begin{bmatrix} a_1 \\ \vdots \\ a_n \end{bmatrix} \quad , \tag{3.7}$$

where $a_i$ is the amplitude of the $i^{th}$ mode. The library uses the Runge-Kutta algorithm [25] to simulate the mode propagation for a given input. Additionally, the library can calculate the adiabatic criterion, a valuable parameter that can be utilized to infer the required $z$-profile to suppress mode coupling (i.e., to remain adiabatic). The adiabatic criterion is defined as

$$\tilde{\alpha}_{ij} = \frac{\beta_i - \beta_j}{\tilde{C}_{ij}} \tag{3.8}$$

and is, like the normalized coupling coefficient, independent of the longitudinal profile. Hence, it is very relevant for the design and optimization of optical structures. In the two-mode model, a tapered curve equalling the adiabatic criterion would generate a 10% coupling at every half-beating length between the modes, as shown in [101]. To prevent unintended coupling, it is necessary to adhere to a curve that lies beneath the adiabatic criterion. Figure 3.3 illustrates the adiabatic criterion of the four computed modes for a symmetric 4x4 coupler made of SMF28 fibers. The longitudinal profiles of the couplers are computed for three different initial heating lengths, as defined in [153], and included in the graph. It should be emphasized that SuPyMode also enables the calculation of coupler profiles with multiple segments, a necessary requirement for precise optimization of optical coupler designs. Figure 3.3 (a) highlights that a heating length of 2 mm results in a notable coupling with the propagating modes as it crosses the adiabatic curves. Consequently, this particular design is typically not recommended.

### 3.5.4 Validation

Validation of predictions from the library was performed using a cylindrical-symmetric structure for which analytical solutions are known[1]. Figure 3.4 shows the accordance of the different essential parameters computed with SuPyMode and the analytical results. From Fig 3.4 (a-b), we can notice a relabelling (swap) of the modes $LP_{03}$ and $LP_{41}$ at an ITR value of 0.5. This effect can be attributed to a strong coupling behavior, which can be imputed to

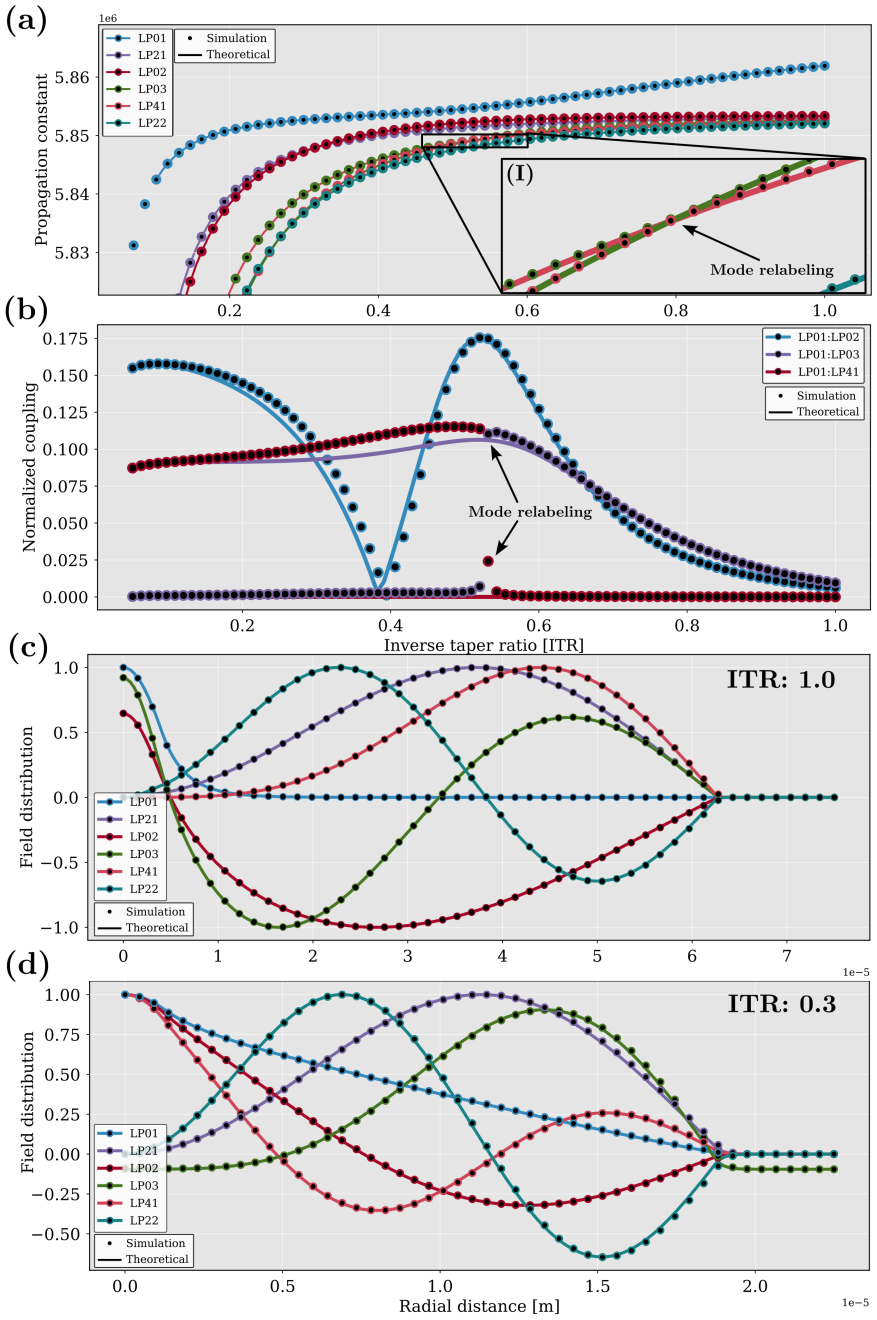



FIGURE 3.4 Comparison of simulated and analytical results for propagation constant (a), normalized coupling (b), field distribution at ITR of 1.0 (c) and 0.3 (d) of a single SMF28$^{TM}$ fiber taper.

the propagation constant of the two modes converging to a similar value. From a theoretical perspective, $LP_{03}$ and $LP_{41}$ modes remain uncoupled due to their inherent symmetrical and anti-symmetrical properties along a consistent axis. Consequently, the overlapping of their propagation constants is not theoretically problematic. Nevertheless, numerical methods might not maintain these exact symmetries, thereby permitting mode coupling. From Eq. (3.4), we can expect a rapid variation of the normalized coupling for converging propagation constant, which is highlighted in Fig. 3.4 (b). This strong coupling behavior is corroborated by the avoided crossing highlighted in inset (I) of Fig. 3.4 (a).Additionally, validation of field structures computed with the library was also performed by juxtaposing the results with pre-established simulation outcomes utilizing BPM and experimental findings. An extensive analysis was conducted on the mode field structure at varied ITR, effective index, and general coupling behaviors for the 3x1 MSPL [142], 6x1 groupe-mode-specific photonic lantern (GMS-PL) [66], and 10x1 GMS-PL [160].

## 3.6 Applications

PLs are optical devices that map the fundamental modes from several single-mode fibers into the propagation modes of a multimode fiber, each with its specific field profile. MSPLs constitute a subclass of PLs that uses the symmetry-breaking properties of the optical structure to feature a one-to-one mapping between the unique mode of a few single-mode fibers and each mode of the multimode fiber. This capability offers great promises for optical communications, remote sensing, and biomedical imaging. Here, we use SuPyMode to assist in the design of an MSPL and further demonstrate mode-skipping : the ability to pick higher-order modes without exciting all of the lower-order ones.

### 3.6.1 Mode-Specific Photonic Lantern Design

The fundamental principle behind photonic lanterns is based on mode coupling, which enables the transfer of energy between modes defined by different propagation constants and field structures. By carefully designing the arrangement and geometry of the photonic lantern, one can control the modal behavior of the input beam and achieve the desired output characteristics. MSPLs have gained significant attention in recent years due to their unique properties and potential for various practical applications. As previously mentioned, SuPyMode can calculate the modal coupling of a tapered optical structure. However, a more significant parameter to explore is the adiabatic criterion, as it characterizes the modal behavior as a direct function of the tapering process. For some applications, such as in the case of photonic lanterns, it is desirable to avoid modal coupling within the coupler. From

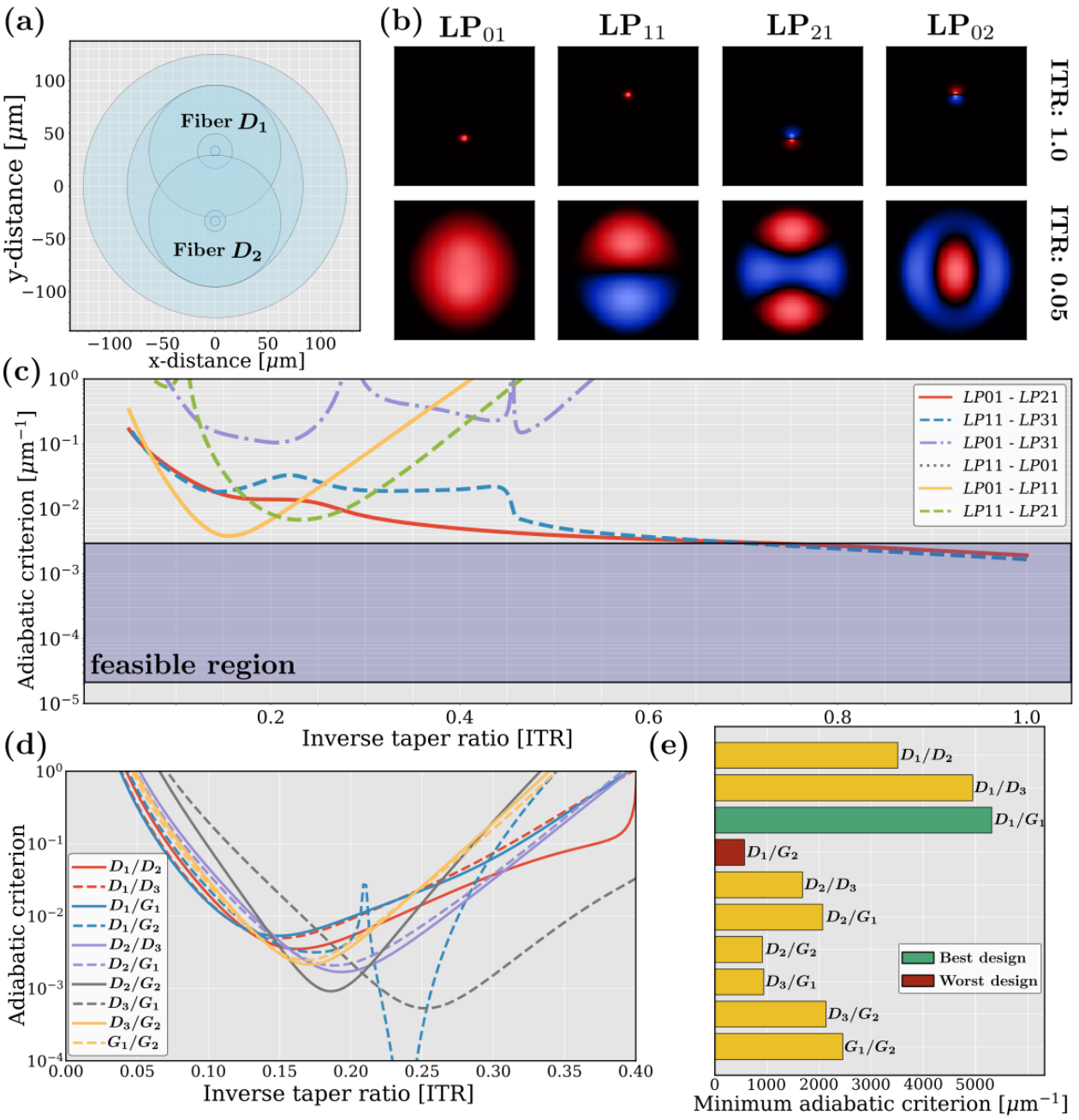



FIGURE 3.5 Design of a 2x1 MSPL based on an A-B structure using SuPyMode. (a) The configuration of the simulated structure highlights the position of each of the fibers : Fiber A and Fiber B. (b) The field structure of the computed modes. For visualization purposes, only four modes are depicted here. (c) The adiabatic criterion of the taper structure. The blue area represents a standard in-lab feasible region with coupler length varying from 1 mm to 30 mm. Comparison of the different 2x1 MSPL designs using fibers from Table 3.1. (a) Adiabatic curves for each design in the ITR region ranging from 0.05 to 0.4. (b) Comparison of the minimum adiabatic values in the same region. The higher the figure, the more robust the component to modal cross-talk.

Eq. (3.8), this implies that we aim to achieve a high adiabatic value at every point in the coupler. As the adiabatic criterion is independent of the tapering process, it can serve as a metric to optimize the fiber structure to minimize modal coupling. The selection of the fiber type and model to manufacture photonic lanterns aims to ensure low cross-talk and wavelength-independent optical behavior. Different approaches have been exploited in the past to improve MSPLs. Among the different techniques, we can note the use of graded index fibers [66, 160] and more recently double-clad fibers [35, 57]. The first approach makes use of graded-index fibers with different core sizes to reduce the modal cross-talk and lift the mode degeneracy of large modal content MSPLs (over 10 modes). While the approach is very promising, having numerous different core radii can be an impediment for the end-user who has to splice to a standard fiber model. The other approach, using double-clad fibers, has also been demonstrated to improve the adiabatic criterion, allowing for smaller and more robust components with lower modal cross-talk. In contrast with the graded-index fibers, multi-clad fibers are usually manufactured to be readily spliced to standard fibers. As both approaches have demonstrated their efficacy in developing MSPLs for a given application, the issue of which method to employ for a particular application remains an open question. In that regard, SuPyMode is a very convenient tool to tackle the issue. To illustrate the potential application of our study, we present a series of diverse conceptual designs for a basic 2x1 MSPL and subsequently evaluate their respective simulation results. Drawing inspiration from the work of [33, 35, 160], we introduce and analyze several novel fabrication techniques relying on different fiber structures, as presented in Table 3.1.

TABLE 3.1 Fiber models, used for the design optimization. The DCF fibers were also used in [33] and GIF are extracted from [160].

| **Double clad fibers (DCF)** | | | | |
|---|---|---|---|---|
| Fiber name | Core diameter [µm] | Core NA | Inner-clad diameter [µm] | inner-clad NA |
| $D_1$ | 9.2 | 0.125 | 33 | 0.11 |
| $D_2$ | 9.2 | 0.12 | 20 | 0.11 |
| $D_3$ | 9.2 | 0.12 | 13 | 0.11 |
| **Graded-index fibers (GIF)** | | | | |
| Fiber name | Core diameter [µm] | | $\Delta$n | |
| $G_1$ | 12 | | $16.10^{-3}$ | |
| $G_2$ | 18 | | $16.10^{-3}$ | |

The simulation outcomes for the $D_1$-$D_2$ configuration are presented in Figure 3.5. Figure 3.5 (b) depicts the computed mode fields at different ITR values. From that figure, we understand that the fundamental modes of Fiber $D_1$ and Fiber $D_2$ map to the $LP_{01}$ and $LP_{11}$ mode,

respectively, at low ITR values. Thus, we designate those modes as fundamental. Any coupling between fundamental modes leads to cross-talk while coupling with non-fundamental modes is included in losses. Figure 3.5 (c) presents the adiabatic criterion for each pair of computed modes. After analyzing the adiabatic curve (LP01-LP11), we conclude that the fundamental modes start to couple at an ITR value of roughly 0.2, which corresponds to the lowest adiabatic value between the relevant modes. Interestingly, this occurs coincidently with the modes leaking their cores to occupy the second cladding. While avoiding crossing the adiabatic criterion curve of the $LP_{01}$-$LP_{11}$ pair ensures low cross-talk, one must also consider the other curves to avoid coupling with cladding modes, which ultimately convert into losses. The present study presents a comparison of the adiabatic criterion values for the fundamental modes in the vicinity of an ITR value of 0.2 for various fiber designs, resulting from permutations of the fibers listed in Table 3.1. The results are illustrated in Figure 3.5 (d). It is noteworthy that the optimal design corresponds to a combination of double-clad fiber and graded-index fiber, utilizing fibers $DCF_1$ and $GIF_2$ as shown in Figure 3.5 (e). In this particular case, we can also infer that DCF combinations lead to better results than GIF combinations.

### 3.6.2 Mode Skipping

The utilization of MSPLs has been demonstrated beyond the telecommunications space, as exemplified in the application of optical tweezers [162] and imaging [29]. The use of MSPLs provides precise control over the field structure that interacts with the sample. However, limitations related to the manufacturing process restrict the available field structures. Recent research on MSPLs has focused on extending the optical structure to encompass higher-order modes, which increases the complexity of the fabrication process, leading to a reduction in manufacturing yield. Accessing higher-order modes through simpler optical structures with precise designs is achievable, and herein is referred to as mode-skipping. However, the experimental harnessing of such designs can prove to be challenging. Specifically, it requires the modal-crossing of the propagation constant before interaction between the modes occurs, as it was briefly mentioned in [66]. In other words, the modal-crossing must occur before the modes start to leak into the common cladding, where they interact as shown in Figure 3.6. Furthermore, the diminished spacing between the propagation constants of higher-order modes increases the likelihood of mode-crossing. Figure 3.6 (c) shows a particular instance of mode-skipping, allowing a simple 2x1 MSPL to generate the $LP_{01}$ and $LP_{21}$ modes. In Figure 3.6 (c), we notice four adiabatic criterion dips which correspond to the $LP_{22}$ (i), $LP_{31}$ (ii), $LP_{02}$ (iii) and $LP_{11}$ (vi) mode crossing, respectively. While the three first (i-iii) modal-crossing do not entail mode-coupling, the last one (iv) involves a strong

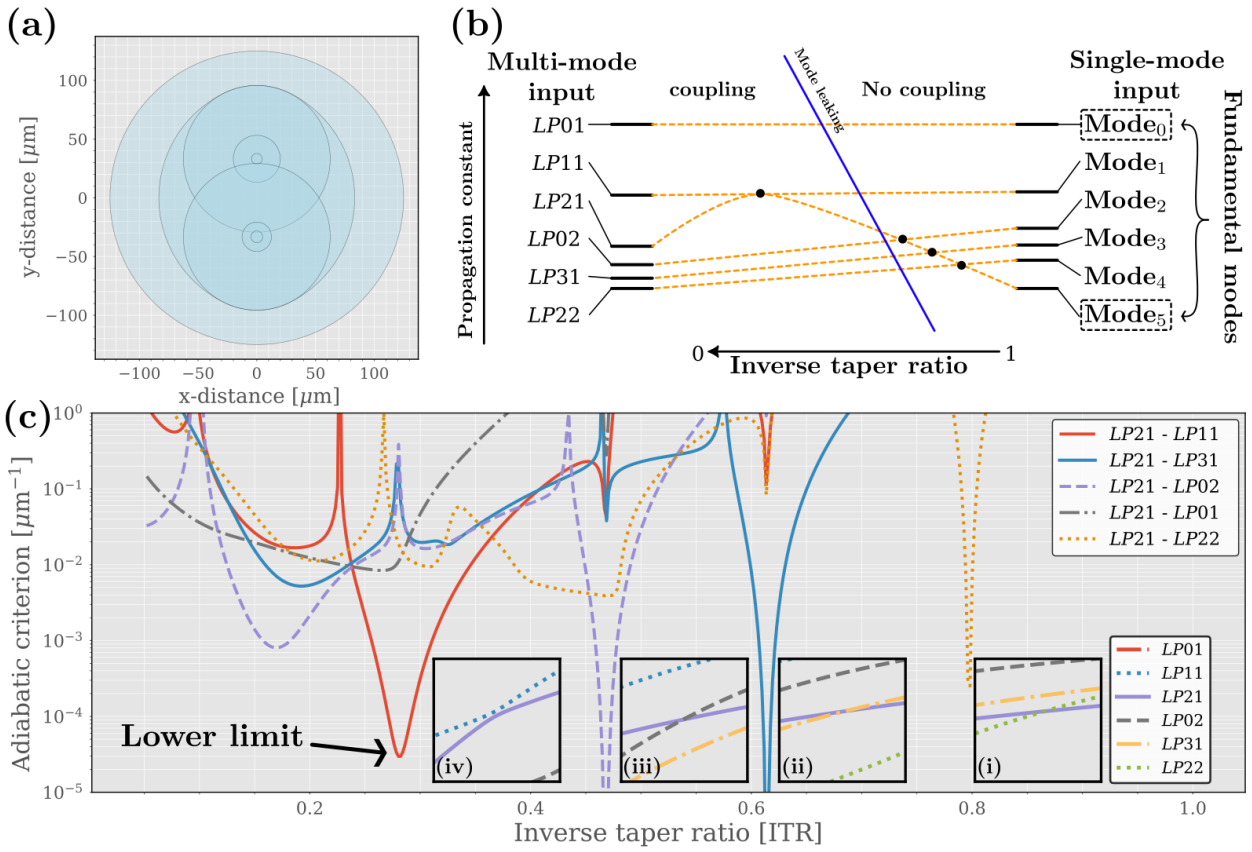



FIGURE 3.6 Depiction of the mode-skipping process. (a) 2x1 asymmetric optical structure that allows for $LP_{01}$ and $LP_{21}$ generation. (b) Depiction of the mode propagation constant and coupling behavior as a function of the ITR. The mode-leaking line separates the coupling vs. no-coupling region. The black dots on the orange curves indicate points of interest. (c) Adiabatic criterion for the optical structure, six first propagation modes. Subset (vi) highlights an avoided crossing, which signifies strong coupling, while (i-iii) are non-interacting crossings that do not account for mode-coupling as the crossing occurs before any mode-leaking can take place.

coupling as implied with the avoided-crossing of the propagation constants. This coupling can, however, be circumvented using a long taper process (heating length over 20 mm), as shown in Figure 3.3.

## 3.7 Discussion

The SuPyMode software tool has been devised to simulate mode propagation in fiber optic components. However, as with any simulation software, there exist several constraints that may give rise to discrepancies between the predicted outcomes and experimental measurements. One of the key limitations pertains to the discretization of the optical structure. To perform numerical design of larger structures, a higher number of pixels is required. As a consequence of the increased number of pixels, the computational time is also increased. In addition, disparities between the simulated and experimentally fused structures may lead to discrepancies between the predicted and measured values. The magnitude of these disparities may vary depending on the specifics of the manufacturing process. Moreover, the application of strain on the fibers during the fusing process may result in a deviation of the fiber core from its initial position. The SuPyMode core scrambling parameters can be employed to assess the extent of this effect. Lastly, it should be noted that SuPyMode relies on the scalar approximation to compute the modal behavior in the optical component. This approximation is valid under the weakly guided regime. However, in cases where the component undergoes a strong tapering process, modes that are guided in the silica structure with a clad formed by the surrounding air may be generated. In such configurations, full vectorial computation is required, as it was explored in [135]. To prevent this situation, it is necessary to employ a capillary tube with a lower refractive index, as previously described in [35, 91, 160].

**Funding**

Fonds de Recherche du Québec - Nature et technologies (FRQNT) #304141 (MPDSH), Natural Sciences and Engineering Research Council (NSERC) of Canada grants #RGPIN-2018-06151 (CB), #RGPIN-06404-2016 (NG).

**Disclosures**

The authors declare that there are no conflicts of interest related to this article.

**Data Availability**

The source code for SuPyMode is available at https ://github.com/MartinPdeS/SuPyMode. The raw data used in the article data is available from the authors upon reasonable request.

# CHAPTER 4 DESIGN OF PHOTONIC LANTERNS COMPONENT USING SUPYMODE, AN OPEN-SOURCED PYTHON LIBRARY

## 4.1 Chapter Context

This chapter renders a detailed exposition of the design principles governing modally-specific photonic lantern (MSPL). Employing the metric provided methodology outlined in Chapter 3, we exemplify the application of the adiabatic criterion as a pivotal design parameter for the fabrication of 3- and 4-mode MSPL structures, engineered to exhibit minimal cross-talk and losses.


### Abstract

Photonic lanterns are a new type of tapered fiber optics component that have been stirring a lot of attention lately as they have found extensive applications in various fields, including telecommunications, sensing, and photonics. The design and optimization of these components are crucial for achieving desired optical functionalities. SuPyMode, a versatile Python library, addresses the challenge of simulating light propagation in tapered fiber optics components by employing eigenmode expansion (EME) and coupled-mode theory (CMT) in a pipe-line enabling the precise design and analysis of tapered fiber components.


## 4.2 Introduction

With the recent emergence of the photonic lantern (PL) [18], the scientific community has seen a resurging interest in the design of fiber taper structure. Emerging as a transformative fiber optics component, PLs enable the seamless transition of light between individual modes of single-mode fibers and the modes of a multimode fiber. This unique capability stems from their specialized design, where multiple single-mode fibers adiabatically merge into a single multimode waveguide. Their potential has been quickly recognized in areas such as astrophysics [91], where they facilitate efficient light collection, and in high-capacity optical communication systems, enhancing bandwidth without compromising on signal fidelity [92]. Furthermore, their applicability extends to the realm of imaging, introducing innovative features to be exploited [29, 34]. As the scientific community intensifies its focus on understanding and optimizing these new components, tools like SuPyMode play a critical role. By encompassing functionalities for in-depth analysis of light propagation in tapered

components, SuPyMode provides an integrated platform for photonics research and applications. In this work, we present the theoretical framework upon which SuPyMode is built, and validate the package by presenting a juxtaposition of simulation predictions and experimental results for a MSPL with very low modal cross-talk.

## 4.3 Method

SuPyMode employs a combination of EME framework and CMT to simulate light propagation in tapered fiber optics components. The library leverages the geometric properties of tapered structures, particularly homothetic transformations, to calculate the adiabatic criterion for each pair of propagating modes, a critical parameter in optimizing taper structures. The adiabatic criterion, defined as

$$\alpha_{ij} = \frac{\sqrt{\beta_i \beta_j}}{\pi k^2} \left( \int_A \psi_i \, \psi_j^* \, \frac{\partial n^2}{\partial r} \, r \, \mathrm{d}A \right)^{-1}, \tag{4.1}$$

is computed for each pair of propagating modes $i$ and $j$ for which $\hat{\psi}_i$ and $\beta_i$ are respectively the L2-normalized mode field and propagation constant of the $i^{th}$ mode [24]. In this equation, $k$ is the wavenumber, and $n$ is the refractive index profile of the tapered structure. The adiabatic criterion represents a quantitative measurement expressing the propensities of modal coupling for a given pair. A low value of this criterion signifies increased challenges in designing a component that precludes such coupling. Figure 4.1 illustrates the application of the adiabatic criterion in component design. Subfigure 4.1 (a) delineates the normalized longitudinal profile of tapered structures (represented with the inverse taper ratio) across four distinct heating lengths, given an equivalent stretching distance. The parameters, namely heating length and stretching distance, are explicitly defined in [19]. It is discernible that a reduction in the heating length results in a pronounced transition slope, rendering the component comparatively compact—an attribute often associated with enhanced component robustness. Nonetheless, invoking the CMT for tapered structures, an accentuated slope corresponds to augmented propensities for mode coupling. The metric used to assess the tendency of mode coupling is defined as the logarithmic derivative of the characteristic transverse length scale :

$$s(z) = \frac{1}{\rho(z)} \frac{\mathrm{d}\rho(z)}{\mathrm{d}z}. \tag{4.2}$$

Figure 4.1 (b) presents the adiabatic criterion as a function of the inverse taper ratio (defined as the reduction factor of the structure) for pairs of modes of a three-mode MSPL. Along the adiabatic criterion curves is depicted the corresponding logarithmic derivative of the

characteristic length scale associated with the heating length. Such graphical representations serve as vital indicators in assessing the viability of a given design. The curves corresponding to the adiabatic criterion of the modes delineate the relative ease with which modes couple in comparison to the taper curves, illustrated in black. Should the adiabatic criterion lie below the taper curves, it indicates an anticipated pronounced coupling behavior between the modes. Based on the provided data, it can be inferred that only the fiber component with a heating length of 4.0 and 8.00 mm do not induce mode coupling. This characteristic is frequently considered essential in the design of optical fiber couplers. SuPyMode provides a user-friendly Python API that allows users to define tapered structures, facilitating rapid experimentation. To ensure efficient numerical computations, the library integrates a C++ computing core, enabling it to handle complex simulations swiftly. This methodology allows SuPyMode to be a versatile and powerful tool for researchers and engineers in the field of photonics, as demonstrated through its application in designing PLs and other tapered fiber optics components.

## 4.4 Photonic Lantern Design

One of the prominent applications of SuPyMode is the design of PLs. PLs are essential components for mode conversion and beam shaping in optical communication systems and astrophotonics. Several subclasses, including the MSPL, groupe-mode-specific photonic lantern (GMS-PL), and hybrid variants, are similar in their avoidance of modal coupling and the manifestation of specific symmetries. Extensive resources are being dedicated to exploring the design space for this type of component due to the absence of currently accepted industry standards. For example, the application of graded-index fibers with varying core sizes has been investigated for the development of high-modal content PLs [67, 161]. More recently, an alternative approach involving the use of double-clad fiber (DCF) has been examined, offering the potential advantage of improved integration with existing standard fiber models [35]. SuPyMode enables the exploration of various geometries and parameters to optimize the performance of PLs, ultimately enhancing their efficiency and applicability. Figure 4.2 depicts both simulation results and experimental implementations of a 3– and 4–mode MSPL, derived from a design selected through the utilization of the SuPyMode computational tool.

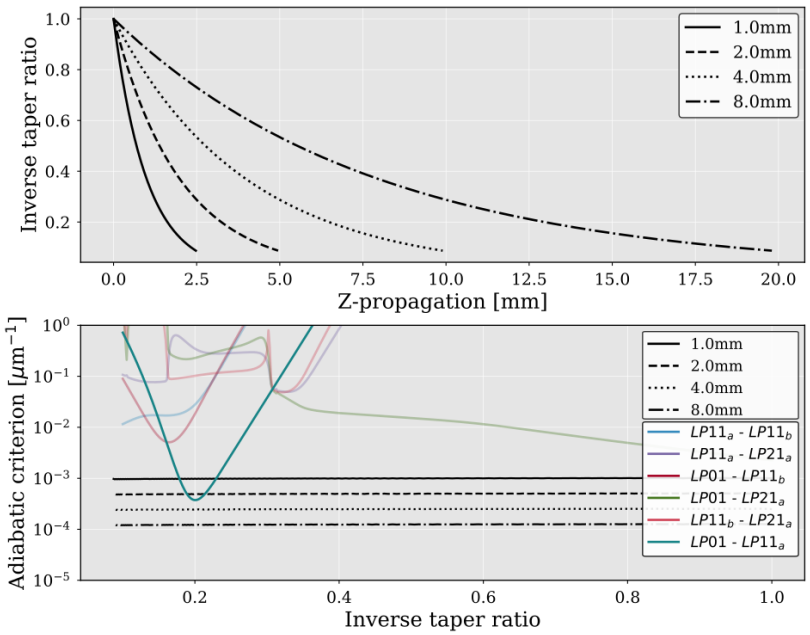



FIGURE 4.1 Fiber taper parametrization. (a) Depiction of different taper fiber profiles as a function of the heating length. (b) Adiabatic criterion of propagation mode couple and the adiabatic factor associated with each heating length. Within this subfigure, particular attention is directed towards the LP01-LP11$a$ adiabatic criterion due to its lower magnitude in comparison to other criteria.

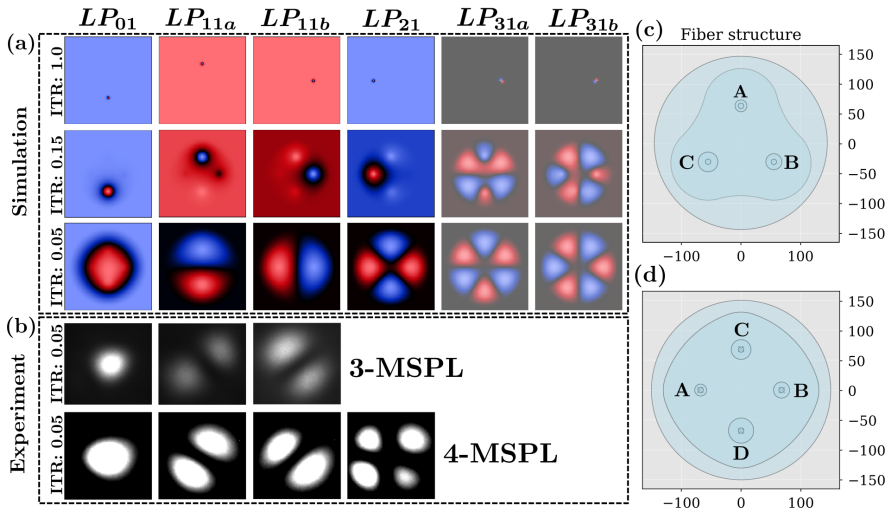



FIGURE 4.2 Comparison of simulation and experimentation for MSPL design. (a) Simulation of the modes field for the 4-mode configuration depicted in (d) at different localization in the tapered component (MSPL) which are associated to different inverse taper ratios (ITR). The two modes dimmed are higher-order excitation of the DCFs, and are usually disregarded. (b) Experimental measurements of the mode field generated by a 3– and 4–mode MSPL ; (c, d) Optical structure employing three (and four) different DCF and an outer capillary tube for the 3– and 4–mode configurations, respectively.

## 4.5 Conclusion

SuPyMode is a powerful and versatile Python library that employs EME and CMT to simulate light propagation in tapered fiber optics components. Its flexible API, combined with the computational efficiency of its C++ core, makes it a valuable tool for researchers and engineers working in photonics. In this work, we demonstrate the utility of SuPyMode in the design of PLs, showcasing its potential through real-world implementations.

# CHAPTER 5 ARTICLE 2 : PYMIESIM : AN OPEN-SOURCE LIBRARY FOR FAST AND FLEXIBLE FAR-FIELD MIE SCATTERING SIMULATIONS

This chapter was adapted from : **Martin Poinsinet de Sivry-Houle**, Nicolas Godbout, and Caroline Boudoux, "PyMieSim : an open-source library for fast and flexible far-field Mie scattering simulations," Opt. Continuum 2, 520-534 (2023), submitted on October 11, 2023.

## 5.1 Author Contribution

The article on which this chapter is based was submitted to Optics Continuum, published on March 2023. Martin Poinsinet de Sivry-Houle is the first author of the publication and contributed to 90% of the work. Nicolas Godbout and Caroline Boudoux were senior investigators and assisted in the manuscript revision.

## 5.2 Chapter Context

This chapter delves into the specifics of PyMieSim, a software tool designed to extensively study the optical interactions among the source, scatterer, and detector. Developed to facilitate a detailed understanding of Mie scattering interactions, PyMieSim incorporates various detection schemes to model and predict contrast mechanisms. While primarily targeted towards aiding particle sensing in the context of biomedical imaging, the software also aims to demonstrate the possibility of achieving sub-resolution sensing through structured light detection schemes. The software's potential is supported by a range of case studies that underline its practical utility and adaptability. However, it is important to note that the transformation of biomedical imaging through improved Mie scattering analysis and enhanced contrast mechanisms is a complex and multi-faceted endeavor that extends beyond the capabilities of a single software tool. Despite this, PyMieSim presents a promising direction for future research, potentially illuminating new paths in the exploration of Mie scattering interactions and sub-resolution sensing.

## Abstract

Mie scattering simulations are essential to designing sensing and imaging devices for atmospheric and biomedical sciences applications. Current simulators based on Lorenz-Mie theory

allow obtaining scattering phase functions for several scatterer geometries. Still, they are not optimized for simulating ranging parameters and do not compute coupling powers into coherent or incoherent detectors. Here, we present PyMieSim : a Python interface wrapping a C++ parallelized core for a fast, flexible, and highly visual simulation package allowing for the study of ranges of parameters for different source, scatterer, and detector configurations. We demonstrate two applications : flow-cytometry geometry optimization and few-mode optical coherence tomography contrast analysis.

## 5.3 Introduction

Light-particle interactions are at the heart of a wide range of technologies, from biomedical imaging to solid-state physics [22,113]. In particular, numerous biomedical optics applications rely upon light scattering interactions for early diagnosis of cancer [72] or a variety of diseases, such as Alzheimer's [39]. Understanding such complex interactions between light sources, scatterers, and detectors is of prime importance in validating experimental results and theoretical predictions. Optical configurations composed of a source, scatterer, and detector (SSD) are defined by several attributes, resulting in systems of high dimensionality. Although the source and scatterer interaction can be challenging to solve, under certain conditions [59], the scatterer can be approximated to a geometry sporting symmetries such as a sphere, simplifying the mathematical expressions and, thus, enabling the use of fast simulation tools, such as the Lorenz-Mie scattering theory (LMT). The LMT framework allows finding exact solutions to Maxwell's equations for some scatterer geometries such as homogeneous spheres, stratified spheres, or circular cylinders, albeit using planewave illumination. Bohren and Huffman's Fortran codes [22] for such a framework have been widely used and adapted in several programming languages, providing an essential tool for experimental validation and theoretical predictions. Python is currently a prevalent, interpreted programming language [158] that has become pivotal for scientific applications, notably due to its wide range of available libraries [112, 117], exportability, and flexibility. Presently, a few Python/C++ projects exist for LMT such as PyMieScatt (Python) [148], MieLab (Python) [119] or Bim-Sim (C++ ) [14]. These do not emulate interactions with detectors (coherent or incoherent), and nor are they suitable for studying optical properties of large sets of configurations. Moreover, as these projects are written exclusively in Python or C++ , they inherit either the slowness or complexity of the associated programming language. In this paper, we present PyMieSim, a fast and flexible Python library wrapping a C++ /Fortran core for simulating a wide range of SSD configurations with a much-reduced run time. The library allows defining a complete SSD system to compute the full scattered field (over 4 $\pi$ steradian), properties such as effi-

ciencies (scattering, extinction, absorption, and radiation pressure), asymmetry, and albedo parameters, as well the coupling between the far-field scattered wave and a detection scheme (incoherent detector or coherent optical fibers). PyMieSim comprises three different LMT solvers, each one computing solutions of Maxwell's equations for different scatterer form factors : homogeneous spheres, 2-layer spheres, and perpendicularly illuminated infinite circular cylinders. Whilst there exists a few libraries allowing for the study of source-scatterer interactions [86, 129, 148], none allow evaluating interaction with a detector. More importantly, other packages are not suitable for studying the optical properties of a large set of optical configurations with the required short compute time. By contrast, PyMieSim allows the simulation of coherent detection schemes like fiber optic modes or incoherent schemes like photodiode detectors. PyMieSim offers more than two orders of magnitude in reduced compute-time over all comparable publicly-available packages. In the following sections, we discuss the most important aspects of the scattering algorithm implemented in PyMieSim, validate its results against state-of-the-art algorithms, and demonstrate typical simulations, including various detection geometries.

### 5.3.1 Lorenz-Mie Theory Applications

Lorenz-Mie scattering theory (LMT) is a central framework for describing various processes that are at the core of several technologies and studies. LMT makes use of electric and magnetic multipole expansions to compute the scattered near- and far fields. Originally, LMT packages only allowed computing solutions for homogeneous spheres [111]. Since then, various geometries were adapted, including infinite cylinders [150], stratified spheres [119], and others [46]. The analysis of such solutions as a function of the scattering event parameters may serve many applications in biomedical optics, such as light scattering spectroscopy (LSS) [155] or surface plasmon resonance enhancement, respectively. Solutions to Mie scattering may also be used for particle sizing [159], absorption quantification through the atmosphere [23], sensing of cells in biological tissues [11], flow cytometry [156], and also in metamaterial design [170]. While the LMT framework is bound to assume planewave illumination and is limited to certain scatterer geometries, it is widely used as a first-order approximation for more complex configurations. The generalized Lorenz-Mie scattering theory (GLMT) framework is an extension of LMT that enables defining an arbitrary illumination source to compute the scattering attribute. However, GLMT is more computationally expensive—especially when rotational symmetry is broken—as it usually involves computing higher-order terms of beam decomposition [130].

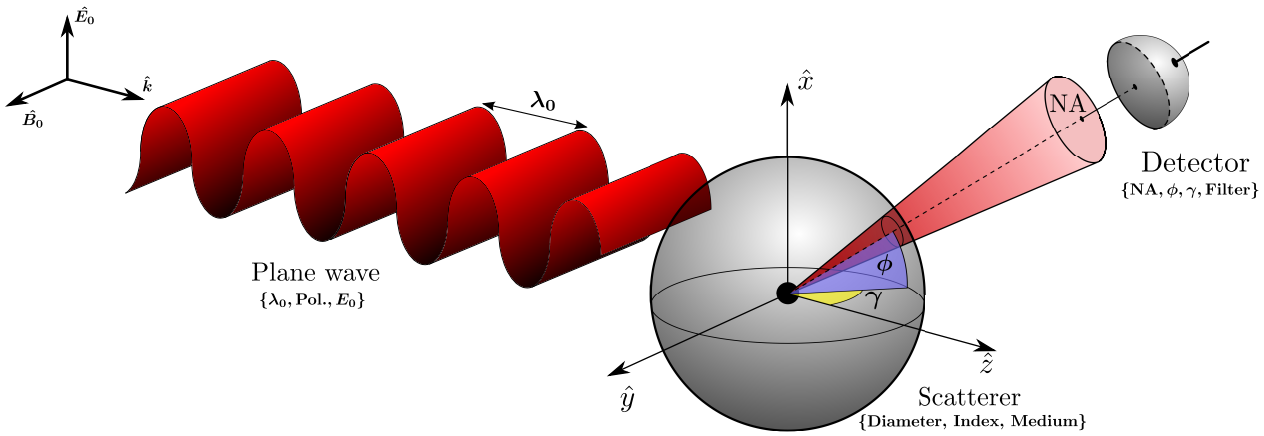



FIGURE 5.1 Representation of a scattering event configuration. An incident planewave (wavelength $\lambda_0$, polarization and electric amplitude $\vec{E}_0$, and wavevector $\hat{k}$) interacts with a homogeneous spherical scatterer (diameter $d$, and index, $m_{\text{sca}}$) immersed in a medium (index $m_{\text{med}}$). The resulting scattered wave (not shown) is projected onto an incoherent detector (numerical aperture NA, and angular location $\gamma$ and $\phi$) through a polarizing filter (not shown). Alternatively, PyMieSim allows replacing the incoherent detector with a coherent detection scheme (not shown) such as a single- or few-mode optical fiber (defined as a superposition of the scattered field onto several LP propagation modes).

## 5.4 Theory

PyMieSim is a Python package that was developed to provide a novel tool for the extensive study of light scattering interactions. In order to simulate a scattering event as shown in Fig. 5.1, PyMieSim exploits the LMT framework. From this, the library can output various scattering properties, compute the scattered far fields and compute the coupling between the latter and different detection schemes.

### 5.4.1 Optical Setup

Figure 5.1 shows a typical geometry for a scattering event defined using variables found in the package. Illumination is described using the wavelength in vacuum, $\lambda_0$, the polarization, $\hat{E}_0$ and amplitude $|E_0|$. A scatterer (either a homogeneous sphere, a stratified sphere, or an infinite cylinder) is described through its diameter, $d$, its refractive index, $m_{\text{sca}}$, and that of the surrounding medium, $m_{\text{med}}$. A detector defined with a numerical aperture (NA) is placed at an inclination and azimuthal angles $\phi$ and $\gamma$, respectively, accepts two orthogonally polarized scattered fields that can be specifically selected with a polarization filter. The detector coupling mechanism can also be set to coherent or incoherent, such as a photodiode or linearly polarized (LP) propagation modes in an optical fiber, respectively.

### 5.4.2 Lorenz-Mie Theory

The standard LMT provides a mathematical framework that enables numerical methods to infer scattering properties of a scatterer planewave interaction. While approximate algorithms such as the anomalous diffraction [69] or Wiscombe approximation [166] were developed to accelerate the computation, the need for such speed up has been decreasing with the evolution of central process unit (CPU) and graphical process unit (GPU) architectures and clock speed. As of today, a well-written exact solution algorithm can usually achieve the time-restrictive requirements of the end-user. For this reason, we will restrain ourselves to discussing exact solution algorithms. In particular, LMT returns the scattering matrix elements, denoted as $S_{1-4}$, and defined as

$$\begin{pmatrix} E_{\parallel}^{s} \\ E_{\perp}^{s} \end{pmatrix} = \frac{e^{ikr}}{ikr}. \begin{pmatrix} S_1 & S_4 \\ S_3 & S_2 \end{pmatrix} \begin{pmatrix} E_{\parallel}^{i} \\ E_{\perp}^{i} \end{pmatrix} \quad , \tag{5.1}$$

where $E^i$ and $E^s$ are the incident and scattered electric fields, respectively, $k$ is the wave-number, and $r$ is the distance from the scatterer. For a spherical scatterer, the $S_3$ and $S_4$ are null. Other useful coefficients are defined in

$$\vec{E}^s = E_0 \sum_{n=1}^{\infty} \frac{i^n(2n+1)}{n(n+1)} \left( i a_n \vec{N}_{e1n}^{(3)} - b_n \vec{M}_{o1n}^{(3)} \right) \quad , \tag{5.2}$$

where $\vec{N}_{e1n}^{(3)}$, and $\vec{M}_{o1n}^{(3)}$ are the vector spherical harmonics (VSH) as defined in [22]. LMT's exact algorithms usually represent the scattered far-field amplitudes as an infinite summation of VSH associated with electric and magnetic multipole coefficients, $a_n$ and $b_n$, respectively. The coefficients $a_n$ and $b_n$ are used to compute scattering and absorption efficiencies, for example. The VSH, also denoted as electric and magnetic multipoles, form a complete orthogonal basis for the decomposition of the scattered fields. The scattering near-fields are also defined within the LMT and are associated to the coefficients $c_n$ and $d_n$, which are not of interest in this paper. Most of the computational time for those algorithms is used to evaluate the scattering coefficient up to a certain order $n_{max}$. The scattering coefficients ($a_n$ and $b_n$) are derived using the Legendre and Bessel functions of order $n$, which are computed recursively. For calculations that do not involve near-field computing, Wiscombe's criterion is usually adopted [115]. This criterion defines the maximum order as

$$n_{max} = x + 4.05x^{1/3} + 2 \quad , \tag{5.3}$$

where $x = \pi d/\lambda$ is the size parameter, $d$ is the diameter of the scatterer, and $\lambda$ is the

incident wavelength in the surrounding medium ($\lambda = \lambda_0/m_{\text{med}}$). The homogeneous sphere, multilayer sphere and infinite cylinder are specific cases for which the scattering coefficients are well-defined as they lead to an analytical expression. In this paper, we follow the same mathematical notation as developed in [55] :

$$\begin{cases} \Psi_n(x) & = x\sqrt{\frac{\pi}{2x}}J_{n+1/2}(x) \\ \xi_n(x) & = x\sqrt{\frac{\pi}{2x}}H^{(1)}_{n+1/2}(x) \end{cases}, \tag{5.4}$$

with $J_n$, $H_n^{(1)}$ being the cylindrical Bessel and Hankel functions of the first kind, respectively. When a scatterer is also absorbing, its refractive index (RI) becomes complex, and so is the argument $x$ in Eq. (5.4). However, to the best of our knowledge, no C++ library implements complex argument Bessel functions. We therefore opted for a Fortran wrapper which exploits the Amos library [3] capable of such computations. Adopting this convention, and following Bohren and Huffman [22], we write the scattering coefficients $a_n$ and $b_n$ for the homogeneous sphere, infinite cylinder and 2-layer sphere as

homogeneous sphere
$$\begin{cases} a_n = \frac{\tilde{m}\Psi_n(\tilde{m}x)\dot{\Psi}_n(x) - \Psi_n(x)\dot{\Psi}_n(\tilde{m}x)}{\tilde{m}\Psi_n(\tilde{m}x)\dot{\xi}_n(x) - \xi_n(x)\dot{\Psi}_n(\tilde{m}x)} \\ b_n = \frac{\Psi_n(\tilde{m}x)\dot{\Psi}_n(x) - \tilde{m}\Psi_n(x)\dot{\Psi}_n(\tilde{m}x)}{\Psi_n(\tilde{m}x)\dot{\xi}_n(x) - \tilde{m}\xi_n(x)\dot{\Psi}_n(\tilde{m}x)} \end{cases}, \tag{5.5}$$

infinite cylinder
$$\begin{cases} a_n = \frac{\tilde{m}\dot{J}_n(x)J_n(\tilde{m}x) - J_n(x)\dot{J}_n(\tilde{m}x)}{\tilde{m}J_n(\tilde{m}x)\dot{H}_n^{(1)}(x) - \dot{J}_n(\tilde{m}x)H_n^{(1)}(x)} \\ b_n = \frac{\tilde{m}J_n(\tilde{m}x)\dot{J}_n(x) - \tilde{m}\dot{J}_n(\tilde{m}x)J_n(x)}{\tilde{m}J_n(\tilde{m}x)\dot{H}_n^{(1)}(x) - \tilde{m}\dot{J}_n(\tilde{m}x)H_n^{(1)}(x)} \end{cases}, \tag{5.6}$$

2-layer sphere
$$\begin{cases} a_n = \frac{\Psi_n(y)\left[\dot{\Psi}_n(\tilde{m}_2 y) - A_n(x)\dot{\xi}_n(\tilde{m}_2 y)\right] - \tilde{m}_2\dot{\Psi}_n(y)[\Psi_n(\tilde{m}_2 y) - A_n(x)\xi_n(\tilde{m}_2 y)]}{\xi_n(y)\left[\dot{\Psi}_n(\tilde{m}_2 y) - A_n(x)\dot{\xi}_n(\tilde{m}_2 y)\right] - \tilde{m}_2\dot{\xi}_n(y)[\Psi_n(\tilde{m}_2 y) - A_n(x)\xi_n(\tilde{m}_2 y)]} \\ b_n = \frac{\tilde{m}_2\Psi_n(y)\left[\dot{\Psi}_n(\tilde{m}_2 y) - B_n(x)\dot{\xi}_n(\tilde{m}_2 y)\right] - \dot{\Psi}_n(y)[\Psi_n(\tilde{m}_2 y) - B_n(x)\xi_n(\tilde{m}_2 y)]}{\tilde{m}_2\xi_n(y)\left[\dot{\Psi}_n(\tilde{m}_2 y) - A_n(x)\dot{\xi}_n(\tilde{m}_2 y)\right] - \dot{\xi}_n(y)[\Psi_n(\tilde{m}_2 y) - B_n(x)\xi_n(\tilde{m}_2 y)]} \end{cases}, \tag{5.7}$$

with
$$\begin{cases} A_n = \frac{\tilde{m}_2\Psi_n(\tilde{m}_2 x)\dot{\Psi}_n(\tilde{m}_1 x) - \tilde{m}_1\dot{\Psi}_n(\tilde{m}_2 x)\Psi_n(\tilde{m}_1 x)}{\tilde{m}_2\xi_n(\tilde{m}_2 x)\dot{\Psi}_n(\tilde{m}_1 x) - \tilde{m}_1\dot{\xi}_n(\tilde{m}_2 x)\Psi_n(\tilde{m}_1 x)} \\ B_n = \frac{\tilde{m}_2\psi_n(\tilde{m}_1 x)\dot{\psi}_n(\tilde{m}_2 x) - \tilde{m}_1\psi_n(\tilde{m}_2 x)\dot{\psi}_n(\tilde{m}_1 x)}{\tilde{m}_2\psi_n(\tilde{m}_1 x)\dot{\xi}_n(\tilde{m}_2 x) - \tilde{m}_1\xi_n(\tilde{m}_2 x)\dot{\psi}_n(\tilde{m}_1 x)} \end{cases},$$

where $x = kd_1/2$ and $y = kd_2/2$ are the size parameters for core and shell, respectively, with $d_{1,2}$ being the diameters of the associated scatterer layers, and $k$ the wavenumber. The dot ( $\dot{}$ ) represents a total derivative. The variable $\tilde{m}$ represents the relative RI of the scatterer, meaning that its value is divided by the RI of the medium. In the case of the 2-layer sphere, $\tilde{m}_1$ and $\tilde{m}_2$ represent the relative RI of the core and shell. Eqs. (5.5 - 5.7) assume a non-magnetic scatterer immersed in a non-absorbing medium.

### 5.4.3 Scattering Properties

While the scattering coefficients represent the amplitudes for the VSH, which do not describe measurable properties of the scattering event, they can be used to compute the scattering efficiencies and other parameters. Table 5.1 shows PyMieSim's output for each scatterer type. For the homogeneous and 2-layer sphere, PyMieSim computes the efficiencies for scattering ($Q_{\text{sca}}$), extinction ($Q_{\text{ext}}$), absorption ($Q_{\text{abs}}$), radiation pressure ($Q_{\text{pr}}$) and backscatter ($Q_{\text{back}}$), as well as the asymmetry parameter ($g$) and albedo ($\Lambda$), using the relations shown in the Table 5.1. These relations are based on the coefficients $a_n$ and $b_n$ described in Eqs. 5.5–5.7. However, due to the symmetry breaking for the infinite cylinder, the asymmetry parameter $g$ cannot be readily written in terms of the scattering coefficient $a_n$ and $b_n$. As such, PyMieSim evaluates the asymmetry parameter $g$ by computing the expected value of the inclination angle : $\langle \cos(\phi) \rangle$ (Equations not shown [22]). The cross-sections, $\sigma$, associated with the efficiencies can be retrieved, by multiplying $Q$ with the geometrical cross-section of the scatterer $A$ as

$$\sigma_i = Q_i * A \quad [\text{m}^2].$$

### 5.4.4 Coupling Mechanism

In addition to computing the scattering properties and scattering far-field, the PyMieSim package can evaluate the coupling of the scattering far-field with a specific detector. To do so, the solid angle space, where the far-field is evaluated, is generated using the Fibonacci lattice algorithm [151], which exhibits useful integration properties such as avoiding the local anisotropy of a conventional latitude–longitude array. The simulated detectors can be divided into two categories, namely, incoherent and coherent detection schemes. The first category embodies a system for which the output signal is proportional to the intensity of the impinging light field, such as a PIN diode. Such a detection scheme does not depend on the impinging field phase. The second category represents a system sensitive to the amplitude of the incident

TABLE 5.1 Scattering parameters computed by PyMieSim for spherical particles. PyMieSim also computes scattering parameters for infinite cylinders using equations found in [22] and reproduced in [126], but not included here for conciseness' sake.

| Parameter \ Scatterer | homogeneous sphere | 2-layer sphere |
|---|---|---|
| $Q_{\text{sca}}$ | $\frac{2}{x^2}\sum_n (2n+1)(\lvert a_n\rvert^2 + \lvert b_n\rvert^2)$ | |
| $Q_{\text{ext}}$ | $\frac{2}{x^2}\sum_n (2n+1)\mathfrak{Re}\{a_n + b_n\}$ | |
| $Q_{\text{abs}}$ | $Q_{ext} - Q_{sca}$ | |
| $Q_{\text{back}}$ | $x^{-2}\lvert\sum_n (2n+1)(-1)^n (a_n + b_n)\rvert^2$ | |
| $Q_{\text{ratio}}$ | $Q_{back}/Q_{sca}$ | |
| $Q_{\text{pr}}$ | $Q_{ext} - g\,Q_{sca}$ | |
| $g = \langle\cos(\phi)\rangle$ | $\frac{4}{Q_{sca}\,x^2}\left[\sum_n \frac{n(n+2)}{(n+1)}\mathfrak{Re}\{a_n\,a_{n+1}^* + b_n\,b_{n+1}^*\} + \sum_n \frac{(2n+1)}{n(n+1)}\mathfrak{Re}\{a_n\,b_n^*\}\right]$ | |
| $\Lambda$ | $Q_{ext}/Q_{sca}$ | |

light field, such as a single-mode fiber (SMF) or a few-mode fiber (FMF). Furthermore, the coherent coupling mechanism can be subdivided into two parts : centered coupling and mean coupling. The first case occurs when the scatterer is perfectly centered with the detector in comparison to the incident light field. In that case, following the same argument described in [125], we define the centered coupling as

$$\eta_{\text{centered}} = \left| \iint_{\Omega} \tilde{\psi}(\xi,\nu)^* \, \tilde{\phi}_{\text{det.}}(\xi,\nu)\, d\xi\, d\nu \right|^2 \quad , \tag{5.8}$$

where $\tilde{\psi}$ and $\tilde{\phi}$ are the far-field representations of the scattered light field and the detector, respectively, $\xi$ and $\nu$ are angles in spherical coordinates, and, finally, $\Omega$ is the solid angle subtended by the NA of the imaging system. The second case occurs when the scatterer is allowed not to be centered (said to be offsetted) with the detector, we thus define the mean coupling.

$$\eta_{\text{mean}} = \left\langle \left| \tilde{\psi}(\xi,\nu) \,.\, \tilde{\phi}_{\text{det.}}(\xi,\nu) \right|^2 \right\rangle_{\Omega} \quad , \tag{5.9}$$

For incoherent coupling mechanisms, the centered and mean couplings lead to the same results, as it does not depend on the phase of the scattering far field. Additionally, the PyMieSim software can also compute the scatterer footprint, which represents the coupling as a function of the scatterer spatial offset in two directions. Such a footprint is what we can

expect to see using a scanning system, as it was demonstrated in [125].

## 5.5 Main features of PyMieSim

PyMieSim was developed using an architecture promoting fast computing time and ease of operation under several platforms.

### 5.5.1 Architecture

Fig. 5.2 represents the structure of PyMieSim. The package takes advantage of the object-oriented aspect of Python to define three C++ classes : *Source* describes the incoming wave, *Scatterer* defines the scatterer geometry and attributes, and *Detector* defines the detector type, position, and attributes. Within the Python wrapper *Experiment*, *Source* and *Scatterer* interact together to return scattering efficiencies, while *Detector* returns the coupling ratio and scatterer footprint. The wrapping of these classes into a Python object is done using the PyBind11 library [73]. PyMieSim was developed in parallel with another Python package : PyOptik [124] to define the scatterer and immersion medium as specific materials with wavelength-dependent properties fetched from an online database (RefractiveIndex.info [127]). The code being composed of a Python wrapper for C++ , it has to be compiled and, as such, is operating system (OS) dependent. For portability, PyMieSim exploits the Python package manager with uploaded pre-compiled code (wheel format). PyMieSim is currently available on the three main OS : Linux, macOS, Windows for different Python versions : 3.7, 3.8, 3.9. Furthermore, the project also allows end-users to manually install the package for any system configuration. PyMieSim is also available on the online Google Colab platform and, thus, may be used on any OS.

### 5.5.2 Compute Time

Wiscombe's criterion, used to define the coefficient order, $n$, (see Eq. (5.3)) shows that the compute time rapidly increases for large size parameters, $x$. PyMieSim, written in C++ and Fortran, significantly reduces the runtime compared to existing Python packages, allowing for the study of a large set of SSD configurations up to large-size parameters. Figure 5.3 (a) shows the runtime comparison for scattering coefficient calculations using different software packages. The calculations were performed on a Linux distribution using an AMD Ryzen 5 2600 (6 cores) CPU and 16 GB of ddr4 ram, and show a gain exceeding 130x for large sets of parameters ($> 40\ 000$). PyMieSim's short computational time allows interfacing with other algorithms for fast post-processing, such as Mie inverse problems [27, 102]. Such gain permits

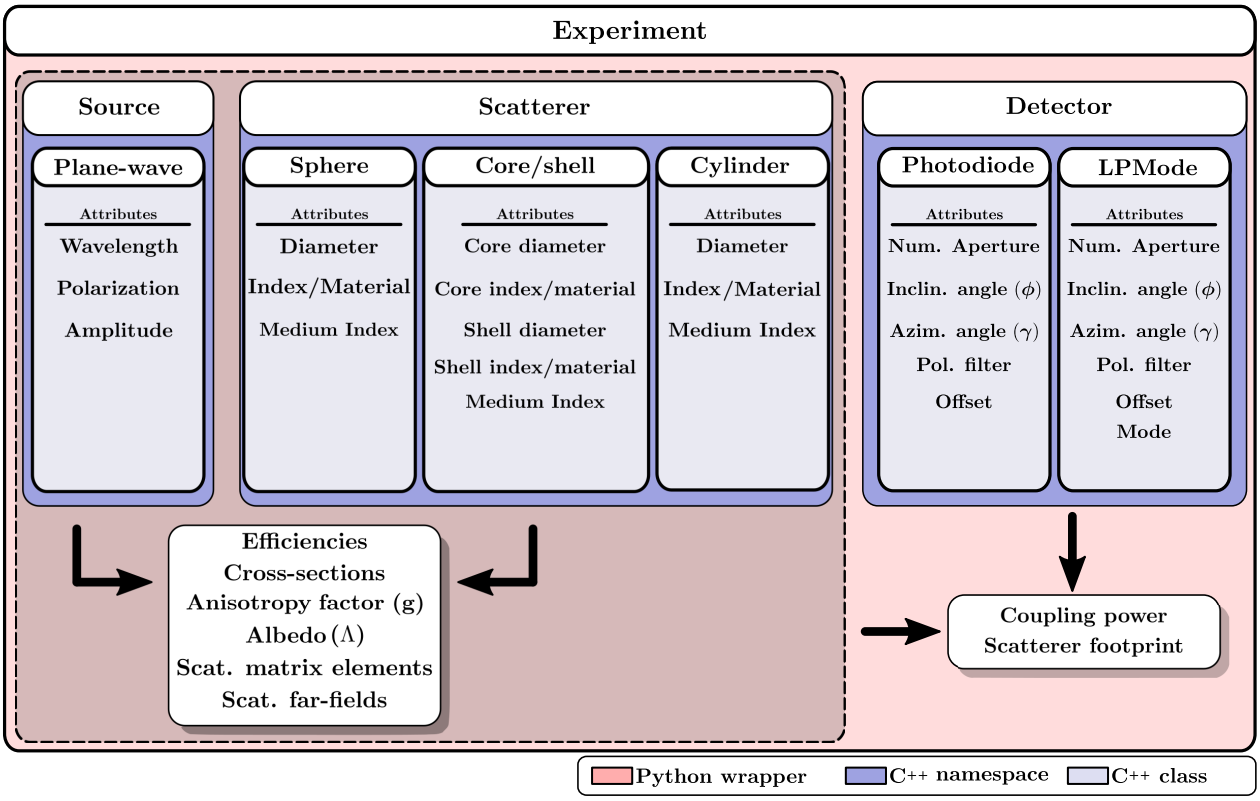



FIGURE 5.2 Representation of the structure and computing capabilities of the PyMieSim library, highlighting the numerous attributes defining the optical configurations.

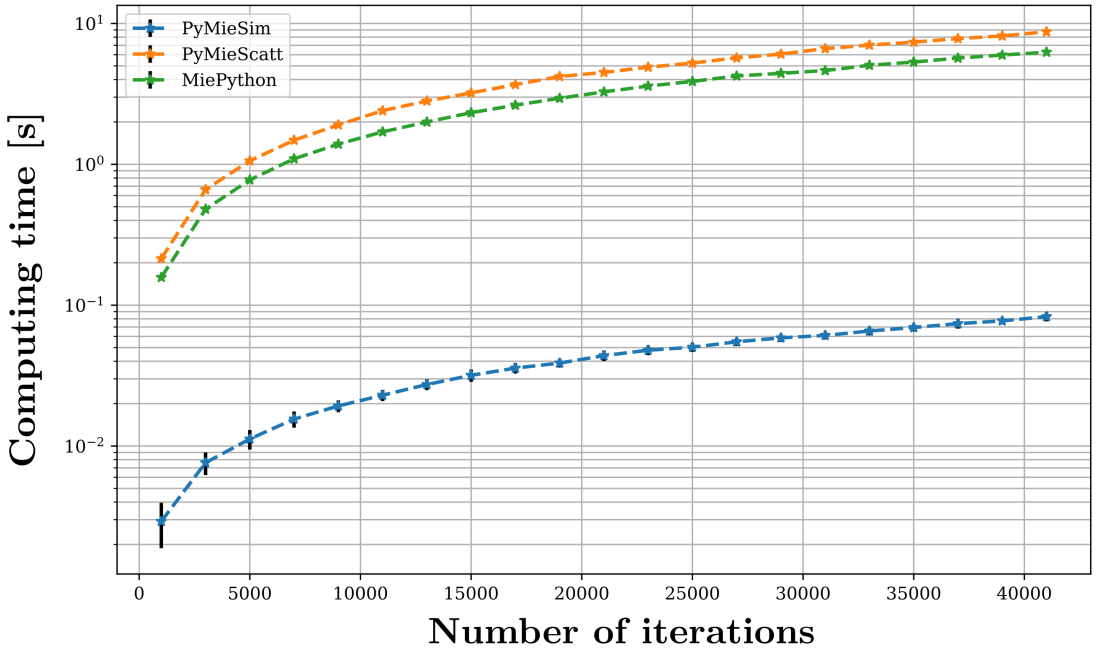



FIGURE 5.3 Library bench-marking presenting the computing time for scattering coefficient $An$ for scatterer with RI of 4, size ranging from 400 to 1000 nm and a source with a wavelength of 800 nm.

optimization tools to be used in conjunction with the library.

### 5.5.3 User Interface

PyMieSim simulates SSD configurations, which are composed of up to fourteen attributes, as shown in Fig. 5.2. The package gives to the end-user full control over each of those attributes, allowing to iterate over ranges for each one. Moreover, PyMieSim comes with an additional tool (DataVisual [121]) for high-dimensionality data operation, analysis, and visualization. PyMieSim provides a handy application programming interface (API), accompanied by visual tools at each level to grasp the optical configurations. PyMieSim is also a set of independent tools that allow the user to embed within another project. The software implements a seamless integration of the C++ outputted data with the scientific NumPy library [62], allowing the package to be readily implemented in any other Python project. Fig. 5.4 shows the simulation of the scattering event as depicted in Fig 5.1, for ranging values of detector's inclination angle $\phi$ and numerical aperture NA. The plots show that, as the NA of the detector increases, finer details in the scattering diagram vanish. Normalization is necessary to visualize all four curves, as increased NA results in increased coupling power, which the package allows calculating (not shown). Working examples of the code used to generate the plots shown in this paper can also be found at `https://pymiesim.readthedocs.io/en/latest/`. As such, simulation and visualization are important aspects for an exhaustive understanding of the involved mechanisms. PyMieSim makes use of different graphical tools to give better insight to the end user.

Fig. 5.5 shows examples of simulations performed using PyMieSim. Fig. 5.5 (a)–(c) show scattering experiments using a single scatterer ($d = 1000\,\text{nm}$, $m = 1.4$) and a linearly polarized planewave ($\lambda_0 = 500\,\text{nm}$). Fig. 5.5 (a) shows amplitude scattering matrix elements $S_1(\phi)$ (left) and $S_2(\phi)$ (right). Fig. 5.5 (b) shows a 3D rendering of the real and imaginary parts of the scattering phase function, while Fig. 5.5 (c) shows the far-field representation of the scattered intensity. Fig. 5.5 (d) shows different detector far-field representations. From left to right : an incoherent detector (NA=0.5), and three fiber modes : $\text{LP}_{01}$, $\text{LP}_{11}$, and $\text{LP}_{21}$. The LP far-field modes are computed using the Fraunhofer approximation.

## 5.6 Validation

Mie simulation results for the homogeneous sphere, the 2-layer sphere, and the infinite cylinder were extensively tested and compared to other libraries, namely : MiePlot [86], PyMieScatt [148], and MiePython [129]. However, to the best of our knowledge, no library

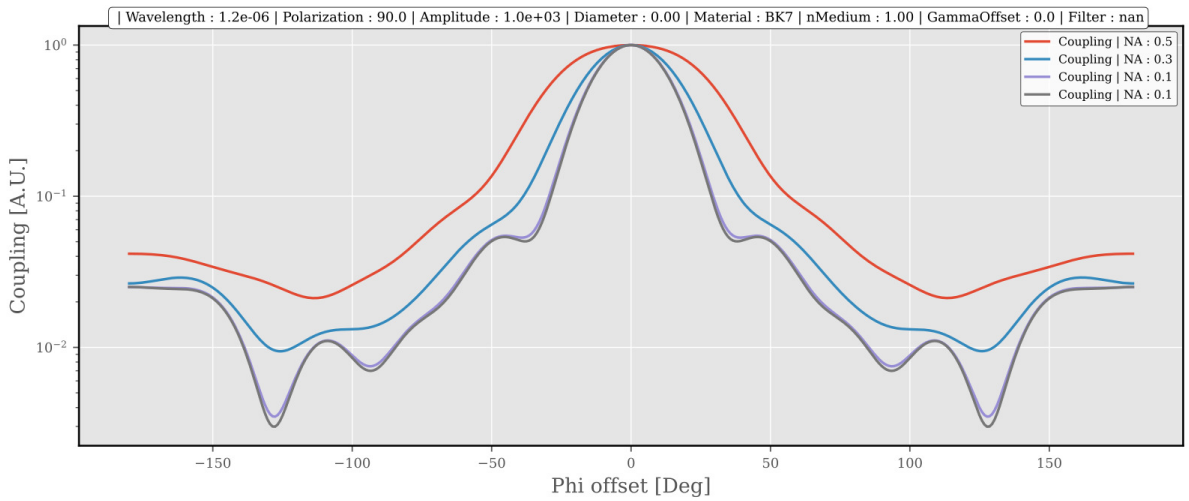



FIGURE 5.4 Results from the scattering experiment presented in Fig. 1 with $\lambda_0 = 1200$nm, $d = 2000$nm, and a particle composed of BK7 glass. Coupling power is evaluated for four different detector NA's displaced along the $\phi$ angle (and for $\gamma = 0$).

implements the scattering calculation for infinite cylinders. As such, we compared our results to the literature. Fig. 5.6 compares the scattering efficiencies for two orthogonal polarization, $Q_{scaI}, Q_{scaII}$, for a cylinder ($m = 1.55$) in air (red and blue curves) and in water (orange and green curves) with results published in [10,22] (black dashed curves). The four curves overlap perfectly.

## 5.7 Application

Here, we describe two use cases exploiting the unique features of PyMieSim, namely its fast compute core and the ability to simulate a coherent detection scheme.

### 5.7.1 Flow-Cytometry Optimization

PyMieSim's fast computing core allows using the library for optimization problems. For example, we demonstrate how PyMieSim could be used to improve the accuracy of a flow cytometry system through the optimization of its detectors' position. In its standard implementation, flow-cytometry uses two orthogonal photodetectors defined by the coordinates $\{\phi_0 = 0°, \gamma_0 = 0°\}$ and $\{\phi_1 = 90°, \gamma_1 = 0°\}$ in order to measure front and side scattering efficiencies of scatterers flowing one at a time through a monochromatic, polarized laser beam [107]. In this flow-cytometry optimization example, we define the optical system's baseline parameters as in [157]. We thus modeled scattering from spherical scatterers within a phase space

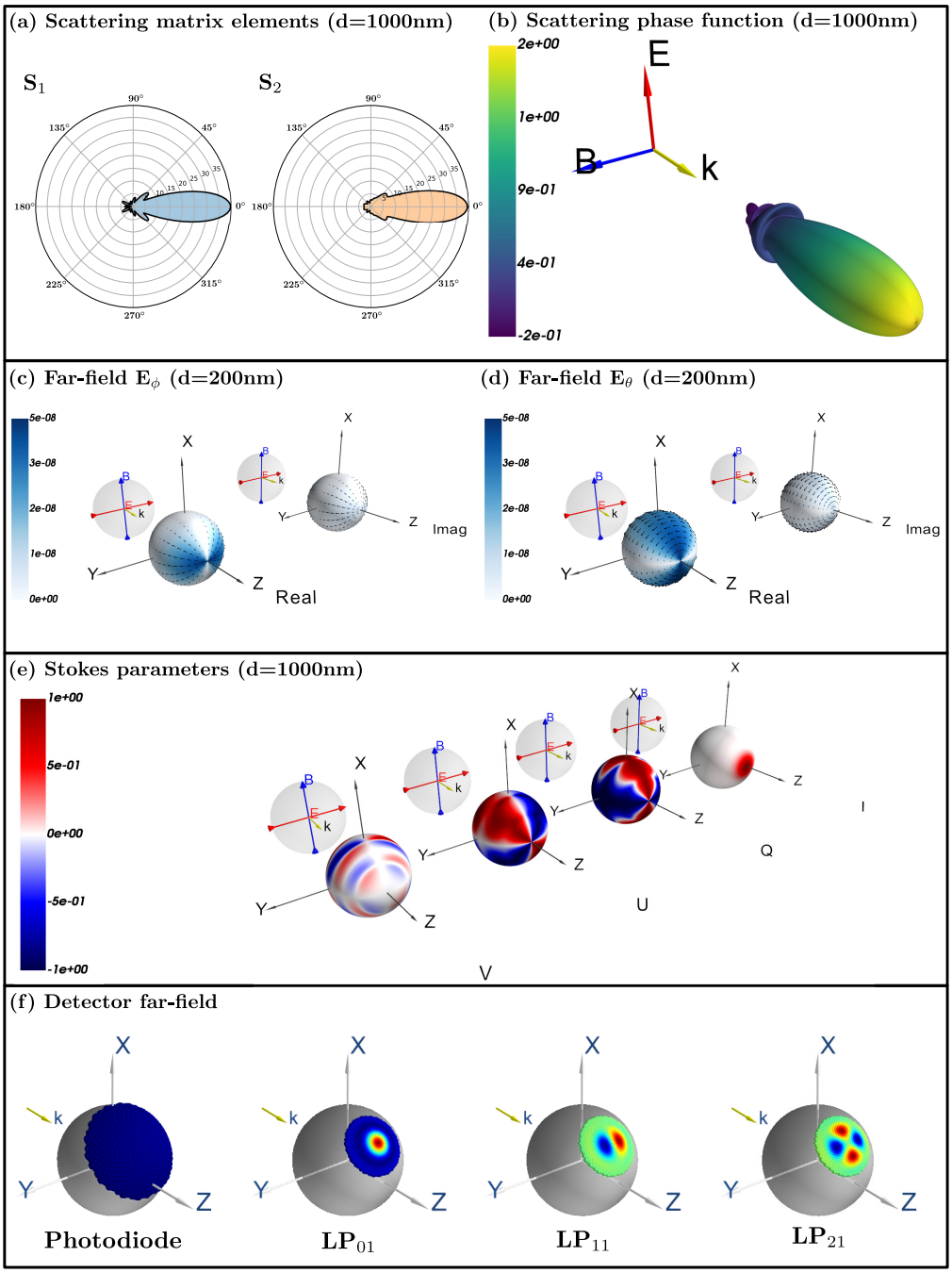



FIGURE 5.5 Images obtained using the PyMieSim library for scattering simulations of various scatterer sizes illuminated with a 1000 nm planewave. (a) The non-null scattering matrix element $S_1$ and $S_2$ ; (b) Scattering phase function ; (c & d) Scattering far-field in the $\hat{\phi}$ and $\hat{\gamma}$ direction, respectively. The real and imaginary parts are depicted in the right and left parts of the sub-figure ; (e) Stokes parameters defining the polarization state using I (intensity), Q (linearly polarized, 0°), U (linearly polarized, 45°) and V (circularly polarized) ; (f) Detector far-field representation for a photodiode, $LP_{01}$, $LP_{11}$ and $LP_{21}$.

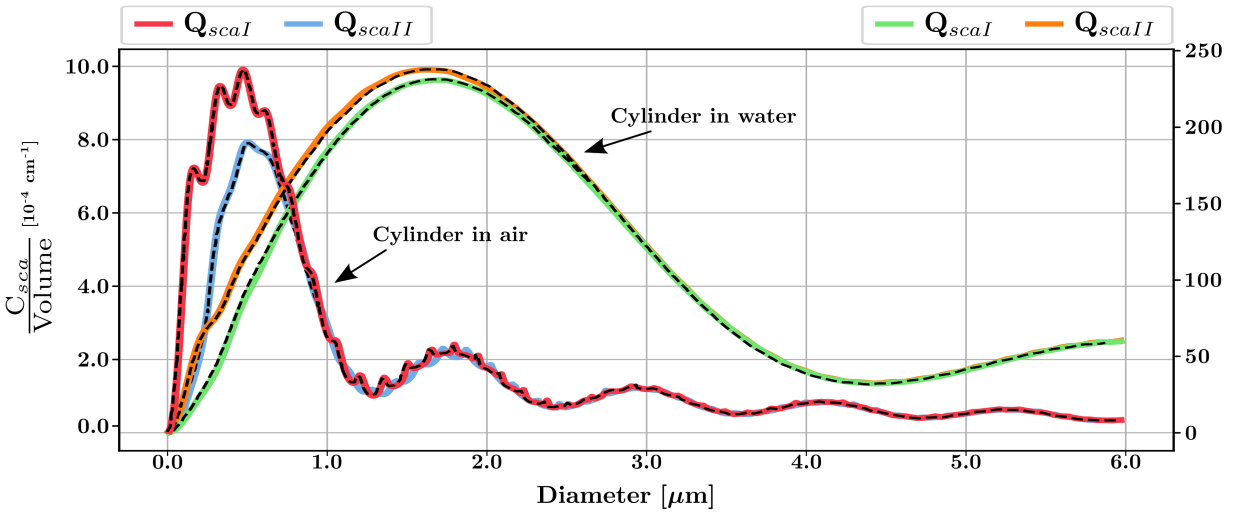



FIGURE 5.6 Simulation of the scattering cross-sections for an infinite cylinder as a function of diameter. The simulation parameters are chosen to replicate the results presented in Fig.(8.7 & 8.8) of [22], which are here represented by the black dashed lines.

defined by a refractive index ranging from 1.33 to 1.6 and diameter ranging from 100 to 500 nm, illuminated with a polarized light source at 405 nm. We first modeled an unoptimized orthogonal detector pair with an NA of 0.15, then let PyMieSim optimize the detectors' angular values ($\phi$ and $\gamma$) and NA (where NA is a free parameter ranging from [0.1 to 0.4]). Figs. 5.7 (a-b) show, for each detector, the coupling power as a function of scatterer size and refractive index. For each detector, the measured coupling power defines an iso-contour, the intersection of which returns the scatterer's size and refractive index. Uncertainty in the detector's measurement broadens the iso-contour into areas bounded by dashed lines in Figs. 5.7 (a-b) and shown as shaded areas in Figs. 5.7 (c-d). Figs. 5.7 (c) maps the intersection of the areas in the unoptimized case. As iso-contours from each detector are not orthogonal, the uncertainty on size and refractive index remains large. PyMieSim was then used to compute a new set of detector's angular locations and NA for which uncertainty would be minimized across all scatterer sizes and refractive indices. For a fixed measurement uncertainty, the best-case scenario occurs when the iso-contours for both detectors are orthogonal, this would mean that the projection of the gradient of the coupling field for each detector equals zero at every point. This was used as the optimization metric, normalized on a scale from zero to one, where zero means that all the iso-contour lines are orthogonal, and one means that they are co-linear. Mathematically, the optimization problem can be written in the following form :

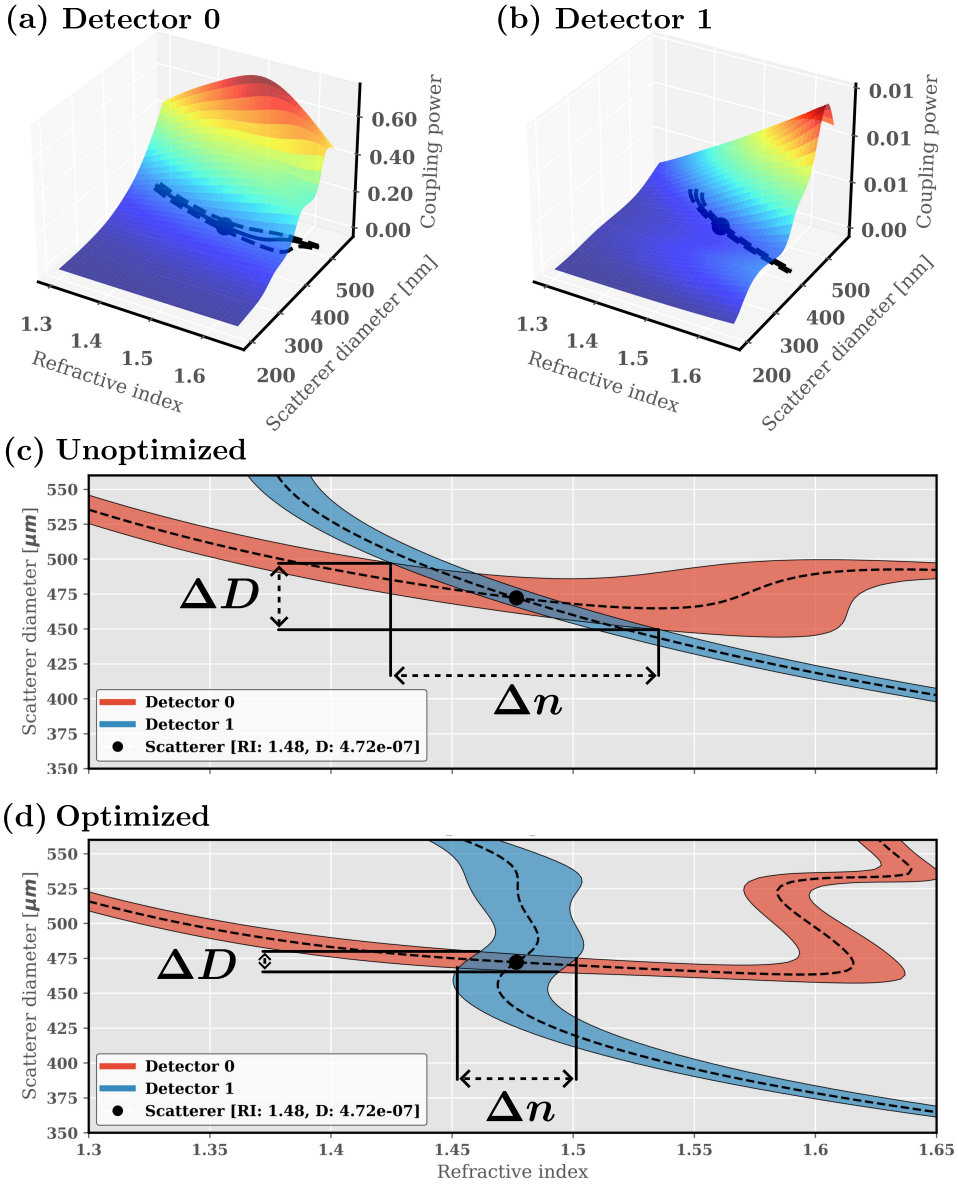



FIGURE 5.7 Parameter space optimization for a flow-cytometry experiment. (a-b) Coupling power of scattered light with a typical flow-cytometry system composed of two orthogonal detectors : (a) detector 0 $\{\phi_0 = 0°, \gamma_0 = 0°, \text{NA} = 0.15\}$ (b) detector 1 $\{\phi_1 = 90°, \gamma_1 = 0°, \text{NA} = 0.15\}$. (c-d) Iso-contour projections of a specific scatterer measurement (RI : 1.48, diameter : 472 nm, dashed lines) with a measurement error of 5% (shaded areas) for the typical (c) and optimized (d) flow-cytometer, where optimized detectors are placed at : detector 0 $\{\phi_0 = 0°, \gamma_0 = 42.3°, \text{NA} = 0.38\}$ and detector 1$\{\phi_1 = 133.2°, \gamma_1 = 68.0°, \text{NA} = 0.38\}$, respectively. $\Delta D$ and $\Delta n$ represent the diameter and refractive index uncertainty, respectively.

$$\min_{\forall s \in \boldsymbol{S}} \left(\vec{\nabla} F_0(s)\right) \cdot \left(\vec{\nabla} F_1(s)\right) \quad , \tag{5.10}$$

where $\boldsymbol{S}$ is the feasible set $\{\phi \in [0, 360], \gamma \in [0, 360], \mathrm{NA} \in [0.1, 0.4]\}$ as defined above, $\mathrm{F}_0$ and $\mathrm{F}_1$ are the coupling fields computed using PyMieSim for each detector. A quick assessment of the metric function establishes that the optimization problem is non-linear and non-convex, and thus we are not guaranteed to find a global minimum. Treating the question as a black-box optimization problem, we consequently choose the Nelder-Mead algorithm [114]. Figure 5.7 (d) presents the iso-contours for the optimized detector's angular values and NA, showing a reduction of uncertainty in size and refractive index. The optimization process gives us a local minimum of 0.27, while using the standard parameters, we obtain a metric value of 0.78. For such a demanding optimization process, PyMieSim's short compute-time and easy-to-handle API were proven very useful for the reasonable computation time and expressiveness of a few lines of code.

### 5.7.2 Coherent Imaging Analysis

Another valuable application of the library concerns coherent or partially coherent imaging. PyMieSim allows simulating coherent detection schemes based on a fiber's LP modes to improve endoscopy methods such as optical coherence tomography (OCT). Recently, the use of several LP modes has been under investigation as a way to acquire additional contrast [39, 82, 125]. PyMieSim allows modeling the source of contrast based on scatterer size and geometries for each LP mode [125]. Fig 5.8 shows an example of the coupling power of a coherent imaging system as a function of the scatterer size and different LP modes. In particular, Fig. 5.8 demonstrates that the coupling behavior does not change for small scatterers (i.e., approaching the Rayleigh regime), however, the coupling power in each mode diverges for larger scatterers, hinting at possible size-based contrast for FM-OCT.

## 5.8 Conclusion

We conclude by briefly comparing PyMieSim to other implementations of Mie theory. Table 5.2 summarizes the features of several Mie codes available online. The table highlights PyMieSim's main aspects : enabling simulation for different types of scatterers, a fast computing core, an easy-to-install package, and an intuitive API. Moreover, PyMieSim addresses shortcomings associated with the other libraries, providing a continuous integration pipeline for an extensive testing process to ensure the library structure's integrity and that the results

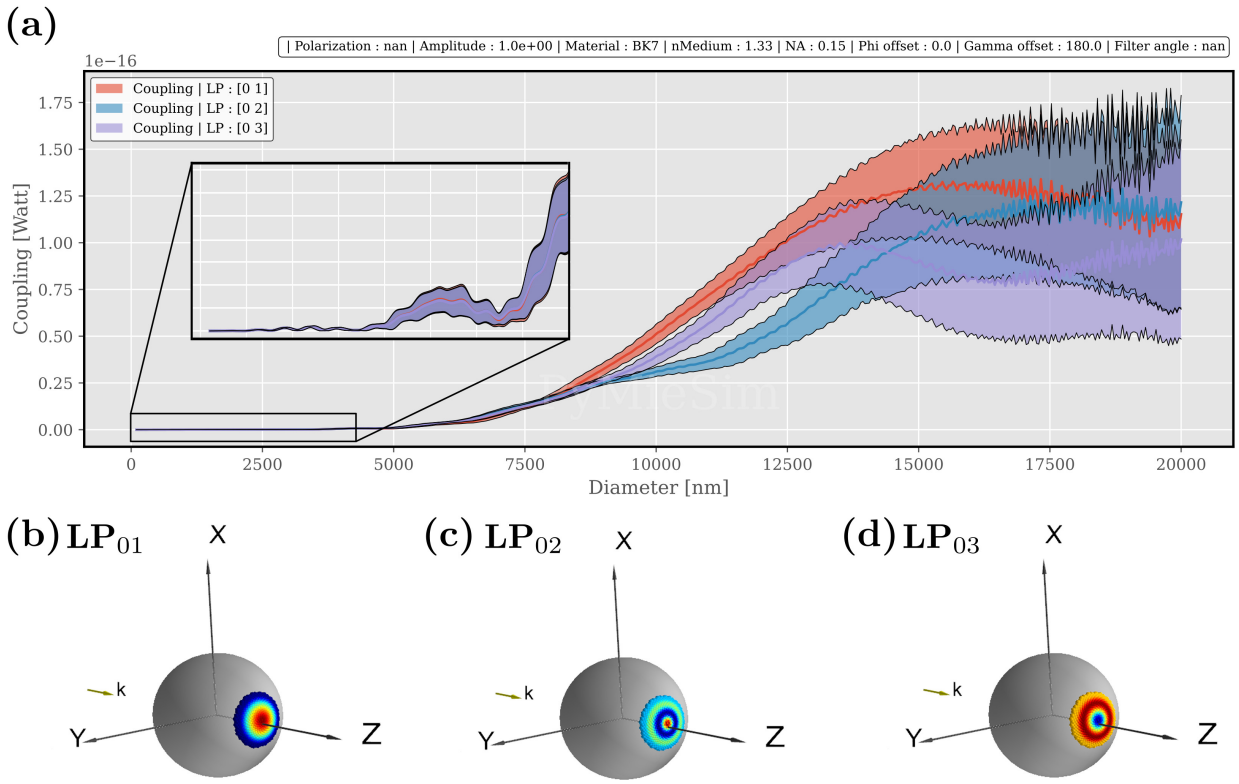



FIGURE 5.8 Simulating FM-OCT imaging at $\lambda_0 = 930nm$ and $\Delta\lambda = 100nm$ with 3 LP modes. (a) Mean (solid lines) and standard deviation (shaded areas) of the power coupled back into each mode as a function of the scatterer diameter for LP01 (b), LP02 (c), and LP03 (d), represented in the far-field. Inset shows the overlap of the three coupling powers in the Rayleigh regime.

produced match the literature. Additionally, the library provides complete online documentation and a platform with tens of examples featuring the reproduction of already published results.

The PyMieSim package is still under active development and has been designed to be readily upgraded. The library also makes use of external tools such as Travis [13] for continuous integration and Docker [109] for the compilation of the source code for each OS. There are various incremental additions and features that are being designed for near-future deployments, namely : GLMT framework, GPU computation, and graphical user interface (GUI). The GLMT framework is an extension of the LMT for structured illumination sources, thus allowing the user to define specific light sources such as a Gaussian beam [130], Bessel beam [2] or fiber optic LP modes. While many simulation projects exist for LMT simulations, only a few include GLMT. The framework can also be used to simulate the interaction with scatterers breaking the symmetries, as it was demonstrated for arbitrarily oriented spheroids [167]. While the necessary computation differs from the LMT framework, using the existing PyMieSim platform makes such a feature easier to implement. A similar approach could also be used to compute the near-field components of scattering events, allowing for multi-scatterer interaction and thus widening the range of applications of the library.

The ability to create experiment setups with ranging attributes for the scattering event is one of the main appeals of PyMieSim. Moreover, its implementation has been parallelized to make the most of the multiple cores that recent CPU architecture offers. Due to its highly independent implementation, the algorithm for such computation could be passed to GPU for an even more reduced runtime.

Finally, the aim of the package is to be easy to install and use. While the interpreted Python language allows using easy to handle platforms such as Jupyter notebook or Google Colab, the coding part might still be a barrier for some users. As such, developing a graphical interface can help overcome this difficulty. This is why we plan to develop a server-based application that will be accessible through a web browser.

**Funding**

Fonds de Recherche du Québec - Nature et technologies (FRQNT) #304141 (MPDSH), Natural Sciences and Engineering Research Council (NSERC) of Canada grants #RGPIN-2018-06151 (CB), #RGPIN-06404-2016 (NG).

TABLE 5.2 Features of open source LMT packages. Features were deduced from an in-depth analysis of each project.

| | Features \ Libraries | PyMieSim | PyMieScatt | MieLab | MiePython | BimSim |
|---|---|---|---|---|---|---|
| Scatterer type | Homogeneous sphere | ✓ | ✓ | ✓ | ✓ | ✓ |
| | 2-layer sphere | ✓ | ✓ | ✓ | | |
| | N-layer sphere | | | ✓ | | |
| | Infinite cylinder | ✓ | | | | |
| Performance | Compiled core | ✓ | | | ✓ | ✓ |
| | CPU Parallel computing | ✓ | | | | |
| | GPU computing | | | | | ✓ |
| Ease of use | Python Interface | ✓ | ✓ | ✓ | ✓ | |
| | Documentation | ✓ | ✓ | ✓ | ✓ | |
| | Examples | ✓ | ✓ | | | |
| | Package manager | ✓ | ✓ | | ✓ | |
| | Multi-platform | ✓ | ✓ | | ✓ | ✓ |
| | Online platform | ✓ | | | ✓ | |
| | Data visualization tools | ✓ | | | | |
| | Ranging parameters | ✓ | | | | |
| | Graphic interface | | | ✓ | | |
| Extra | Continuous Integration | ✓ | | | | |
| | Automatic testing | ✓ | | | | |
| | Detector emulation | ✓ | | | | |

## Acknowledgements

We thank Pierre-Alexandre Aubé for his precious help with the writing of the PyMieSim package. Portions of this work were presented at SPIE Photonics West's Symposium on *Optical Interactions with Tissues and Cells XXXIII; and Advanced Photonics in Urology* in 2022 (PC1195802) [123]. The presentation focused on the application programming interface and the usability of the package, while this manuscript delves into the equations behind the package, validates its output against other packages, demonstrates improvement in the computation time, and demonstrates the novel and unique features of PyMieSim through two use-cases of practical interest to the community.

## Disclosures

The authors declare no conflicts of interest.

## Data Availability

The source code for PyMieSim is available on GitHub [126]. The raw data used in the article is available from the authors upon reasonable request.

# CHAPTER 6 ARTICLE 3 : ALL-FIBER FEW-MODE OPTICAL COHERENCE TOMOGRAPHY USING A MODALLY-SPECIFIC PHOTONIC LANTERN

This chapter was adapted from : **Martin Poinsinet de Sivry-Houle** et al. "All-fiber few-mode optical coherence tomography using a modally-specific photonic lantern." Biomedical Optics Express 12 9 (2021) : 5704-5719, submitted on April 26, 2021.

## 6.1 Author Contribution

The article on which this chapter is based was submitted to Biomedical Optics Express journal, published on 19/09/2021. Martin Poinsinet de Sivry-Houle is the first author of the publication and contributed to 90% of the work. Simon Beaudoin, Simon Brais-Brunet, Mathieu Dehaes, and Caroline Boudoux contributed to the scientific discussion. Nicolas Godbout and Caroline Boudoux were senior investigators and assisted in the manuscript revision.

## 6.2 Chapter Context

This chapter presents a novel study in the field of biomedical imaging, featuring the first-ever application of a modally-specific photonic lantern (MSPL). The study's primary objective was to investigate and validate the technology's potential to enhance sensing and contrast in OCT, a key technique in biomedical imaging. The exploration was grounded on a model, which was then corroborated through experimental work. The research highlights the complex contrast mechanisms involved when utilizing this avant-garde technology in OCT. By employing the MSPL in conjunction of OCT, the study sets a precedent that might lead to advancements in biomedical imaging, refining its capabilities and accuracy. This paper thus provides an initial look into this promising and relatively unexplored territory.

## Abstract

OCT was recently performed using a few-mode (FM) fiber to increase contrast or improve resolution using a sequential time-domain demultiplexing scheme, isolating the different interferometric signals of the mode-coupled backscattered light. Here, we present an all-fiber FM-OCT system based on a parallel modal demultiplexing scheme exploiting a novel MSPL. The MSPL allows for maximal fringe visibility for each fiber propagation mode in an all-fiber

assembly, which provides the robustness required for clinical applications. The custom-built MSPL was designed for OCT at 930 nm and is wavelength-independent over the broad OCT spectrum. We further present a comprehensive coupling model for the interpretation of FM-OCT images using the first two propagation modes of a few-mode fiber, validate its predictions, and demonstrate the technique using *in vitro* microbead phantoms and *ex vivo* biological samples.

## 6.3 Introduction

Optical coherence tomography (OCT) is an imaging technique that relies on low-coherence interferometry to measure depth-resolved reflectance profiles of tissues [68]. By illuminating a sample with a low-coherence light source, OCT systems measure the cross-correlation signal with a reference arm to discriminate backscattering light originating from different tissue depths. This discrimination, which is called coherence gating, allows obtaining a three-dimensional reconstruction of the sample. Similar to most microscopy techniques, OCT comprises an illumination and a collection scheme. Typically, OCT systems use a unique SMF for both illumination and collection, thereby rejecting most backscattered light along with information it carries. Several optical techniques — including elastic light scattering spectroscopy [49] and hybrid confocal imaging [70] — exploit this wealth of information as a contrast mechanism. However, these techniques are constrained to probing thin samples to ensure a single-scattering regime, as multiple-scattering would randomize the phase function. By comparison, the intrinsic coherence gating of OCT can be used to assess scattering in a thin, virtual layer located within a macroscopic sample. Therefore, combining OCT imaging with a contrast mechanism based on the scattering phase function (SPF) would allow exploiting valuable information including in-depth intrinsic properties of the biological tissue. Previous studies have shown that this strategy could be achieved using the first few propagation modes of a FMF provided they can be efficiently isolated and independently measured [38, 40]. In particular, these studies suggest that contrast channels based on scattering directionality can be obtained using higher-order propagation modes. Amongst other things, they demonstrated the use of higher-order modes to highlight neuritic plaques associated with Alzheimer's disease in *ex vivo* brain samples. The optical system previously described [38] exploits modal dispersion of an FMF [144] to achieve time-windowing demultiplexing of the interferometric channels. However, the complex scheme proposed by the authors presents technical limitations on maximal fringe visibility. In particular, as the scheme requires free-space misalignment of the optical beam to allow for interference between orthogonal modes, the acquisition of additional modes requires increasing the offset at the expense of the signal-to-noise ratio.

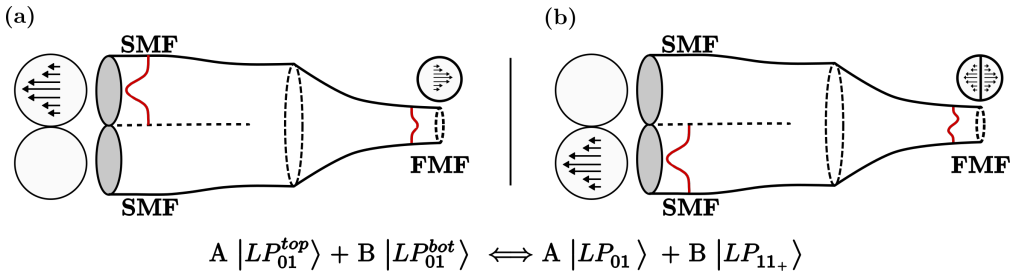



FIGURE 6.1 Schematic of a modally-specific photonic lantern. (a) The top SMF LP mode, $|LP_{01}^{top}\rangle$, maps the $\mathrm{LP}_{01}$ mode of an FMF. (b) The bottom SMF mode, $|LP_{01}^{bot}\rangle$, maps the $\mathrm{LP}_{11+}$ mode of the FMF. Mapping from the FMF to the SMF is reciprocal. The equation shows the mapping relation with $A$ and $B$ being amplitude coefficients, and the + sign (as opposed to $\times$) represents one of the two orthogonal $\mathrm{LP}_{11}$ mode (the two modes ($\mathrm{LP}_{11+}$, $\mathrm{LP}_{11_\times}$) are similarly structured but for a $\pi/2$ rotation).

To simplify the imaging system and overcome these limitations, we present an all-fiber approach based on a custom-made MSPL. Photonic lanterns are $N$-by-one fiber optic components mapping the propagation modes of a bundle of $N$ SMFs to the modes of a multimode structure [16]. MSPLs are a sub-category of photonic lanterns that feature a one-to-one mapping between individual SMFs and LP modes of a multimode fiber. Reciprocally, MSPLs allow demultiplexing the modal content of light propagating in a multimode fiber. MSPLs are intrinsically wavelength independent. This signifies that the modal mapping does not depend on the excitation wavelength, a trait that makes them particularly interesting for broadband imaging techniques such as OCT. Figure 6.1 presents a schematic describing the principle of a MSPL. In particular, Fig. 6.1 (a) shows the excitation in the upper SMF mapping to the fundamental mode of an FMF, while in Fig. 6.1 (b), the lower SMF maps to a higher order mode of the FMF. In this paper, we present a few-mode OCT imaging system based on a custom-designed MSPL, provide a comprehensive model for the mode-dependent coupling mechanism of the backscattered light onto the FMF, and experimentally validate numerical predictions through responses from optical phantoms and *ex vivo* biological samples.

## 6.4 Contrast mechanism

Here, we propose a model for coupling backscattered light with the modes of the FMF. We begin with a general model that we then apply to two specific cases : a single spherical scatterer and a continuous distribution of refractive indices representing biological tissues.

### 6.4.1 Coupling model

Illumination is carried out with a particular mode of an MSPL through imaging optics and results in its projection with magnification onto the focal plane and within the sample. Conversely, collecting light with the same optical scheme leads to the projection of backscattered light from the sample onto the fiber tip. As such, backscattered light couples with each of the modes of the multimode end of the MSPL with different efficiencies. Since the MSPL selectively demultiplexes certain modes, we can directly measure such efficiencies. The rest of the higher-order modes, which are not demultiplexed, couple into the cladding modes of the fiber and are subsequently lost in the first few centimeters of propagation. With a similar approach used in previous studies [32, 43, 77], we define the modal coupling efficiency $\boldsymbol{\eta}_{l,m}$ of the incident light field onto LP modes as

$$\boldsymbol{\eta_{l,m}} = |\langle\psi|\phi_{l,m}\rangle|^2 = \underbrace{\left|\iint_s \psi(x,y)^*\phi_{l,m}(x,y)dxdy\right|^2}_{DSR} \tag{6.1}$$

$$= \underbrace{\left|\iint_\Omega \tilde{\psi}(\xi,\nu)^*\tilde{\phi}_{l,m}(\xi,\nu)d\xi d\nu\right|^2}_{FSR} = \left|\left\langle\tilde{\psi}\middle|\tilde{\phi}_{l,m}\right\rangle\right|^2, \tag{6.2}$$

where $\langle\psi|$ represents the incident light field state arriving onto the FMF while $|\phi_{l,m}\rangle$ represents the FMF mode state, with $l$ and $m$ being indices associated with LP modes. The second line of the equation is derived from the first using Plancherel's theorem, also called the Parseval-Plancherel identity. Depending on the situation, one can choose to use the direct-space representation (DSR) or the Fourier-space representation (FSR). Here, $\psi(x,y)$ and $\phi(x,y)$ are the direct-space fields, while $\tilde{\psi}(\xi,\nu)$ and $\tilde{\phi}(\xi,\nu)$ are the spatial Fourier-space fields. The integral index $s$ represents the plane in which the near-field LP modes exist, and its Fourier counterpart $\Omega$ represents the solid angle subtended by the NA of the imaging lens. This definition does not account for vector fields and thus, its exactness relies on the scalar approximation, which is usually adequate for most low NA imaging systems [143]. From Eq. (6.1), we observe that each mode added to the system leads to complementary information regarding the SPF as each mode carries an orthogonal projection of the SPF. More specifically, each collected mode allows to sample spatial frequency content of the incident light field. Using this additional information and adequate modeling, we can simultaneously infer certain intrinsic properties of the sample and generate more contrast channels. While the MSPL is wavelength-independent, the modal coupling efficiencies are wavelength-dependent, which may provide an additional way to probe biological samples in a manner similar to

light-scattering spectroscopy [7]. To quantitatively estimate spatial frequencies contained in the backscattered wavefront for a given wavelength, we use the SPF that describes the polar distribution of the far-field scattering intensity [140]. For a single spherical scatterer, closed-form solutions arise from Mie scattering theory [21, 71], which is particularly useful to validate theoretical predictions. For a distribution of scatterers, empirical phase functions such as the Henyey-Greenstein (HG) distribution [63] are widely used for their approximate representation of tissue scattering and simplified mathematical forms.

### Mie scattering coupling

To assess the optical response of the system to a sample and validate the proposed model, we investigated the coupling mechanism for a single scatterer. For spherical dielectrics, Mie scattering theory predicts that the scattering efficiency and phase function depend on the size parameter $\alpha$ defined as

$$\alpha = \pi d/\lambda, \tag{6.3}$$

where $d$ is the diameter of the spherical scatterer and $\lambda$ is the wavelength of the impinging field. The SPF is also dependent on the polarization state of the incident light field, but for the sake of conciseness, we only consider linearly polarized illumination. Using a home-made Python package based on previous studies [22, 149] we can compute the parameters $S_{11}(\theta)$ and $S_{22}(\theta)$ which define the far-field phase function for differently-sized dielectric spheres using

$$\begin{bmatrix} E_{\parallel}^{s} \\ E_{\perp}^{s} \end{bmatrix} = \frac{e^{-ikr}}{ikr} \begin{bmatrix} S_{11}(\theta) & S_{12}(\theta) \\ S_{21}(\theta) & S_{22}(\theta) \end{bmatrix} \begin{bmatrix} E_{\parallel}^{0} \\ E_{\perp}^{0} \end{bmatrix}, \tag{6.4}$$

where $E^s$ denotes the scattered field, while $E^0$ is the incident field. $E_{\parallel}$ and $E_{\perp}$ are the parallel and perpendicular fields (i.e., two polarization states) measured at a point of distance $r$ from the scatterer, respectively. For spherical scatterers, there is, in theory, no coupling between polarization states and $S_{12} = S_{21} = 0$. We did not take into account the structure of the illuminating field and assumed it to be uniform. Using Eq. 6.4, we can simulate the full far-field amplitudes profiles (over $4\pi$ steradians) for different scatterer sizes, as presented in Fig. 6.2. In Fig. 6.2 (a-c), we present the overlap of the far-field scattering distribution

of $LP_{01}$ and $LP_{11+}$ in spatial frequency representation. We notice that the overlap strongly depends on the scatterer size and thus, from Eq. 6.1, we expect it to affect the modal coupling efficiency. Using the FSR part of Eq. (6.1), we compute the modal coupling efficiency for a perfectly centered scatterer relative to the collecting mode by computing the overlap integral. In practice, however, it is unlikely that the scattered field will be perfectly axially aligned with the fiber mode field. To account for non-centered scatterers, lateral offsets $\delta_x$ and $\delta_y$ in the $x$ and $y$ directions, respectively, were added to Eq. 6.1. Using the convolution theorem, the overlap integral can be computed in Fourier-space as

$$\begin{aligned}\boldsymbol{\eta}_{l,m}(\delta_x,\delta_y) = |\langle\psi(x+\delta_x,y+\delta_y)|\phi_{l,m}(x,y)\rangle|^2 &= \Big|\underbrace{[\psi\otimes\phi_{l,m}](\delta_x,\delta_y)}_{\textbf{convolution}}\Big|^2 \\ &= \Big|\mathscr{F}^{-1}\Big\{\tilde{\psi}(\xi,\nu)\,\tilde{\phi}_{l,m}(\xi,\nu)\Big\}(\delta_x,\delta_y)\Big|^2. \quad (6.5)\end{aligned}$$

Equation (6.5) predicts the modal coupling efficiency of the backscattered light as a function of the lateral offset :

Hence, by allowing the imaging system to oversample, we probe each of those offsets to retrieve the scatterer footprint also presented in Fig. 6.2 (a-c). The point spread function (PSF) of such a system is, by definition, the footprint of a sufficiently small scatterer. We therefore define the respective PSF for $LP_{01}$ and $LP_{11+}$ mode as the footprint produced by the 500 nm scatterers shown in Fig. 6.2 (a). We also define the mean modal coupling efficiency as the integral over the lateral offset space

$$\tilde{\boldsymbol{\eta}}_{l,m} = \Big\langle \eta_{l,m}(\delta_x,\,\delta_y)\Big\rangle = \Big\langle\,\Big|\,\tilde{\psi}(\xi,\nu)\,.\,\tilde{\phi}_{l,m}(\xi,\nu)\Big|^2\Big\rangle_{\Omega}, \quad (6.6)$$

where $\langle\,.\,\rangle$ represents the average value on the solid angle $\Omega$ subtended by the NA of the imaging system. In the modal footprints presented in Fig. 6.2, some of them appear brighter (or darker) denoting a larger (or lower) mean coupling. The variations of the footprint and mean modal coupling efficiencies as a function of the scatterer diameter shows that the spatially oversampled image carries information in a two-fold manner. In particular, the couple $(\boldsymbol{\eta}_{l,m}(\delta_x,\delta_y),\tilde{\boldsymbol{\eta}}_{l,m})$ forms the modal signature of the scatterer. With adequate modeling, the analysis of such signature would theoretically allow inferring the geometry of the scatterer, which is a piece of information well below the resolution limit of a typical OCT system. The oversampled signature also depicts two interesting features. Firstly, the anti-symmetric

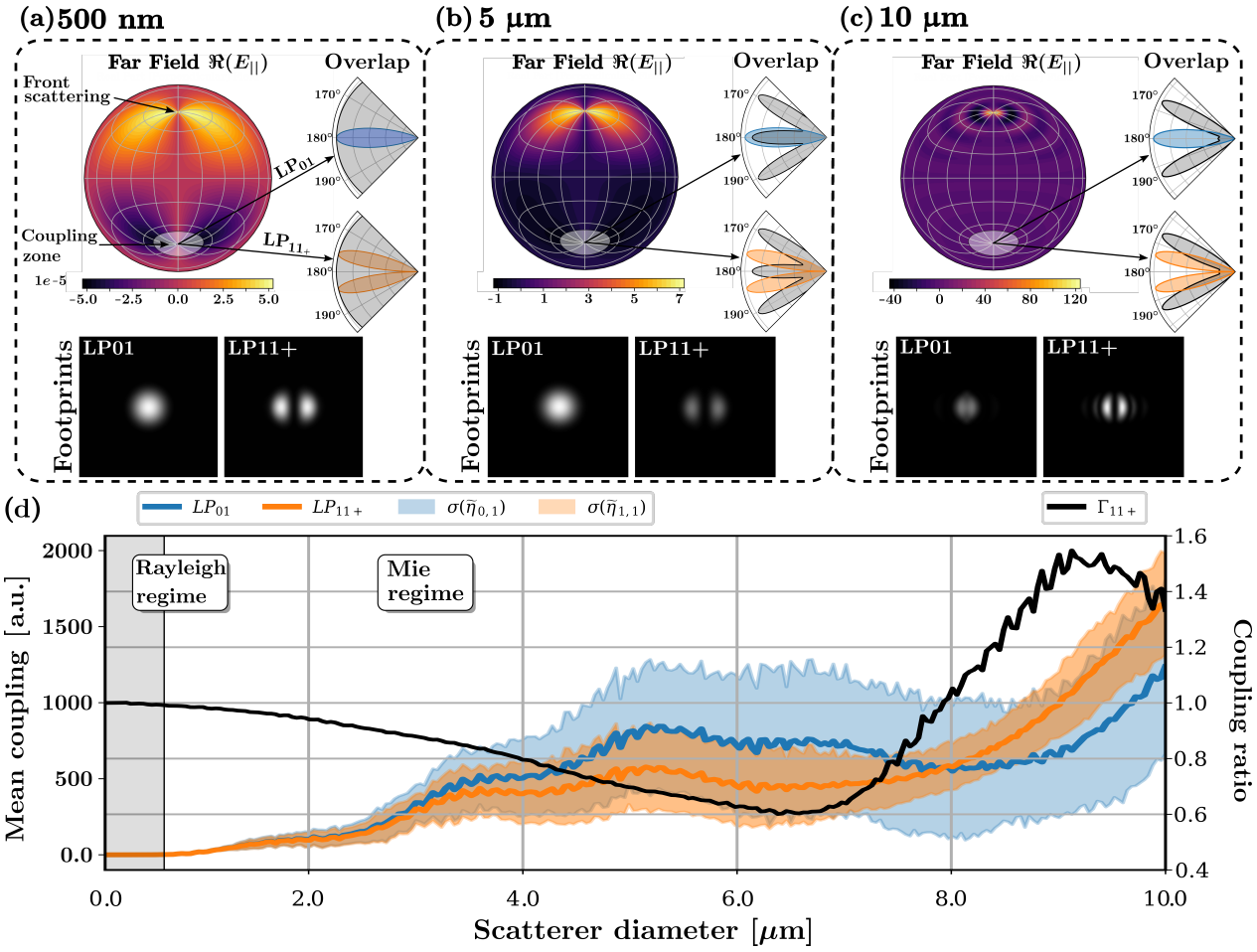



FIGURE 6.2 (a, b & c) Lambert projection of simulated parallel far-field, overlap with LP modes ($LP_{01}$ : blue, $LP_{11+}$ : orange) and simulated modal footprints for scatterers of diameter 500 nm, 5 µm and 10 µm. (d) Mean modal coupling for $LP_{01}$ (blue) and $LP_{11+}$ (orange), and their ratio (black), averaged for the wavelength range of OCT ($\lambda_0 = 930$ nm, $\Delta\lambda = 50$ nm); The x-axis is divided into two sections representing the two scattering regimes, Rayleigh ($\alpha < 1$) and Mie ($\alpha > 1$).

$LP_{11+}$ mode does not couple near a null offset (i.e. when the scatterer is axially aligned with the fiber mode). This behavior is expected as the phase function for a perfectly spherical scatterer is necessarily symmetric under inversion. Thus, if the scatterer is centered with the collecting mode (null offset), the overlap integral with $LP_{11+}$ (Eq. (6.1)) should always be zero. Secondly, from Fig. 6.2 (d) we notice that the mean modal coupling efficiencies strongly depend on the scatterer size. However, based on Mie theory, the SPF stabilizes when approaching the Rayleigh regime defined by the size parameter $\alpha$ being inferior to unity. This indicates that modal coupling efficiencies remain relatively constant for small scatterers in comparison to the wavelength. This characteristic can be visualized in Fig. 6.2 (d) presenting

the mean modal coupling efficiencies as a function of the scatterer diameter. The solid lines represent the mean coupling averaged over the full OCT spectrum while the color shading represents the standard deviation for that same spectrum. Figure 6.2 (d) also includes the ratio of the modal coupling $\Gamma_{1,1+}$ defined as

$$\Gamma_{11+} = \frac{\tilde{\eta}_{1,1+}}{\tilde{\eta}_{0,1}}. \tag{6.7}$$

We notice that for particles under 2 µm (*i.e.* $\alpha \leq 6.75$ at $\lambda = 930$ nm) the ratio $\mathrm{LP}_{11+}$ over $\mathrm{LP}_{01}$ settles to approximately 1.0 ($\Gamma_{11+} \approx 1.0$). We also remark that the modal coupling is wavelength-dependent. This feature is represented as the shaded color ($\sigma(\tilde{\boldsymbol{\eta}}_{l,m})$) in Fig. 6.2 (d). While this dependency is negligible for scatterers with a diameter under 2 µm, it grows significantly (and almost monotonically) for diameter over that value. Thus, we define the threshold size parameter separating the two regimes as $\alpha = 6.75$. For large-bandwidth imaging techniques such as OCT, this feature can be of great interest if the response of each wavelength can be efficiently isolated, as demonstrated in [89]. Our simulation neglected two important effects : multi-particle scattering within an optical plane and defocusing. Here, while coherence gating ensures optical sectioning, it does not prevent scatterers to be affected by adjacent particles. Previous work [154] has shown how the SPF of a two-body system varies as a function of the inter-particle spacing. The results demonstrate that the variation of the SPF mainly occurs for large scattering angles, and the SPF structure does not change significantly for low angles. As most of OCT imaging system have low NA's, we posit that the presence of multiple scatterers does not affect the structure of the scattered fields, although it would enhance the scattering efficiencies. On the other hand, while the effect of optical defocusing can be emulated by modifying the acceptance cone of the far-field representation of the LP mode, it would also compromise the approximation of the incident plane wave. As such, a more extensive model using the generalized Lorenz-Mie theory would be required to take defocusing into account.

### 6.4.2 Coupling mechanism in a biological tissue

In the same way as for Mie scattering, the coupling mechanism for LP modes in biological tissue is directly dependent on the SPF. However, for biological tissues, modeling an accurate phase function for a given sample can prove challenging. The Henyey-Greenstein SPF [63] is widely used, as its analytic form simplifies model fitting. It represents an averaged distribution of multi-event scattered photon paths. However, because the photon mean

free path in biological samples is an order of magnitude larger than the OCT coherence gating (*i.e.* $\leq 10\,\mu m$), most of the photons collected are issued from a single scattering event. For instance, the photon mean free path in human skin is about $350\,\mu m$ for illumination at 755 nm [41]. The use of a more sophisticated model is thus needed. A more extensive way to describe a random and continuous medium is to use the refractive index (RI) correlation function $C_n(\rho)$. This function statistically characterizes the structural distribution of RI in the sample. To model $C_n(\rho)$, the Whittle-Matérn (W-M) functional family can be used :

$$C_n(\rho) = N_c\, 2^{(5-D)/2}\Big(\frac{\rho}{l_c}\Big)^{(D-3)/2} K_{(D-3)/2}\Big(\frac{\rho}{l_c}\Big), \tag{6.8}$$

where $\rho$ is the radial distance, $N_c$ a scaling factor, $D$ a deterministic factor, $l_c$ the correlation length, and $K$ the Bessel function of the second kind. With this definition for the correlation function and using the first Born approximation [9], one can derive the analytical solution for single-event scattering cross-section per unit of volume $\sigma(\theta, \phi)$ [141, 168] such that

$$\sigma(\theta,\phi) = 2\,N_c\,k^4\,l_c^3\,\Gamma(D/2)\frac{(1-\sin^2(\theta)\cos^2(\phi))}{\sqrt{\pi}(1+[2kl_c\sin(\theta/2)]^2)^{D/2}}, \tag{6.9}$$

where $\Gamma$ is the gamma function, $k$ is the wavenumber and $(1-\sin^2(\theta)\cos^2(\phi))$ is the dipole factor for a linearly polarized incident field at the angle $\phi = 0$. It is to be noted that the Born approximation is valid under the condition $N_c\,k\,l_c \ll 1$ [9]. The latter condition defines what

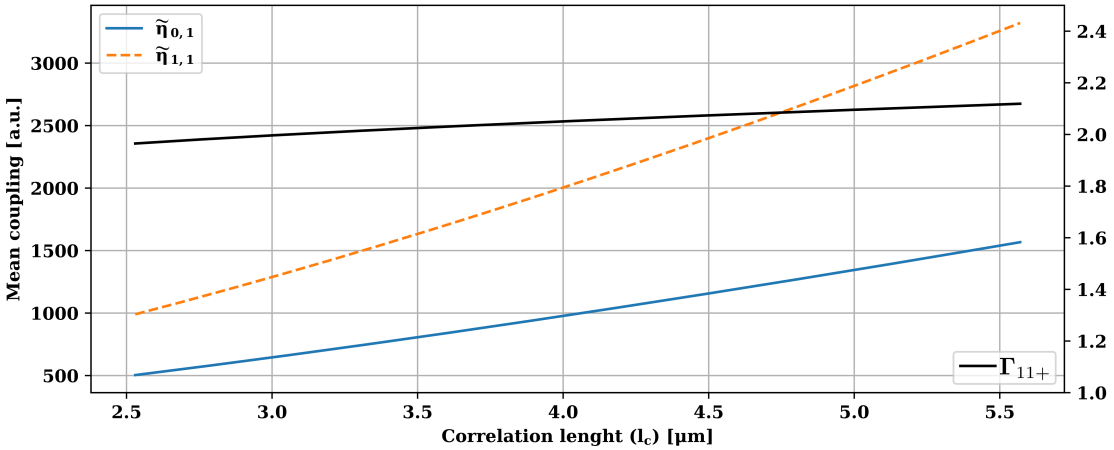



FIGURE 6.3 Theoretical prediction of modal mean coupling in liver sample $\tilde{\boldsymbol{\eta}}_{l,m}$ (blue & orange) and their ratio $\boldsymbol{\Gamma_{11+}}$ (black).

we refer to as low-coherencesamples. Using this model and data provided in [168], we can compute the mean modal coupling in the same way as it was defined in the previous section. Doing so, we observed that for all three parameters $(N_c, l_c, D)$, the mean modal coupling varies in a similar fashion for both modes. For instance, the refractive index correlation length ($l_c$) of a rat liver sample is expected to vary from 2.53 to 5.57 µm [168]. Figure 6.3 presents the theoretical mean coupling for $\mathrm{LP}_{01}$ and $\mathrm{LP}_{11+}$ as a function of $l_c$ for such a sample. Figure 6.3 highlights that the mean coupling $\tilde{\boldsymbol{\eta}}_{l,m}$ increases almost linearly with $\mathrm{l}_c$ for both modes, and hence the ratio ($\mathbf{\Gamma_{11+}}$) does not change significantly. This behavior is expected as such samples scramble the impinging light field structure, resulting in a loss of spatial coherence. Thus, for samples described per $C_n(\rho)$ the SPF tend to be much smoother than for a single spherical scatterer. As such, we refer to them as low-coherencesamples. This result is in contrast with the single scatterer model, which predicts large variation of $\mathbf{\Gamma_{11+}}$ as a function of the scatterers diameter. Moreover, a low-coherencesample should not present a characteristic footprint (as opposed to single scatterers) as each point contributes equally to the output image. Another effect of few-mode coherent imaging is the characteristic speckle pattern associated with each mode. The effect of the illumination pattern on the speckle statistics has been established in [47,65]. More precisely, the speckle autocorrelation function $R_I(\Delta x, \Delta y)$ is linked to the illumination structure as

$$R_I(\Delta x, \Delta y) = \langle I \rangle^2 \left[ 1 + \left| \frac{\iint |P(\xi,\eta)|^2 \exp\left[ i\frac{k}{z}(\xi\Delta x + \eta\Delta y) \right] d\xi d\eta}{\iint |P(\xi,\eta)|^2 d\xi d\eta} \right|^2 \right], \tag{6.10}$$

where $I$ is the intensity of the incident field, $\xi$ and $\eta$ are the transverse coordinates at the objective lens plane, $\Delta x$ and $\Delta y$ are the transverse coordinates at the image plane, $|P(\xi,\eta)|^2$ is the intensity distribution of the field impinging on the sample, $k$ is the wavenumber, and $z$ is the distance between the lens plane and the image plane. Eq. 6.10 highlights the dependence of speckle pattern on the illumination structure $P(\xi,\eta)$. This model is valid for structured illumination and uniform collection. By using the reciprocity principle of optical scattering processes in turbid media, the model is also valid for uniform illumination and structured collection, as discussed previously [81, 128]. To some extent, we can consider the $\mathrm{LP}_{01}$ illumination as uniform and, hence, we can compute the correlation function for $\mathrm{LP}_{01}$ and $\mathrm{LP}_{11+}$ imaging. Additionally, it is possible to retrieve a good estimation of the PSF from the speckle pattern on the sample [108]. Previous works have demonstrated the use of an FMF to eliminate spatial coherence of a laser beam in order to even out the speckle pattern [6] or to distribute light intensity around the focal point [79]. However, such multiplexing techniques

offer limited control on the modal content in the FMF and are restricted to illuminating or collecting light with a circularly symmetric pattern. This last limitation prohibits evaluating direction sensitive properties. As the MSPL allows precise control over each mode, the asymmetric nature of the $LP_{11+}$ speckle pattern could be used to infer dynamic properties of tissues, such as the direction of flows. To summarize the theoretical predictions, we have on one hand the single scatterer model which predicts modal coupling efficiency that strongly depends on the scatterer size. On the other hand, we have the low-coherencesample model, which predicts no significant variation on the modal coupling efficiency but a strong variation in the speckle pattern. These theoretical predictions translate to OCT imaging in the following way. We anticipate that low-coherence samples result in OCT images of similar intensity regardless of the imaging mode. However, for samples containing larger scatterers, we expect a size-dependent differential contrast between OCT images produced with each orthogonal mode. This contrast can be used to highlight large scatterers inside a low-coherencesample, as previously reported with neuritic plaque [38]. However, to get a better understanding on the contrast at the frontier, it would be possible to use solution such as finite-difference time-domain (FDTD) [36, 134], pseudo-spectral time-domain (PSTD) [100] or even polarization tracking Monte-Carlo simulation [26, 164].

## 6.5 Materials and methods

### 6.5.1 Photonic lantern design

Photonic lanterns achieve mode-mapping through an adiabatic transition between the two ends of the component. A truly adiabatic transition also makes the process lossless. The design of the custom-made MSPL is based on previous work [51] from our group. An extensive description of the fabrication process was also previously reported [12]. The current embodiment uses two different custom-pulled double-clad fibers to produce a strongly asymmetric index profile to build an ultra-short (4 mm long) modally-specific 2-by-1 photonic lantern (see Fig. 6.1 (a)). The short length of the component is a desired feature for imaging as it makes it more robust and resistant to vibrations. The radius of the multimode output of the MSPL is 5.0 µm with a theoretical $LP_{01}$ mode field radius of 4.0 µm and an $LP_{11+}$ mode radius of 4.4 µm.

### 6.5.2 Optical system

The MSPL is incorporated into an imaging setup (Fig. 6.4) consisting of two commercially available spectral-domain (SD) OCT systems (Callisto, Thorlabs, Newton, USA) centered

at 930 nm. From the second OCT system, only the spectrometer and acquisition electronics were used for detection – only one OCT source is required for this setup, as highlighted in Fig. 6.4. Its bandwidth of approximately 80 nm provides an axial resolution of 7 µm in the air. This particular system was selected as its wavelength range is within our MSPL operating range. The MSPL features very-low loss over the entire OCT spectrum (under 0.5dB). The FM-OCT system was designed with off-the-shelf optical components including optical fibers (780HP, Thorlabs), achromatic fiber couplers, polarization controllers, B-coated collimators, and achromatic lenses. The objective lens has a 60 mm focal length. In this configuration, illumination is carried out exclusively with $LP_{01}$ . The imaging head is expected to produce a spot-size of approximately 30 µm at the focal point. The optical setup also includes two individual reference arms designed to compensate for dispersion and to precisely adjust the zero-delay position for each propagation mode. These adjustments are controlled with optical lengths $R_1$, $R'_1$, $R_2$ and $R'_2$. The reference arms are adjusted to set an optical path-length difference between the two modes that is a few times longer than the measurement depth of each channel. As such, no crosstalk occurs between the interferometric signals of the individual modes. The $\boldsymbol{\eta_{0,1\rightarrow 0,1}}$ sensitivity was measured to be 92 dB using a mirror and a neutral density filter in the sample arm, as described in [88]. The $\boldsymbol{\eta_{0,1\rightarrow 1,1}}$ sensitivity could not be measured using this standard protocol, as no perfect coupling can be achieved between orthogonal modes using a mirror. However, since Fig. 6.2 demonstrates near perfect mode demultiplexing, and since both modes are processed the same way in the optical setup, we can expect both modal sensitivity to be of the same order of magnitude.

### 6.5.3 Data acquisition and post-processing

Raw data acquisition was performed using the proprietary software ThorImageOCT (Thorlabs, USA), which synchronized both spectrometers with the scanning galvanometer system. A custom-made algorithm inspired by previous work [5] was used to correct for background removal, $k$-linearization, dispersion, and to shift the spectrum to precisely adjust the zero-delay position of the two branches at the same axial position. Background removal, $k$-linearization, and dispersion compensation vectors were first computed using the calibration protocol and then applied to $LP_{01}$ and $LP_{11+}$ C-scans individually. Subsequently, a spectrum shift that emulates a zero-delay displacement was applied. The spectrum shift ensures co-localization of both measurements, such that pixel-by-pixel comparison of coupling efficiencies is possible. The optimal shift is calibrated prior to the experiment by comparing the two interferograms obtained for both LP modes with a mirror in lieu of the sample. A discrete Fourier transform is applied to retrieve OCT images for each mode and dB scaling is performed. The full calibration and post-treatment algorithm (implemented in Python 3) is available online on a

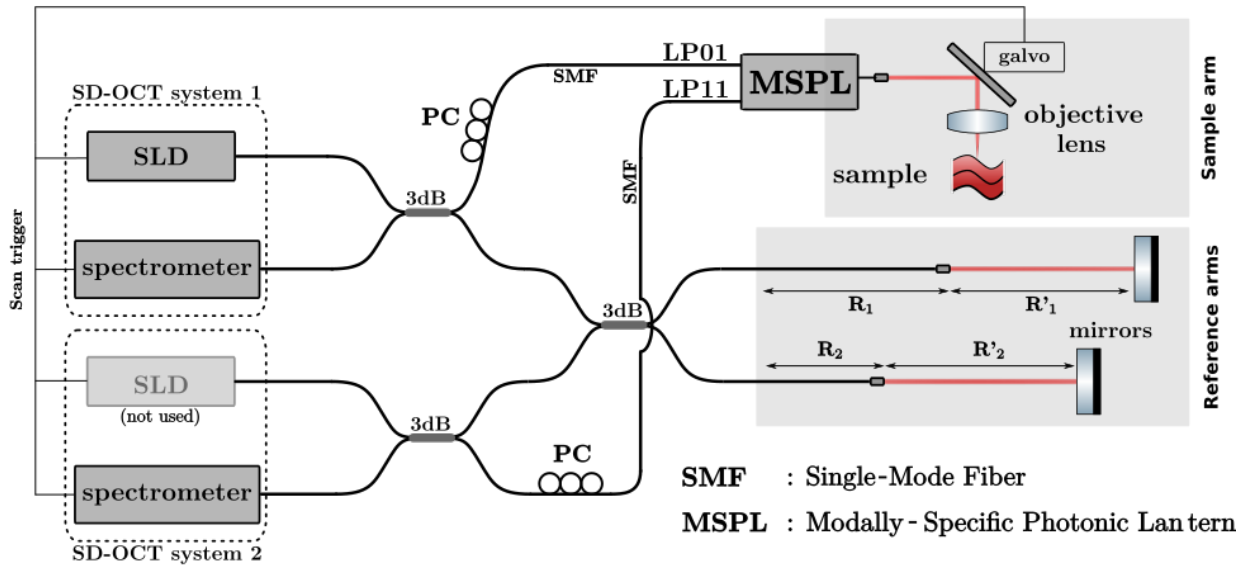



FIGURE 6.4 FM-OCT experimental setup. $R'_1$ and $R'_2$ are the free-space propagation distance, while $R_1$ and $R_2$ are the fiber propagation distances in each branch. SLD stands for superluminescent diode PC stands for polarization controller, galvo stands for galvanometer-mounted mirrors, and 3dB is for 50 :50 fiber couplers.

GitHub repository [122].

### 6.5.4 Sample preparation

In order to experimentally study the FM-OCT contrast mechanism, we use three different samples : two microbeads mix and an *ex vivo* sample of rat lung. The first microbead sample is an optical phantom composed of near-infrared transparent polydimethylsiloxane (PDMS) matrix and $TiO_2$ microbeads (Titanium dioxide powder, Atlantic Equipment Engineers) diameter varying from 0.3 to 10 µm. The sample was prepared with 25 µL of alcoholic solution (70% ethanol) mixed with 15 mg $TiO_2$ microbeads, 10.6 g of PDMS and 1.5 mL of curing agent in an ultrasonic bath. The second microbead sample was made similarly but adding standard size beads (borosilicate glass, Thermofisher 9008 series, 8.4 µm diameter) to the mix with a mass ratio of 6 parts to 1. Finally, the *ex vivo* lung sample was extracted from an adult rat. The lung was not processed prior to imaging.

## 6.6 Results

In this section, we report on experimental validation of the demultiplexing scheme and proof-of-concept of the few-mode OCT imaging with a MSPL. In particular, we applied the tech-

nique to image two different optical phantoms composed of microbeads and *ex vivo* lung samples.

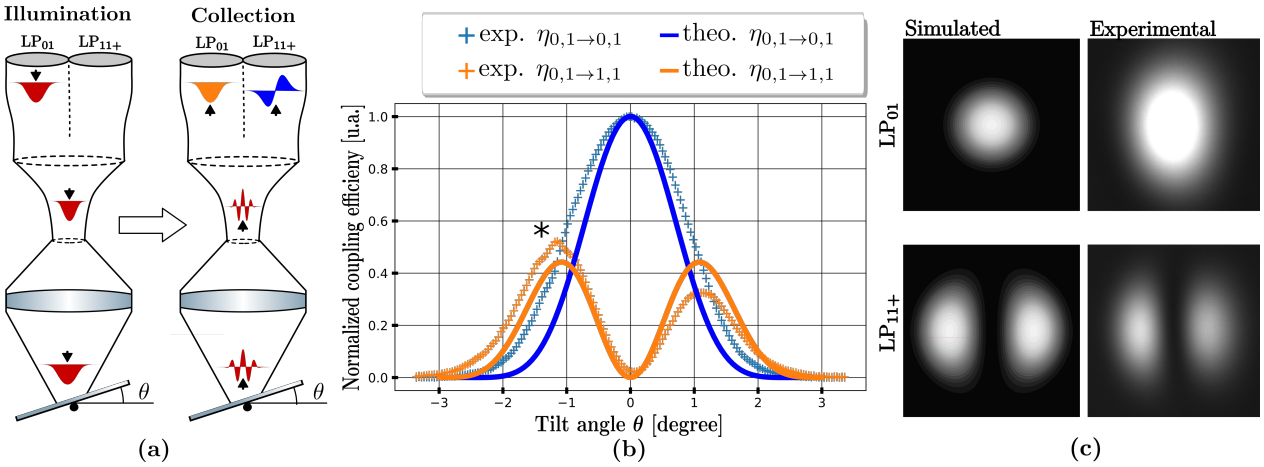



FIGURE 6.5 Validation of the demultiplexing scheme. (a) Optical setup consisting of the MSPL, an imaging lens and tilted mirror for illumination (left) and detection (right). (b) Theoretical (solid lines) and experimental (dashed lines) coupling efficiencies for $LP_{01}$ (blue) and $LP_{11+}$ (orange). (c) Simulated and experimental intensity profiles of the output face of the MSPL, for each mode. The asterisk highlights a notch in the left lobe of the experimental coupling $\eta_{0,1\to1,1}$.

### 6.6.1 Modally-specific photonic lantern validation

To validate the optical behavior of the MSPL with a large bandwidth source, we conducted the experiment with the system described in Fig. 6.4 but using a mirror in place of the sample. Using the unitary property of the Fourier transform, we can infer the total intensity of the light collected from the interferometric signal returned by the OCT system. Total intensity was measured for different mirror tilt angles within the range of ±3 degrees. The optical configuration is depicted in Fig. 6.5 (a) where the left part represents the illumination performed using $LP_{01}$ mode (in red). The tilt of the mirror results in a phase shift of the projected $LP_{01}$ mode along the tilt axis, causing the mode to transform. The right part of Fig. 6.5 (a) shows the transformed mode coupling with each of the branch of the MSPL ($LP_{01}$ in blue and $LP_{11+}$ in orange). Using the direct-space representation of Eq. 6.1 the coupling efficiencies can be written down as

$$\begin{cases} \boldsymbol{\eta_{0,1\to 0,1}}(\theta) = \left|\langle\phi_{0,1}(x,y)|\,\hat{P}(\theta)\,|\phi_{0,1}(x,y)\rangle\right|^2 \\ \boldsymbol{\eta_{0,1\to 1,1}}(\theta) = \left|\langle\phi_{0,1}(x,y)|\,\hat{P}(\theta)\,|\phi_{1,1}(x,y)\rangle\right|^2, \end{cases} \tag{6.11}$$

where $\langle\phi_{0,1}|$ is the $\mathrm{LP}_{01}$ mode field, $\langle\phi_{1,1}|$ the $\mathrm{LP}_{11+}$ mode field, and $\hat{P}(\theta)$ the phase shift operator on the tilt axis $\hat{x}$ with a tilt angle of $\theta$ defined as $\hat{P}(\theta) = \exp\{i\,k\,x\,\tan\theta\}$. Those efficiencies were computed for each mode as a function of the tilt angle of the mirror and measured experimentally. Thus, we can validate the mode-field distribution and demultiplexing scheme by comparing the theoretical predictions to the experiment. In particular, for a null mirror tilt angle, we expect no cross-coupling between the modes. This feature is of utmost importance, as it certifies that the photonic lantern is indeed modally specific. Figure 6.5 (b) shows theoretical (solid blue and orange lines) and experimental (dotted blue and orange lines) normalized coupling efficiencies of the two modes. Figure 6.5 (c) depicts both modes' intensity profiles ($\mathrm{LP}_{01}$ and $\mathrm{LP}_{11+}$ ) as simulated (left) for a perfectly symmetrical FMF and as acquired experimentally (right) at the output of the MSPL. Due to the asymmetric nature of our home-made MSPL, the resulting mode fields are not exactly the same as would be expected of a circularly symmetric FMF fiber. These differences can be visualized by comparing the left and right columns of Fig. 6.5 (c) where the experimental $\mathrm{LP}_{01}$ and $\mathrm{LP}_{11+}$ modes are slightly elongated with respect to the simulated modes for a perfectly symmetric FMF.

### 6.6.2 Phantom imaging

The optical response of a phantom made of microbeads was acquired and analyzed using $\mathrm{LP}_{01}$ for illumination and both $\mathrm{LP}_{01}$ and $\mathrm{LP}_{11+}$ for collection. Figure 6.6 (a to d) show collected scans using $\mathrm{LP}_{01}$ (top) and $\mathrm{LP}_{11+}$ (bottom) modes displayed in logarithmic scale. While Fig. 6.6 (a, b & c) presents results obtained using disperse beads (diameter ranging from 0.3 to 10 µm), sub-figure (d) was acquired using a mixture of standard size beads (8.3 µm) and the disperse beads. Figure 6.6 (a) shows *en face* maximum intensity projection (MIP) of the C-scans collected with $\mathrm{LP}_{01}$ and $\mathrm{LP}_{11+}$ . Figure 6.6 (b) presents a B-scan taken from the same region of interest (ROI) of the optical phantom with enlarged insets (i and ii). The visible structures (white arrows) appearing in Fig. 6.6 (a & b) point at a non-uniform mixture of the microbeads in the phantom. Figures 6.6 (c & d) show two oversampled (by a factor of $\approx 15$) MIPs from two optical phantoms obtained at similar resolution. The first one (c) is made of disperse beads and the second one (d) is made of a mixture of standard size and disperse beads, with the proportion being six parts to one, respectively. It should be pointed out that the contrast of the two images is adjusted for saturation not to occur. Hence, the few scatterers that strongly couple with $\mathrm{LP}_{11+}$ in Fig. 6.6 (d) tend to dim the others. The mixed sample is thus majorly constituted of exactly 8.3 µm beads with a small proportion of beads over and below that size. This sample was produced in order to highlight a size-selective contrast mechanism. Sub-figures (c & d) also include red and blue arrows pointing at specific microbeads for comparison between the two modes. In addition to highlighting the selective

contrast, oversampled images show the experimental footprints of scatterers for each mode : a single lobe for $LP_{01}$ and a double-lobe for $LP_{11+}$ .

In particular, the red arrows show scatterers with a higher coupling efficiency in the $LP_{01}$ mode compared to $LP_{11+}$ mode, while the blue arrows indicate the opposite pattern (lower efficiency).

### 6.6.3 Rat lung imaging

The optical response of an *ex vivo* rat lung was acquired and analyzed using $LP_{01}$ illumination and both $LP_{01}$ and $LP_{11+}$ for collection. The top row shows images collected with $LP_{01}$ , while the bottom row shows images acquired with $LP_{11+}$ . Figures 6.7 (a & b) show B-scans and *en face* view of a freshly excised *ex vivo* rat lung. Two structures, marked with white arrows, can be observed in the images. Fig.6.7 (a & b) show the lung pleura at the air-tissue interface as well as an alveolus. For each collection mode, ROIs were selected, enlarged, and reproduced as insets (i-v) of the corresponding *en face* views. Insets (i-iv) display some of the regions where differential contrasts were observed. In the insets (i-iv), the blue arrows highlight higher $LP_{01}$ mean coupling efficiencies ($\tilde{\boldsymbol{\eta}}_{\mathbf{0,1}}$) while red arrows point to higher $LP_{11+}$ mean coupling efficiencies ($\tilde{\boldsymbol{\eta}}_{\mathbf{1,1+}}$), the red arrows also highlight the double-lobe pattern predicted for single spherical scatterers. While the double-lobe pattern does not certify the presence of a single spherical scatterer, it does ensure a symmetrical structure as discussed in Section 6.4.1. Inset (v) shows homogeneous regions of the rat lung highlighting the speckle pattern of the OCT image. The autocorrelation of the speckle pattern of (iv) is presented in column (b) along with respective theoretical predictions (top-right corner) obtained using Eq. (6.10) for a large bandwidth OCT light source.

## 6.7 Discussion

By combining the coherence gating of OCT with a phase function demultiplexing scheme, FM-OCT unravels the possibility to study unexplored contrast channels. Our approach is based on the use of modally-specific photonic lantern, which allows to efficiently demultiplex and measure mode-coupled backscattered light without compromising OCT signal quality. The proposed optical system (Fig. 6.4) enables parallelization of the measurements, a tight control over dispersion, and OCT zero-delay localization for both modes. These characteristics ensure an optimal co-registration of images for all contrast channels. Moreover, the implementation does rely on off-the-shelf optical components with the only exception being the modally-specific photonic lantern itself, which was custom-made for this application.

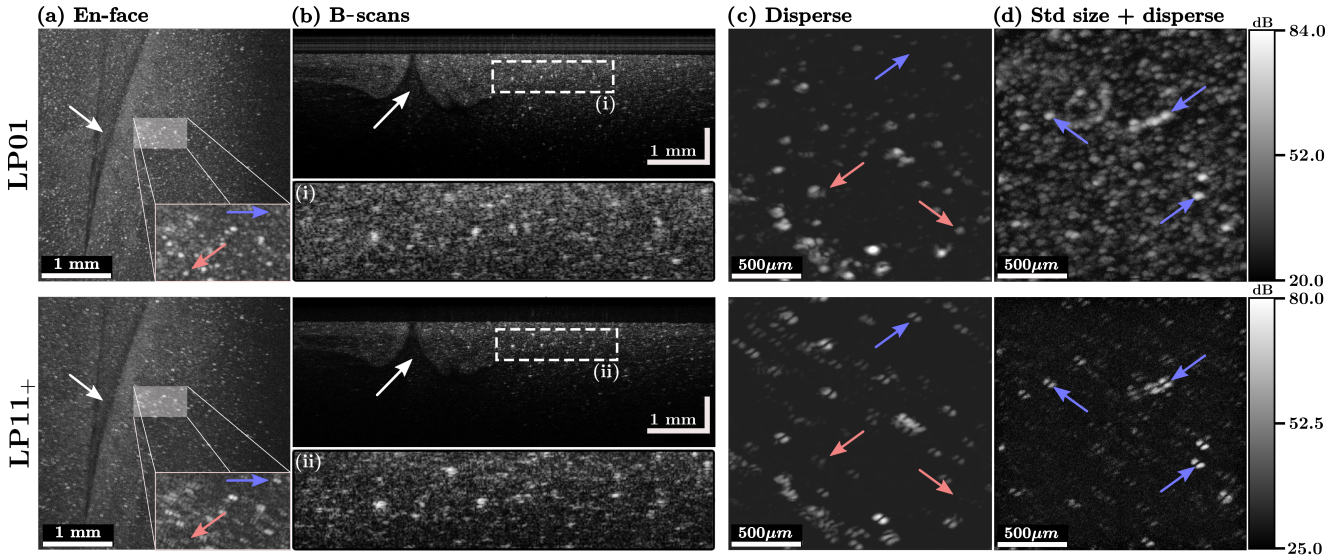



FIGURE 6.6 FM-OCT scans of a microbead optical phantom using $LP_{01}$ (top) and $LP_{11+}$ (bottom). (a) Maximum intensity projection (MIP) of *en-face* view. (b) B-scans obtained using $LP_{01}$ and $LP_{11+}$ with enlarged insets (i & ii). (c-d) Oversampled and zoomed C-scan obtained using disperse $TiO_2$ microbeads (0.3-10 µm) and mono-disperse borosilicate glass beads (8.3 µm), respectively. Sub-figures (d) are presented with their respective logarithmic scale bars.

In our first experiment, a tilted mirror was used to investigate mode coupling. The analysis of the results validates the propagation modes demultiplexing process in three points : it (1) shows the correspondence between the MSPL modes and the theoretical FMF mode, (2) demonstrates a mode demultiplexing as theoretically predicted, and (3) highlights a very low crosstalk for a zero tilt angle, which was demonstrated by $\boldsymbol{\eta_{0,1\rightarrow 1,1}}(0) \approx 0$ (see Fig. 6.5 (b)). However, the small degree of asymmetry of the $\boldsymbol{\eta_{0,1\rightarrow 1,1}}$ and the wider coupling $\boldsymbol{\eta_{0,1\rightarrow 0,1}}$ indicates a slight deviation from the ideal LP modes of an FMF. Additionally, we notice a notch on top of the left lobe of $\boldsymbol{\eta_{0,1\rightarrow 1,1}}$ (highlighted with an asterisk). This notch is caused by the residual influence of one of the fiber cores, which are supposed to vanish in the tapering process. Such minor aberrations can be corrected through design and fabrication improvements of the MSPL, which we will integrate into future developments.

In this work, we also developed and validated a simple model to compute modal coupling efficiencies through the study of *in vitro* and *ex vivo* samples. The study of the optical response of microbeads of varying diameters (ranging from 0.3 to 10 µm) validates two predictions of the coupling model. First, Fig. 6.6 (a & b) shows specific scatterers that appeared brighter when imaged with $LP_{11+}$ compared to $LP_{01}$ (red arrows) and vice versa (blue arrows). Additionally, from Mie scattering theory, we know that larger scatterers also have higher

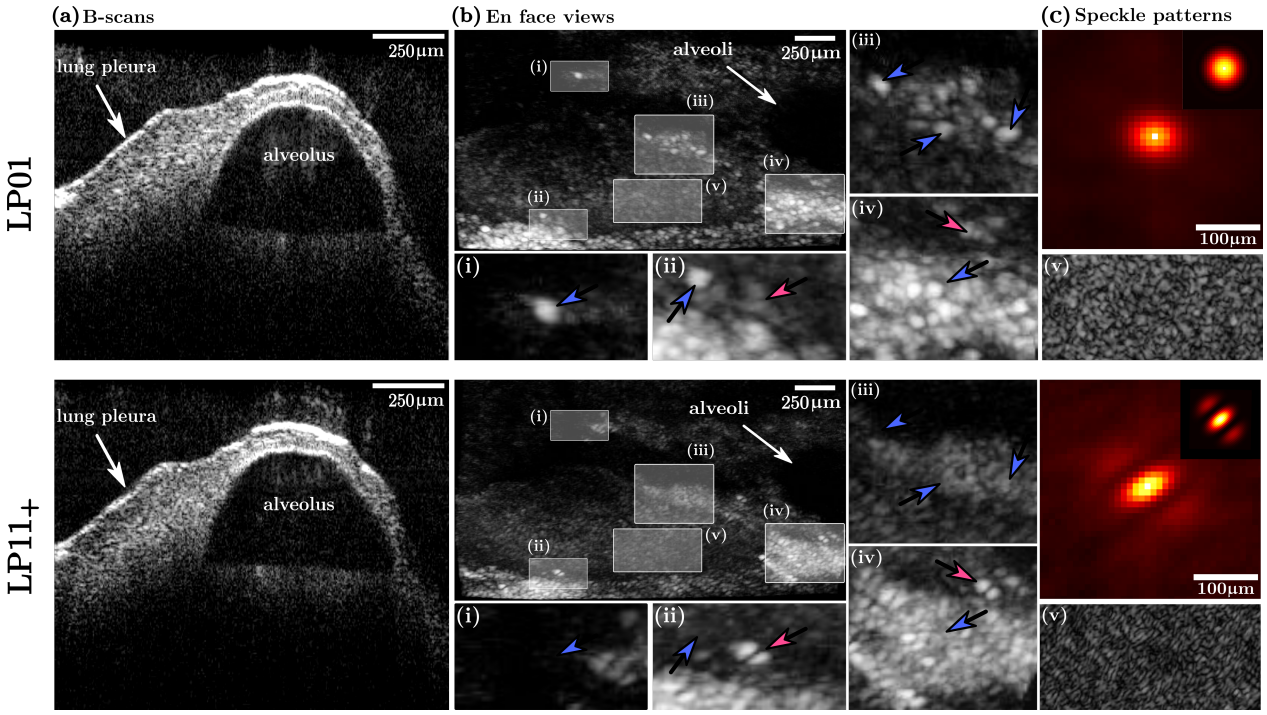



FIGURE 6.7 Adult rat lung imaged with FM-OCT (dB scaling). (a) B-scan of a rat lung using $LP_{01}$ (top row) and $LP_{11+}$ (bottom row). (b) *En-face* view MIP of a rat lung with insets (i-iv) enlarged. Inset (v), reproduced to the right, shows the speckle pattern. (c) Auto-correlation function of speckle pattern with the predicted pattern integrated of the OCT wavelength range (inset).

scattering efficiencies and hence produce brighter spots in OCT scans. As we demonstrated, scatterers with small diameters ($\leq 2\,\mu m$) tend to couple equivalently in both modes, while those with a diameter superior to that value tend to couple more into the $LP_{11+}$ mode. Therefore, the coupling model predicts that brighter spots in $LP_{01}$ imaging tend to appear even brighter in $LP_{11+}$ (red arrows for enhanced coupling). Furthermore, to avoid signal saturation, the non-enhanced scatterer simply appeared dimmer. On the other hand, scatterers marked with blue arrows indicate diminished $LP_{11+}$ coupling and can be associated with scatterers with a diameter comprised in the range of 3 - 7 µm for which the coupling ratio ($\Gamma_{11+}$) is below 1 (Fig. 6.2 (d)). Results obtained with standard size beads (Fig.6.6 (d)) also highlight a consistent coupling mechanism, as most of the beads (majorly composed of standard size 8.3 µm) couple with the same ratio in both $LP_{01}$ and $LP_{11+}$ modes. Additionally, $LP_{11+}$ images obtained from the microbead phantom (Fig. 6.6 (a & c)) feature the predicted double-lobe footprint (Fig. 6.2). The results obtained from the microbead phantom validates the predicted modal signature and demonstrates the possibility of discriminating scatterers based on their size. While we did not yet investigate the optical response of a large

set of mono-dispersed scatterers, this modal signature could be of great interest for sub-resolution sensing, in particular when high sensitivity to scatterer size is relevant. Techniques such as elastic light scattering spectroscopy [49] or inverse spectroscopic optical coherence tomography [168] indeed exploit nuclear-to-cytoplasmic volume ratios to discriminate cancerous versus normal tissues. The investigation of the lung sample shows that most of the latter fall within the regime of a low-coherencesample for which differential coupling was not observed ($\Gamma_{11+} \approx constant$). This observation is consistent with the model description in which the phase function derived from the Born approximation (Eq 6.9) is uniform enough for the coupling to be equal for both modes ($LP_{01}$ and $LP_{11+}$ ). There are however several areas (as shown in Fig. 6.7 (b) insets) for which differential coupling is observed. This is expected as for the porous trait of the lung structures [37, 85]. The differential coupling can thus be associated to high refractive index heterogeneity such as capillaries or cell clusters having a size parameter larger than the threshold value ($\alpha > 6.75$). Some of those particular areas presented in Fig. 6.6 (a) insets also feature the double-lobe pattern specific to single spherical scatterers. The double-lobe pattern also indicates a symmetric structure and therefore supports the hypothesis of cell clusters. No comparison was yet done with histology, which will be integrated into future research. Results from the microbeads phantom and low-coherencesample underline an interesting feature. Small scatterers and low-coherencesamples correspond to low RI correlation lengths and do not feature differential coupling between the two modes. However, in some areas, high RI correlation lengths, originating from structures such as large scatterers produce a differential coupling between the two modes and generate an important source of contrast for OCT. This contrast is based on the size parameter (a combination of scatterer diameter and wavelength) which allows for a certain tunability for highlighting biological structures of interest. These results validate the proposed model and corroborate previously reported results [38]. Moreover, as theoretically predicted, the speckle pattern was very distinctive of the fiber mode with which each image was acquired. We notice that the image obtained with $LP_{11+}$ is less affected by the speckle as its structure is finer than the speckle pattern of $LP_{01}$ . Finally, the speckle autocorrelation associated with each mode was experimentally measured and compared to theoretical predictions (Fig. 6.7 (b)). While results for each mode are concordant, the experimental measurement for $LP_{11+}$ shows dimmer side lobes compared to what would be expected. In summary, we demonstrated a new and efficient technique of studying the optical response of samples using different types of structured light field (LP modes). Additionally, we proposed and validated a simple coupling model that described a contrast based on the refractive index correlation length, which is a mechanism that had already been exploited [38] but not fully characterized. Our work shows that FM-OCT's advantage over conventional OCT is in locating larger cells or clus-

ters of proteins, such as found in amyloid plaques in the brain, in a background of rather homogeneous tissue. Indeed, Fig. 6.2 (c) suggests that the contrast between the two modes is null in the Rayleigh regime, and becomes significant in the Mie regime, especially as the particle size reaches several wavelengths. Furthermore, we provided a proof-of-principle based on a novel modally-specific photonic lantern that allowed for an all-fiber optical circuit. The all-fiber approach permits adding channels without compromising signal quality : indeed, one could now envision scaling up the number of channels with the development of 3- to N-fiber MSPLs. Despite its highly efficient demultiplexing scheme, the proposed optical setup presented some technical limitations. OCT imaging was performed at a wavelength accommodating the operating wavelength of the MSPL, for which devices such as broadband circulators are not common. Following this proof-of-principle, custom fibers will be drawn to design an MSPL at longer wavelength for OCT imaging (e.g. 1300 nm). In addition to allow for better penetration, an MSPL operating at longer wavelengths could be coupled with circulators and integrated in a swept-source OCT system, using two photodetectors (in lieu of spectrometers), for parallel acquisition of the modes ; or even a single photodetector coupled to an optical switch for sequential acquisition of the modes. Also, in the situation where the collecting mode does not feature a rotational symmetry, the polarization state of the incident light field can affect the coupling (*e.g.* microbeads imaging). Future work includes *in vivo* validation of the contrast mechanism in biological tissue.

**Funding**

Natural Sciences and Engineering Research Council (NSERC) of Canada grants #RGPIN-2018-06151 (CB), #RGPIN-2015-04672 and #RTI-2016-00636 (MD), #RGPIN-06404-2016 (NG) and the Fonds de Recherche du Québec – Santé (FRQS) grant #32600 (MD).

**Acknowledgements**

We thank Xavier Attendu for his precious help with the redaction of the manuscript, and Emilie Heckel and Irène Londono for sample preparation.

**Disclosures**

CB, NG : Castor Optics, inc. (I,P), MPdSH, SBB (P)

## Data Availability

Data underlying the results presented in this paper are not publicly available at this time but may be obtained from the authors upon reasonable request.

# CHAPTER 7 STRUCTURED FIELD INTERACTION WITH TURBID MEDIA : A STUDY THROUGH THE LENS OF THE BORN APPROXIMATION

## 7.1 Chapter Context

Contrary to previous chapters, this one is not adapted from any article. This chapter delves into the process of light scattering for structured light field in turbid media. This chapter is a complement to Chapter 5 which presents a similar study but for single scattering events. More specifically, this approach is designed to close the gap in our current model concerning the interaction of fiber optic modes with biological tissues. The objective is to develop an exhaustive framework that encapsulates the dynamics of structured illumination and collection schemes in their interaction with turbid media.

## 7.2 Introduction

The burgeoning field of biomedical imaging necessitates advanced techniques for probing complex biological tissues, often characterized by their turbid nature. This study presents a novel approach using the Born approximation (BA) and Whittle-Matérn (W-M) covariance function to analyze the interaction of structured light fields with such turbid media. The BA, a linear perturbation theory, offers a simplified yet effective means to model the scattering of light within inhomogeneous materials. By applying this approximation to structured light fields, characterized by their non-uniform intensity and phase distributions, we gain insights into the scattering and absorption phenomena in turbid media like human tissues as modeled with a W-M distribution.

The significance of this study lies in the potential of structured light fields to enhance imaging resolution and contrast in biomedical applications. Traditional imaging methods often struggle with the scattering properties of biological tissues as of its complex intricacies, leading to limitations in image analysis. Structured light fields, with their unique structure, could lead toward overcoming these challenges by manipulating the phase and amplitude of the light field to unveil unique interaction features.

Our methodology involves simulating the interaction of various structured light patterns with a range of turbid media, using computational models based on the BA. The outcomes are then compared against another model, namely Lorenz-Mie scattering, to validate its accuracy. This approach provides a quantitative understanding of light-tissue interactions, crucial for

the development of advanced imaging techniques like optical coherence tomography (OCT) and multiphoton microscopy.

The study's implications extend beyond biomedical imaging, potentially impacting fields like optical therapeutics and light-based diagnostic tools. Understanding the interaction of structured light with turbid media could lead to improved methods for targeted drug delivery, non-invasive diagnostics, and enhanced imaging techniques, contributing significantly to medical science and healthcare.

### 7.2.1 Light Field Generation

Structured light fields refers to light beams with non-uniform amplitude transverse distribution, often engineered to form specific patterns like grids, stripes, or more complex shapes. Various techniques have been developed for the engineering of structured light, each presenting its own set of benefits and drawbacks. Significant efforts have been dedicated to the development of refined beam control methodologies such as spatial light multiplexer (SLM) ; however, the resources required for the enhancement of spatial resolution frequently escalates to levels that may be considered economically unfeasible. In contrast, techniques that utilize the demultiplexing of propagation modes in fiber optics leverage the efficient and precise fabrication processes of optical fibers. This approach enables exacting control over the produced modes, benefiting from the inherent precision and efficiency of optical fiber technology, positing an efficient demultiplexing mechanism. Photonic lanterns (PLs) lie in that category of devices enabling the (de)-multiplexing of linearly-polarized (LP) modes, and thus constitutes an ideal platform to use its built-in field structures to probe structured light field interaction with turbid media.

Additionally, while the polarization state of the light field constitutes a significant parameter, this study will primarily focus on examining the interactions of structured scalar light fields, as exemplified by the LP modes, with turbid media, thereby delimiting the scope of analysis to this particular aspect.

### 7.2.2 Born Approximation

The BA is a fundamental concept in scattering theory, particularly applicable to the field of optics and photonics. It simplifies the complex problem of light scattering in inhomogeneous media by assuming the scattering potential is weak compared to the incident wave. This linear approximation allows for the calculation of the scattered field as a perturbation of the incident field, without needing to solve the full wave equation. In particular, the BA is

valid for media where the refractive index variation is small, a common scenario in biological tissues. To derive the first order BA similarly as presented in [96], we start with the Maxwell equations in an unbound-charge and magnetization free media.

$$\begin{cases} \nabla_c \boldsymbol{E} = -\partial_t \boldsymbol{B} \\ \nabla_c \boldsymbol{H} = \boldsymbol{J}_f + \partial_t \boldsymbol{D} \end{cases} \Rightarrow \begin{cases} \nabla_c \boldsymbol{E} = -\partial_t \boldsymbol{B} \\ \nabla_c \left(\mu_0^{-1} \boldsymbol{B}\right) = \partial_t \boldsymbol{D} \end{cases} \Rightarrow \begin{cases} \nabla_c \boldsymbol{E} = -\partial_t \boldsymbol{B} \\ \nabla_c \boldsymbol{B} = \mu_0 \partial_t \boldsymbol{D} \end{cases} , \tag{7.1}$$

where $\nabla_c$ is the curl operator, $\boldsymbol{E}$, $\boldsymbol{B}$, $\boldsymbol{D}$, $\boldsymbol{H}$ and $\boldsymbol{J}_f$ are the electric, magnetic flux density, displacement, magnetic flux intensity and free-charge current vectors, respectively. Using the curl operator on the first line of 7.1 we get

$$\nabla_c \nabla_c \boldsymbol{E} = -\nabla_c \partial_t \boldsymbol{B} = -\partial_t \nabla_c \boldsymbol{B} = -\partial_t \left(\mu_0 \partial_t \boldsymbol{D}\right)$$

Considering a monochromatic impinging light field, we can switch to the time-Fourier domain and replace the $\partial_t$ operator for the pulsation $i\omega_0$. This allows us to obtain

$$\nabla_c \nabla_c \boldsymbol{E} = \mu_0 \, \omega_0^2 \boldsymbol{D} = \mu_0 \, \omega_0^2 \left(\epsilon_0 \boldsymbol{E} + \boldsymbol{P}\right)$$

$$\left(\nabla_c \nabla_c - k_0^2 \, \mathbb{I}\right) \boldsymbol{E} = \mu_0 \, \omega_0^2 \boldsymbol{P} \quad .$$

Assuming a linear dielectric media, we can set $\boldsymbol{P} = \epsilon_0 \, \chi_e \, \boldsymbol{E}$ and decompose the media's susceptibility into an average and deviation component :

$$\chi_e(\boldsymbol{r}) = \langle \chi_e \rangle + \Delta\chi_e(\boldsymbol{r}) \quad ,$$

which translates, in the spatial frequency domain, to

$$\tilde{\chi}_e(\boldsymbol{k}) = \langle \chi_e \rangle \, \delta(\boldsymbol{k}) + \Delta\tilde{\chi}_e(\boldsymbol{k}) \quad .$$

Using the first-order BA we only consider the effect of the incident field on the polarization of the medium

$$\boldsymbol{P} = \epsilon_0 \, \left[\langle \chi_e \rangle + \Delta\chi_e(\boldsymbol{r})\right] \, \boldsymbol{E}_i \quad , \tag{7.2}$$

so that

$$\left(\nabla_c \nabla_c - k_0^2 \, \mathbb{I}\right) \boldsymbol{E}_s = k_0^2 \, \left[\langle \chi_e \rangle + \Delta\chi_e(\boldsymbol{r})\right] \, \boldsymbol{E}_i(\boldsymbol{r}, \omega) \quad .$$

We then set the incident light field to propagates in the $\boldsymbol{k}^i$ direction, and $\boldsymbol{E}_i(\boldsymbol{r}_\perp, \omega)$ represents its transverse profile as depicted in Figure 7.1 and obtain

$$\left(\nabla_c \nabla_c - k_0^2 \, \mathbb{I}\right) \boldsymbol{E}_s = k_0^2 \, \left[\langle \chi_e \rangle + \Delta\chi_e(\boldsymbol{r})\right] \, \boldsymbol{E}_i(\boldsymbol{r}_\perp, \omega) e^{i\boldsymbol{k}^i.\boldsymbol{r}} \quad ,$$

Now expressing the direct spatial space into its Fourier component, the curl operator becomes $-i\boldsymbol{k}\times$ which allows us to write

$$\begin{aligned} -\left[(\boldsymbol{k} \times \boldsymbol{k}\times) + k_0^2 \, \mathbb{I}\right] \tilde{\boldsymbol{E}}_s(\boldsymbol{k}) &= k_0^2 \, (2\pi)^{-1} \int_{\mathbb{R}^3} d\boldsymbol{r} \, \left[\langle \chi_e \rangle + \Delta\chi_e(\boldsymbol{r})\right] \, \boldsymbol{E}_i(\boldsymbol{r}_\perp, \omega) e^{i(\boldsymbol{k}-\boldsymbol{k}^i).\boldsymbol{r}} \\ &= k_0^2 \, \left[\langle \chi_e \rangle \, \delta(\boldsymbol{k} - \boldsymbol{k}^i) + \Delta\tilde{\chi}_e(\boldsymbol{k} - \boldsymbol{k}^i)\right] * \tilde{\boldsymbol{E}}_i(\boldsymbol{k}_\perp) \quad . \end{aligned}$$

This finally leads to

$$\left[\boldsymbol{k} \otimes \boldsymbol{k} + \left(k_0^2 - k_s^2\right) \mathbb{I}\right] \tilde{\boldsymbol{E}}_s(\boldsymbol{k}) = -k_0^2 \, \left[\langle \chi_e \rangle \, \delta(\boldsymbol{k} - \boldsymbol{k}^i) + \Delta\tilde{\chi}_e(\boldsymbol{k} - \boldsymbol{k}^i)\right] * \tilde{\boldsymbol{E}}_i(\boldsymbol{k}_\perp) \quad , \tag{7.3}$$

where $*$ represents the convolution operation, $\delta(\boldsymbol{k} - \boldsymbol{k}^i)$ is the Dirac's delta function, $\otimes$ is the outer product and $k_s$ is the norm of the scattered wavevector. We can approximate the scattered wavenumber as $k_s^2 = k_0^2(1+\langle\tilde{\chi}\rangle)$. Then, applying the first term within the right-hand side parenthesis of Eq. 7.3 on the electric vector leads to

$$(\boldsymbol{k} \otimes \boldsymbol{k}) \, \tilde{\boldsymbol{E}}_s = \boldsymbol{k} \cdot (\boldsymbol{k} \cdot \tilde{\boldsymbol{E}}_s) \quad ,$$

which is null for far-fields as the $\boldsymbol{k}$ and $\boldsymbol{E}$ are posited to be orthogonal. This allows us to get the simplified formulation

$$\left(k_0^2 - k^2\right) \tilde{\boldsymbol{E}}_s(\boldsymbol{k}) = -k_0^2 \, \left[\langle \tilde{\chi}_e \rangle \, \delta(\boldsymbol{k} - \boldsymbol{k}^i) + \Delta\tilde{\chi}_e(\boldsymbol{k} - \boldsymbol{k}^i)\right] * \tilde{\boldsymbol{E}}_i(\boldsymbol{k}_\perp) \quad , \tag{7.4}$$

so that

$$\begin{aligned} \tilde{\boldsymbol{E}}_s(\boldsymbol{k}) &= -\frac{1}{\langle \tilde{\chi}_e \rangle} \, \left[\langle \tilde{\chi}_e \rangle \, \delta(\boldsymbol{k} - \boldsymbol{k}^i) + \Delta\tilde{\chi}_e(\boldsymbol{k} - \boldsymbol{k}^i)\right] * \tilde{\boldsymbol{E}}_i(\boldsymbol{k}_\perp) \\ &= -\left[\delta(\boldsymbol{q}) + \frac{\Delta\tilde{\chi}_e(\boldsymbol{q})}{\langle \tilde{\chi}_e \rangle}\right] * \tilde{\boldsymbol{E}}_i(\boldsymbol{q}_\perp) \quad , \end{aligned} \tag{7.5}$$

where $\boldsymbol{q} = (\boldsymbol{k} - \boldsymbol{k}^i)$ symbolizes the angular frequency displacement relative to the incident wave vector $\boldsymbol{k}^i$. This expression highlights that the vector $\boldsymbol{k}^i$ is instrumental in breaking the symmetry between forward and backward scattering. Furthermore, it is discernible that

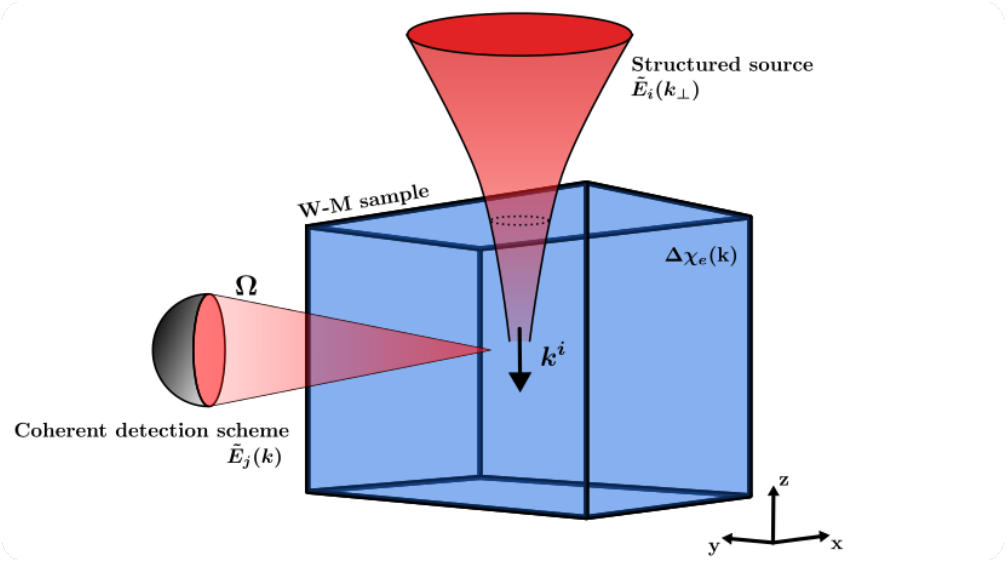



FIGURE 7.1 Representation of the different element composing the scattering setup.

for susceptibility distributions characterized by high angular frequencies, the asymmetry induced by $\boldsymbol{k}^i$ becomes negligible, aligning with predictions from Mie scattering theory which predicts that the smaller the scatterer the more isotropic the scattered far-fields. Moreover, this formulation underpins a critical aspect of the BA method. As highlighted in Equation 7.5, there exists a demonstrable relationship between the constituents of the scattered far-field and the Fourier transform of the medium's susceptibility distribution convolved with the transverse amplitude distribution of the incident field. This fundamental property is of paramount importance in subsequent aspects of the study.

For a linearly polarized incident wave propagating along the $z$-axis and polarized along the $x$-axis, we can deduce the amplitude of the scattered field by projecting the $x$-axis onto the plan perpendicular to the $k$ vector.

$$\tilde{\boldsymbol{E}}_s(\boldsymbol{k}) = \tilde{E}_s(\boldsymbol{k})\hat{E}_s = -\left[\delta(\boldsymbol{q}) + \frac{\Delta\tilde{\chi}_e(\boldsymbol{q})}{\langle\tilde{\chi}_e\rangle}\right] * \tilde{E}_i(\boldsymbol{q}_\perp)\hat{x} \quad ,$$

leading to

$$\tilde{E}_s(\boldsymbol{k}) = -\left[\delta(\boldsymbol{q}) + \frac{\Delta\tilde{\chi}_e(\boldsymbol{q})}{\langle\tilde{\chi}_e\rangle}\right] * \tilde{E}_i(\boldsymbol{q}_\perp)\,\hat{x}\cdot\hat{k}_\perp$$

$$\tilde{E}_s(\boldsymbol{k}) = -\left[\delta(\boldsymbol{q}) + \frac{\Delta\tilde{\chi}_e(\boldsymbol{q})}{\langle\tilde{\chi}_e\rangle}\right] * \tilde{E}_i(\boldsymbol{q}_\perp)\cos\phi \quad , \tag{7.6}$$

where $\phi \in [0, \pi]$ is the polar angle. Equation 7.6 constitutes the fundamental relation that will be used in the following sections. In the situation where the source is a plane-wave and the distribution $\chi_e$ represents a single scatterer for which the dimension is sufficiently small in compared to the wavelength, we retrieve the dipole radiation pattern as shown in Figure. 7.2 which also shows its adequacy with Mie theory.

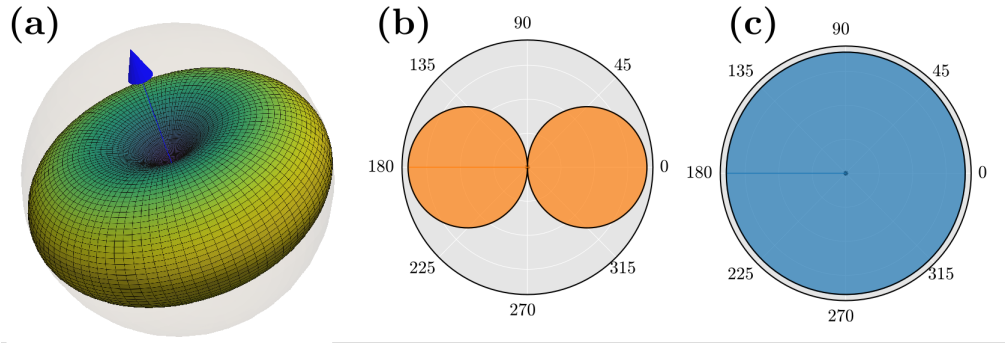



FIGURE 7.2 (a) Scattered far-field for a $\chi_e$ distribution characterizing a small spherical scatterer for an incident field polarized on the blue arrow axis and using the BA. (b & c) scattered far-fields orthogonal projections for a spherical scatterer significantly smaller (ratio of 0.1) than the wavelength using Mie theory.

### 7.2.3 Modeling of Turbid Media

Turbid media, such as biological tissues, are characterized by their random and inhomogeneous nature, leading to complex light scattering and absorption. When light enters such a medium, it undergoes multiple scattering events, which can significantly alter the impinging beam structure. The analysis of how structured light interacts with these scattering events is fundamentally linked to the random distribution of refractive index within the media. Prior to delving into the examination of light-matter interactions within such media, it is imperative to establish a methodology for sample characterization. An exhaustive approach to depict the stochastic continuous medium involves modeling the refractive index correlation function. This function serves as a statistical instrument for characterizing the distribution of tissue structures. A common way to model such a distribution is to use the W-M covariance function [52, 169]. The W-M covariance function family is a three-parameter model as represented by the covariance formulation

$$B(r) = N_c \left(\frac{r}{l_c}\right)^{\frac{D-3}{2}} K_{\frac{D-3}{2}}\left(\frac{r}{l_c}\right) \tag{7.7}$$

where $r$ being the Euclidean distance, $N_c$ is the scaling factor which is proportional to the variance of the distribution, $l_c$ is the correlation length, $K_i$ is the modified Bessel function of order $i$ and finally $D$ is the deterministic factor. The deterministic factor, also labeled fractal index, represents the asymptotic structures of the field distribution [97]. The value of this index is expected to be very close to three when delineating biological sample's refractive index distribution, as it was shown in [169]. As such, in this study, we will assume this parameter to be close to three. It is also important to notice that for a deterministic factor of three and using the first order BA for a plane-wave source, we can retrieve the ubiquitous Henyey–Greenstein phase function [133].

The scaling factor's relationship with the variance of the W-M field varies based on whether the deterministic factor is greater than or less than three. This relationship is described as

$$N_c = \begin{cases} \dfrac{\mathrm{Var}[n]}{\Gamma\left(m - 3/2\right)} & \text{for } D > 3 \\ \dfrac{\mathrm{Var}[n]}{2^{5/2-m}\left(\frac{r_{\min}}{l_c}\right) K_{m-3/2}\left(\frac{r_{\min}}{l_c}\right)} & \text{for } 0 < D \leq 3 \end{cases} .$$

In this context, $r_{\min}$ represents the minimum boundary value, delineating the constraints applied to $B_n$ for evaluation purposes, as discussed in [52]. Despite the inherent complexity of this formulation, the principal interest lies in recognizing that, in both cases $N_c$ is directly proportional to $\mathrm{Var}[n]$.

The W-M covariance family of functions are solutions of the stochastic partial differential equation

$$\left(l_c^2 - \Delta\right)^{\frac{D}{2}} \; X(\boldsymbol{r}) = N_c \, \eta(\boldsymbol{r}) \quad , \tag{7.8}$$

where $\Delta$ is the Laplacian, $X$ is the W-M refractive index field and $\eta$ is a random Gaussian vector [98, 165]. Equation 7.8 suggests that through appropriate discretization of the Laplacian operator, such as employing finite difference methods, it becomes feasible to synthesize a W-M field, thereby facilitating subsequent analytical investigations. We can solve Equation 7.8 using a standard $Ax = b$ solver for a given Gaussian noise seed, as depicted in Figure 7.3 which compares three different W-M fields with correlation length ranging from one to four. Decomposing its spatial-Fourier component, we can rewrite Eq. 7.8 (proof in appendix B) as

$$\tilde{X}(\boldsymbol{k}) = N_c \, \left(l_c^2 + k^2\right)^{\frac{-D}{2}} \; \eta(\boldsymbol{k}) \quad .$$

This formulation indicates that the distribution's angular frequencies are inversely related

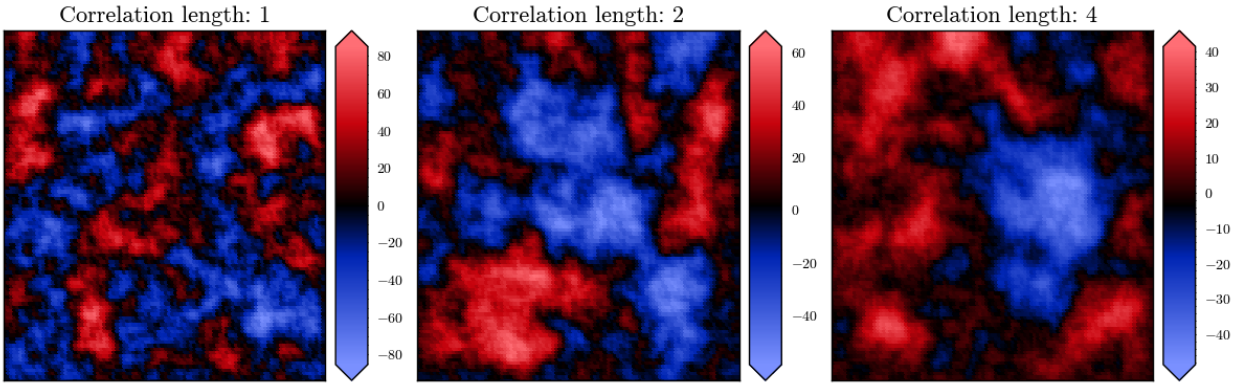



FIGURE 7.3 Depiction of W-M field generated using Eq. 7.8 for three different values of correlation length. All two other parameters are kept at a fixed value of $D = 3$ and $N_c = 1$.

to the correlation length, an important feature that is exploited in scattering-based contrast mechanism technique.

The Fourier transform of the covariance function is given by

$$\tilde{B}(k) = N_c\, l_c \frac{\Gamma(\frac{D-3+d}{2})}{2^{\frac{D-5}{2}}} \frac{(2\sqrt{\pi})^d}{[1+(l_c\, k)^2]^{\frac{D-3+d}{2}}} \quad ,$$

where $\Gamma()$ is the gamma function and $d$ is the number of spatial dimension, which is three in our study case [58], we thus obtain the following equation

$$\tilde{B}(k) = N_c\, l_c \frac{\Gamma(\frac{D}{2})}{2^{\frac{D-5}{2}}} \frac{(2\sqrt{\pi})^3}{[1+(l_c\, k)^2]^{\frac{D}{2}}} \quad . \tag{7.9}$$

## 7.3 Coupling Mechanism

Our goal is to create a model for coupling related to a coherent collection mechanism, using the BA and the formulation for turbid media. This model is intended to be used to describe contrast mechanism based on light scattering. We establish a sesquilinear product to characterize the coherent coupling, $C$, mechanism corresponding to a specific collection field, denoted as $E_j$ in the following way

$$C = E\left[\langle \boldsymbol{E}_j | \boldsymbol{E}_s \rangle\right]_{\boldsymbol{r}} = E\left[\left| \int_{k\in\Omega} d\boldsymbol{k} \tilde{\boldsymbol{E}}_j(\boldsymbol{k}) \cdot \tilde{\boldsymbol{E}}_s(\boldsymbol{k}) \right|^2\right]_{\boldsymbol{r}} \quad , \tag{7.10}$$

where $E\left[.\right]_{\boldsymbol{r}}$ represents the ensemble expectation value over the position. This definition expresses the average coupling value of the scattered field with a collection field. Additionally, assuming that the collection of scattered light is not in the same direction as the source input we can exclude $\boldsymbol{k}^i$ from $\Omega$, enabling us to remove the $\delta(\boldsymbol{q})$ term Eq. 7.6. This non-alignment is characteristic of systems that are based on reflection imaging, where typically, collected light would be collinear but opposite direction with the incident light. Following this, we can rewrite Eq. 7.10 as

$$\begin{aligned} C &= \frac{1}{\langle\tilde{\chi}_e\rangle^2} E\left[\left|\int_{k\in\Omega} d\boldsymbol{k}\, \tilde{E}_j(\boldsymbol{k}) \, - \Delta\tilde{\chi}_e(\boldsymbol{q}) * \tilde{E}_i(\boldsymbol{q}_\perp)\left(\hat{E}_j \cdot \hat{E}_s\right)\right|^2\right]_{\boldsymbol{r}} \\ &= \frac{1}{\langle\tilde{\chi}_e\rangle^2} E\left[\left|\int_{k\in\Omega} d\boldsymbol{k}\, \tilde{E}_j(\boldsymbol{k})\, \Delta\tilde{\chi}_e(\boldsymbol{q}) * \tilde{E}_i(\boldsymbol{q}_\perp)\left(\hat{E}_j \cdot \hat{k}_\perp\right)\cos(\phi)\right|^2\right]_{\boldsymbol{r}} \quad . \end{aligned}$$

Assuming a sufficiently small collecting solid angle $\Omega$ as we can expect from a biomedical imaging technique such as OCT for which numerical aperture (NA) is usually below 0.1, we can approximate the term $\left(\hat{E}_j \cdot \hat{k}_\perp\right)$ to be constant and equal for all $k$ values and equal to one. The implication of a small numerical aperture extends to the nature of the collecting field, suggesting the absence of a longitudinal component. This characteristic allows for the representation of the collecting field in terms of transverse coordinates, analogous to the impinging field. Based on these considerations, the equation can be formulated as follows

$$C = \frac{\cos^2(\phi)}{\langle\tilde{\chi}_e\rangle^2} E\left[\left|\int_{k\in\Omega} d\boldsymbol{k}\, \tilde{E}_j(\boldsymbol{q}_\perp)\, \Delta\tilde{\chi}_e(\boldsymbol{q}) * \tilde{E}_i(\boldsymbol{q}_\perp)\right|^2\right]_{\boldsymbol{r}} \quad . \tag{7.11}$$

In particular, this formulation underscores the coupling dependency on the impinging ($\boldsymbol{E}_i$) and collecting ($\boldsymbol{E}_j$) fields. To highlight these dependencies, we rewrite the coupling factor as $C = C_{ij} = E\left[\langle\boldsymbol{E}_i|\, \Delta\tilde{\chi}_e\, |\boldsymbol{E}_j\rangle\right]_{\boldsymbol{r}}$. Decomposing the squared norm in Eq. 7.11 and using the linear property of the expected value operator, we can rewrite the previous equation as

$$\begin{aligned} C_{ij} &= \frac{\cos^2(\phi)}{\langle\tilde{\chi}_e\rangle^2} \mathrm{E}\left[\int_{\boldsymbol{k}_{1,2}\in\Omega} d\boldsymbol{k}\, \tilde{E}_j(\boldsymbol{q}_{1,\perp})\, \Delta\tilde{\chi}_e(\boldsymbol{q}_1) * \tilde{E}_i(\boldsymbol{q}_{1,\perp})\left(\tilde{E}_j(\boldsymbol{q}_{2,\perp})\, \Delta\tilde{\chi}_e(\boldsymbol{q}_2) * \tilde{E}_i(\boldsymbol{q}_{2,\perp})\right)^*\right]_{\boldsymbol{r}} \\ &= \frac{\cos^2(\phi)}{\langle\tilde{\chi}_e\rangle^2} \int_{\boldsymbol{k}_{1,2}\in\Omega} d\boldsymbol{k}\, \mathrm{E}\left[\Delta\tilde{\chi}_e(\boldsymbol{q}_1)\, \tilde{E}_j(\boldsymbol{q}_{1,\perp}) * \tilde{E}_i(\boldsymbol{q}_{1,\perp})\, \Delta\tilde{\chi}_e(\boldsymbol{q}_2)\, \tilde{E}_j(\boldsymbol{q}_{2,\perp}) * \tilde{E}_i(\boldsymbol{q}_{2,\perp})\right]_r \\ &= \frac{\cos^2(\phi)}{\langle\tilde{\chi}_e\rangle^2} \int_{\boldsymbol{k}_{1,2}\in\Omega} d\boldsymbol{k}\, \mathscr{F}^{-1}\Big\{\mathrm{E}\left[\Delta\chi_e(\boldsymbol{r}_1) \, * E_j(\boldsymbol{r}_{1,\perp})E_i(\boldsymbol{r}_{1,\perp})\, \Delta\chi_e(\boldsymbol{r}_2) \, * E_j(\boldsymbol{r}_{2,\perp})E_i(\boldsymbol{r}_{2,\perp})\right]_r\Big\} \end{aligned}$$

Without loss of generality, we can set the field amplitude in the direct space, $E_j(r)$ and $E_i(r)$ as pure real functions. Using this and the properties of the expected value and variance lets us develop further mode the previous expression, as

$$
\begin{aligned}
C_{ij} &= \frac{\cos^2(\phi)}{\langle\tilde{\chi}_e\rangle^2} \int_{\boldsymbol{k}_{1,2}\in\Omega} d\boldsymbol{k}\, \mathscr{F}^{-1}\left\{ \mathrm{Var}\left[ \Delta\chi_e(\boldsymbol{r})\, \underbrace{E_i(\boldsymbol{r}_\perp) * E_j(\boldsymbol{r}_\perp)}_{\xi_{ij}(\boldsymbol{r}_\perp)} \right]_r \right\} \\
&= \frac{\cos^2(\phi)}{\langle\tilde{\chi}_e\rangle^2} \int_{\boldsymbol{k}_{1,2}\in\Omega} d\boldsymbol{k}\, \mathscr{F}^{-1}\left\{ \mathrm{Var}\left[\Delta\chi_e(\boldsymbol{r})\, \xi_{ij}(\boldsymbol{r}_\perp)\right]_r \right\} \\
&= \frac{\cos^2(\phi)}{\langle\tilde{\chi}_e\rangle^2} \int_{\boldsymbol{k}_{1,2}\in\Omega} d\boldsymbol{k}\, \mathscr{F}^{-1}\Big\{ \mathrm{Var}\left[\Delta\chi_e(\boldsymbol{r})\right]_r \mathrm{Var}\left[\xi_{ij}(\boldsymbol{r}_\perp)\right]_r + \mathrm{Var}\left[\Delta\chi_e(\boldsymbol{r})\right]_r \mathrm{E}\left[\xi_{ij}(\boldsymbol{r}_\perp)\right]_r^2 + \\
&\quad \mathrm{Var}\left[\xi_{ij}(\boldsymbol{r}_\perp)\right]_r \underbrace{\mathrm{E}\left[\Delta\chi_e(\boldsymbol{r})\right]_r^2}_{=0} \Big\} \\
&= \frac{\cos^2(\phi)}{\langle\tilde{\chi}_e\rangle^2} \int_{\boldsymbol{k}_{1,2}\in\Omega} d\boldsymbol{k}\, \mathscr{F}^{-1}\Big\{ \mathrm{Var}\left[\Delta\chi_e(\boldsymbol{r})\right]_r \left( \mathrm{Var}\left[\xi_{ij}(\boldsymbol{r}_\perp)\right]_r + \mathrm{E}\left[\xi_{ij}(\boldsymbol{r}_\perp)\right]_r^2 \right) \Big\} \quad . \\
&= \frac{\cos^2(\phi)}{\langle\tilde{\chi}_e\rangle^2} \int_{\boldsymbol{k}_{1,2}\in\Omega} d\boldsymbol{k}\, \mathscr{F}^{-1}\Big\{ \mathrm{Var}\left[\Delta\chi_e(\boldsymbol{r})\right]_r \, \mathrm{E}\left[\xi_{ij}(\boldsymbol{r}_\perp)^2\right]_r \Big\} \quad .
\end{aligned}
$$

In this expression $\xi_{ij}$ represents the effect of the source and collecting field on the coupling mechanism. Now inserting the covariance description (Eq. 7.7) into the previous equation, we find

$$
C_{ij} = \frac{\cos^2(\phi)}{\langle\tilde{\chi}_e\rangle^2} \int_{\boldsymbol{k}_{1,2}\in\Omega} d\boldsymbol{k}\, \mathscr{F}^{-1}\Big\{ B(\|\boldsymbol{r}\|)\} \, \mathrm{E}\left[\xi_{ij}(\boldsymbol{r}_\perp)^2\right]_r \Big\} \quad .
$$

Having the variance and expected value of the source field and collecting field in the longitudinal direction equating zero we can write the whole integral term as a function of the perpendicular coordinates $\boldsymbol{r}_\perp$.

$$
\begin{aligned}
C_{ij} &= \frac{\cos^2(\phi)}{\langle\tilde{\chi}_e\rangle^2} \int_{\boldsymbol{k}_{1,2}\in\Omega} d\boldsymbol{k}\, \mathscr{F}^{-1}\Big\{ B(r_\perp)\} \, \mathrm{E}\left[\xi_{ij}(\boldsymbol{r}_\perp)^2\right]_r \Big\} \\
&= \frac{\cos^2(\phi)}{\langle\tilde{\chi}_e\rangle^2} \int_{\boldsymbol{k}_{1,2}\in\Omega} d\boldsymbol{k}\, \tilde{B}(k_\perp)\} * \mathscr{F}^{-1}\Big\{ \mathrm{E}\left[\xi_{ij}(\boldsymbol{r}_\perp)^2\right]_r \Big\}(\boldsymbol{k}_\perp) \qquad (7.12)
\end{aligned}
$$

In this expression, the variables $r_\perp$ and $k_\perp$ are defined as the norm of the vector $\boldsymbol{r}_\perp$ and $\boldsymbol{k}_\perp$, respectively.

This last equation elucidates that the selection of the incident field ($\boldsymbol{E}_i$) and the collection field ($\boldsymbol{E}_j$), which compose $\xi_{ij}$, function as probes for assessing the covariance of the electrical susceptibility and by extension the refractive index in the turbid media. Subsequently, inserting Equation 7.9 into Equation 7.12, we acquire the computationally ready formula for the coupling mechanism

$$C_{ij} = A(D)\left(\cos(\phi)\frac{dn}{\langle\tilde{\chi}_e\rangle}\right)^2 \int_{\boldsymbol{k}\in\Omega} d\boldsymbol{k}\, \frac{1}{\left[1+(l_c\, k_\perp)^2\right]^{D/2}} * \mathscr{F}^{-1}\left\{ \mathrm{E}\left[\xi_{ij}(\boldsymbol{r}_\perp)^2\right]_r \right\}(\boldsymbol{k}_\perp) \quad , \quad (7.13)$$

where, $A(D)$ represents a constant term that depends on the deterministic factors.

### 7.3.1 Model predictions

Equation 7.13 serves as the fundamental component in the theoretical framework of this light-matter interaction model. The analysis of the components of the equation that are not integral indicates that the coupling coefficient is directly proportional to the square of the ratio between the variance of the refractive index ($\mathrm{Var}[n]$) and the average value of the refractive index, denoted as $\langle\tilde{\chi}_e\rangle$. This implies that a greater variation in refractive indices enhances the averaged coupling power. The equation also establishes a relationship between the coupling power and the polar angle ($\phi$) of the collection field, which is determined by considering both the incident polarization vector and the $k_i$ vector.

Within the integral portion of the equation, it is discernible that the terms associated with the impinging and collection fields are interchangeable. This characteristic is consistent with the principles of the Lorentz reciprocity theorem. Furthermore, the fraction within the integral suggests a fundamental connection between the correlation length and the transverse angular frequency component of the imaging apparatus. This interrelation signifies that manipulating the angular frequency spectrum of the optical system can be instrumental in determining the media's correlation length. Such an approach is utilized in methodologies like light scattering spectroscopy or techniques that involve varying the NA of the optical system to enable contrast detection. In particular, we understand from that fraction term that to be able to measure a contrast, it is preferable to have the norm of the perpendicular projection of the $k$ vector at least equating the correlation length of the turbid media.

Citing the study in [52], we anticipate that the correlation length, denoted as $l_c$, varies substantially between different biological tissues. Specifically, in the context of rat samples, the correlation length is expected to span from 0.76 µm in brain tissue to 4.05 µm in liver tissue. When considering the standard operational parameters for Optical Coherence Tomography

(OCT), which typically include a numerical aperture (NA) of 0.05 and an central wavelength of 1.31 µm, the product of the correlation length and the transverse wave vector, $l_c, k_\perp$, is projected to lie within the range of 0.1 to 1.0. This range indicates that the potential to detect and measure contrast variations is feasible, albeit the degree of detectability is dependent on the specific type of tissue under examination. This variability in contrast detection is crucial for applications in tissue differentiation and characterization, such as OCT imaging techniques.

### 7.3.2 Challenges and Future Directions

The model, grounded in the BA framework, offers a valuable predictive tool, especially pertinent in techniques that facilitate depth segmentation like confocal microscopy and OCT. Its ability to link measurable quantities to intrinsic turbid sample properties gives it a great potential for bringing into light some unexplored contrast mechanism in the real of biomedical scattering analysis. Additionally, the model provides an adequate framework to explore and understand the effect of structured illumination and collections schemes on the measured coupling quantities. Predictions of the model were skimmed over in Chapter 6, but a more profound study on practical applications, particularly in the realms of medical imaging and therapeutic interventions, would enhance its relevance.

# CHAPTER 8 GENERAL DISCUSSION

## 8.1 Achievement of Research Objectives

This thesis investigates the advancement and integration of an innovative fiber optic component within the domain of biomedical imaging systems. Chapter 1 delineates precise research objectives aimed at accomplishing this objective. Subsequent sections expand upon the attainment of each objective, emphasizing critical components and discoveries. Additionally, the dissertation explores the interconnections between its chapters and their relevance to both current and prospective research efforts.

### 8.1.1 Fiber Component Software and Hardware Design

Chapter 3 and 4 of this thesis delve the development and application of SuPyMode, a novel open-source software for fiber optics design analysis. Developing a model and tool for fiber optic component design holds paramount importance, particularly in the context of emerging innovations like photonic lanterns (PLs).

Fiber optic components play a pivotal role in a wide array of applications, including telecommunications, biomedical imaging, and data transmission. A comprehensive design model facilitates the efficient exploration of novel components, such as photonic lanterns, by providing a systematic framework for their development. Such models enable researchers and engineers to predict and optimize the performance characteristics, such as signal propagation and bandwidth, thus reducing the need for expensive and time-consuming trial-and-error experiments. In the case of PLs, which offer unique capabilities for manipulating light and tailoring its propagation, a well-established design tool is essential for harnessing their full potential in applications ranging from astrophysics to telecommunications. Consequently, the creation of a robust model and tool for fiber optic component design accelerates the pace of technological advancement and enhances our ability to harness the benefits of cutting-edge optical innovations. Implementing solvers for the eigenmode expansion (EME) and coupled-mode theory (CMT) framework, SuPyMode enables simulating mode-propagation in tapered fiber optics component. Consequently defining the adiabatic criterion parameter, the library allows for precise analysis, design, and optimization of tapered optical structures to achieve unprecedented features. The library, additionally, defines fiber structure fusion process for accurate modeling of actual experimental conditions. This piece of software was exploited to demonstrate how the use of double clad fiber can be employed to enhance the adiaba-

tic criterion, enabling to manufacture of large-bandwidth modally-specific photonic lantern (MSPL) with very low cross-talk. Meticulous analysis of those results allowed devising a robust optical coherence tomography (OCT)-specific MSPL for biomedical application in the near-infrared region. The results in Chapters 3 and 4 reveal the utility of simulation tools in developing efficient, novel MSPL devices. Chapter 3 demonstrates the accuracy of the software through theoretical and simulation comparisons. However, the complexity of replicating fusion and taper experiments precluded detailed experimental validation. A thorough comparison of software predictions with experimental outcomes would be ideal but requires advanced equipment. Despite these challenges, SuPyMode offers a rapid means to evaluate manufacturing designs, assess feasibility, and discover new features like mode-skipping.

### 8.1.2 Structured Light-Field and Matter Interaction

Research objective two revolves around delineating the interaction process between structured field light source and turbid matter. The interaction between structured light sources and turbid matter, exemplified by biological samples, has remained relatively underexplored within the scientific community. This scarcity of research can be attributed, in part, to the inherent complexity of such interactions, characterized by the scattering, absorption, and diffusion of light within the turbid medium. Furthermore, the unique attributes of structured light, which encompass a variety of spatial patterns and phase profiles, introduce an additional layer of intricacy to the problem. However, the need for a fundamental model that elucidates the interactions between structured light and turbid matter is of paramount importance. Such a model would provide invaluable insights into phenomena that have relevance across multiple disciplines, including biophotonics, biomedical imaging, and optical communications. By comprehensively understanding the interplay between structured light and turbid media, researchers can enhance the precision and efficacy of various optical techniques, ultimately advancing the frontiers of science and technology in fields that rely heavily on the manipulation and analysis of light in complex environments.

Chapters 5 and 7 explores two avenues that are found to be promising in terms of model predictions. The former exploits the Mie scattering framework to explore the different contrast mechanisms inherent to scattering event, including a detection schemes. The simulation tool (PyMieSim) presented in Chapter 5 enables efficient analysis of those mechanisms. Notably, PyMieSim was exploited to investigate the effect of scatterer size on the light coupling into coherent and structured field, demonstrating a potential sub-resolution sensing mechanism.

Chapter 7 delve into the scattering problem through the Born approximation (BA) for which the scope of validity is retrained to media with low electric susceptibility variance. This

chapter develops a mathematical model for turbid media interaction with structured and coherent illumination and collection schemes and derives equations linking the average coupling power in terms of key parameters that describe the media and both illumination and collections fields. Initial quantitative assessments indicate that media properties, similar to those in biological samples, could produce varying contrasts. These chapters outline the potential of structured illumination and collection in biomedical imaging. However, a meticulous experimental validation is pending.

### 8.1.3 Experimental Validation

Research objective three is about developing an imaging system incorporating the newly developed MSPL and assessing the new contrast mechanism, as well as juxtaposing the experimental measurements to the model predictions. Chapter 6 describes the development of the first few-mode optical coherence tomography (FM-OCT) design, expanding on the technical aspect, the model predictions and analysis on the measurements. Devising such a novel experiment can be proven a technical challenge, given the absence of precedence in the conception of analogous systems.

One of the primary technical challenges revolves around addressing the disparities inherent in the two channels afforded by the (two-mode) FM-OCT. Notably, the OCT source's central wavelength at 930nm presents a significant hurdle due to the considerable deviation from the wavelength associated with low material dispersion (1300nm). This dispersion effect is notably significant for OCT for the resolution of optical system is heavily impacted by dispersion mismatch between the sample and reference arms [99]. From this entails the requirement to meticulously mitigate the mismatch through the use of hardware and software calibrations.

Using the constructed FM-OCT system, we measured various samples, confirming features predicted by developped models and tools. Notably, we observed the scatterer footprint dependent on the collection field, as predicted by PyMieSim. We also noted a coupling contrast related to scatterer size and consistent coupling behavior in turbid samples, partly validating our predictions.

This overview highlights the promise of MSPL for enhancing imaging contrast, but it underscores the need for thorough, systematic investigation into the coupling behavior using well-characterized imaging samples.

## 8.2 Ongoing and Future Research

### 8.2.1 Manufacturing Higher-Order Modes MSPLs

The optical fiber component (MSPL) developed in this study represents a preliminary step in the advancement of more intricate components enabling the (de)-multiplexing of higher order modes. Currently, components have been engineered to accommodate up to four modes.

Nevertheless, it is plausible to design an even more sophisticated system. It should be noted that when designing MSPL, the complexity of fabrication is not linearly correlated with the number of modes. Instead, it exhibits a factorial relation due to the necessity to prevent coupling between each mode pair. It follows that a meticulous analysis of the design parameter space is required for devising new components.

In the realm of fiber optics, (de)-multiplexing of propagating modes holds significant industrial relevance, particularly for telecommunications applications. The MSPLs possess a largely untapped potential, wherein the intrinsic mode structure can be leveraged to attain novel features. For example, research into orbital angular momentum modes facilitated by photonic lanterns is currently gaining momentum, as evidenced by studies such as [28, 42]. These modes exhibit potential in diverse sectors, including quantum optics, as referenced by [78, 104], and imaging, as cited by [94].

The laboratory-based methodology we have pioneered, which ensures robustness with minimal modal cross-talk, shows promise for the advancement of these technologies. Within imaging applications, the generation of $LP_{0n}$ is of particular interest as they arbor the same circular symmetry as the fundamental mode, labeled $LP_{01}$. This trait makes them suitable for techniques such as super-resolution imaging, where the precise control over the mode field structure and relative phase enables a stable mode superposition to decrease the generated spot-size at the focal point. Following our work on producing ever-increasing higher order modes, we can expect to devise the second available necessary mode ($LP_{02}$) for such application with a 5-mode MSPL.

### 8.2.2 Modeling Light-Tissue Interaction

Advancements in the domain of structured light illumination and its integration into imaging systems represent a two-fold exploration. The strategic development of both the methodology and the associated computational models is critical to grasp the full potential of this burgeoning technology. Despite the substantial investment in hardware innovation, as demonstrated by Eugui et al. [39] and subsequent studies, progress in the domain of interaction modeling

has been comparatively limited, resulting in heuristic and complex interpretative processes.

Chapters 5 and 7 within this document were dedicated to establishing a foundational framework for interaction modeling. Specifically, Chapter 5 addresses the interactions involving singular particles, whereas Chapter 7 extends the discussion to continuous sample distributions, pertinent to biological tissues.

Predictive outcomes discussed in these chapters, with some validated in Chapter 6, showcase the versatility of the developed tools. These tools have demonstrated potential applications that span from single-particle detection to light scattering spectroscopy, as explored by Steelman [145]. MSPLs are posing as an ideal platform for the empirical validation of these predictions due to their capacity for precise control over the emitted mode fields.

For empirical substantiation, an experimental setup involving microbeads with controlled dimensions and known refractive indices could be utilized to confirm the precise coupling mechanisms of MSPL as a function of microbead diameter. Such validation would significantly contribute to the adoption and application of MSPL technologies in the fields of imaging and sensory instrumentation.

### 8.2.3 Toward Super-Resolution

Stimulated emission depletion microscopy (STED) microscopy is a super-resolution imaging technique that overcomes the diffraction limit of traditional light microscopy. This method employs two laser beams : a Gaussian-shaped excitation beam to illuminate and excite the fluorescent molecules in a specimen, and a donut-shaped depletion beam, which selectively de-excites fluorescence around the focal point, effectively shrinking the area of illumination. By meticulously aligning these beams, STED microscopy can achieve resolutions beyond the conventional limit, often down to the nanometer scale. This breakthrough has vastly enhanced our ability to visualize and study biological structures and processes at the cellular and subcellular levels, opening new frontiers in biological and medical research.

The PL ability to generate precise mode field places them as a pivotal technology in this regard. Specifically, generated first three scalar modes of optical fibers, designated as LP01, LP11$a$, and LP11$b$, are optimally suited for this application. The fundamental mode, LP01, serves as the fluorescence excitation beam, while a combination of the two $LP_{11}$ modes forms the donut-shaped depletion beam as depicted in Figure 8.1. This methodology presents several advantages over traditional STED microscopy techniques, which typically employ phase masks or spatial light multiplexers (SLMs). Phase masks and SLMs are inherently wavelength-dependent, whereas PLs can be engineered for broad bandwidth sources. Fur-

thermore, the generated modes within a PL are intrinsically co-registered, enhancing the technique's resistance to vibration and eliminating the requirement for meticulous alignment processes that are indispensable in conventional STED microscopy setups. The use of fiber-based devices also enables the miniaturization of the imaging technique enabling for *in-vivo* imaging which is a crucial trait for bringing a technique to practical applications.

Following this, and conjointly with Prof. Weiss laboratory, we are working on bringing up this promising project in parallel to the filing of a patent on the technique.

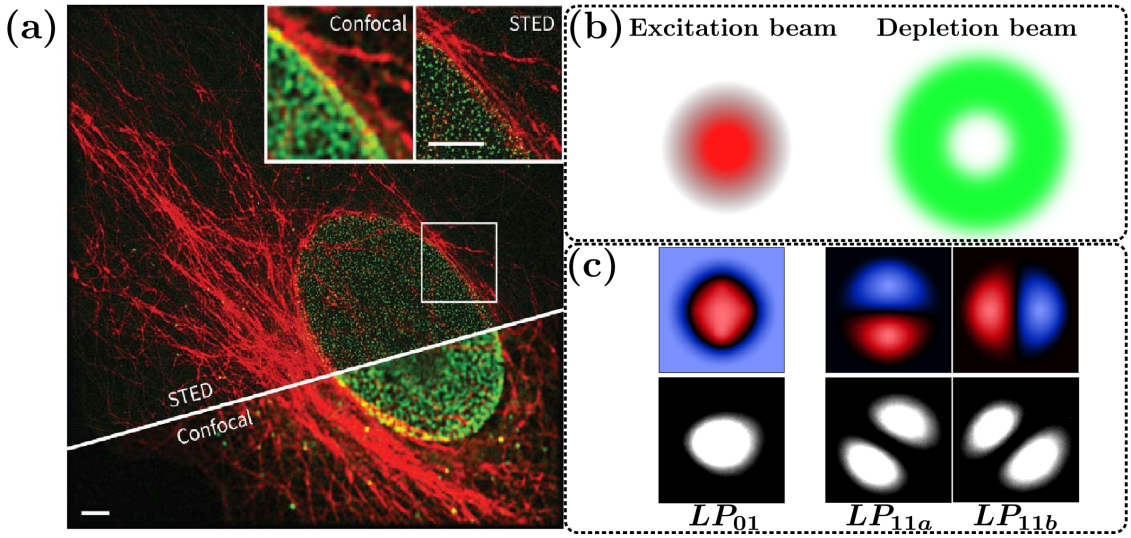



FIGURE 8.1 STED microscopy. (a) Comparison of STED microscopy with confocal. Figure extracted from [54]. (b) Depiction of the two necessary source structures (Gaussian and donut-shaped) for STED microscopy. (c) Simulation and experimental of the mode generated with a 3-mode photonic lantern.

# CHAPTER 9 CONCLUSION

## 9.1 Summary of Work

With the emergence of fiber optics, the biomedical imaging field witnessed a great improvement in the miniaturization of medical instruments, enabling in-depth and *in-vivo* analysis of biological samples. Whereas the application of fiber optics for developing less invasive techniques has been extensively explored, the full potential of fiber optics remains untapped in its current implementation. In this thesis, I worked toward the exploration of the potential contrast mechanisms empowered employing higher-orders fiber propagation modes, developing the tools for developing such systems and the model to explore the contrast mechanisms.

Firstly, I investigated different design for manufacturing robust and large-bandwidth modally-specific photonic lanterns (MSPLs) adapted for optical coherence tomography (OCT) source centered at 930nm. Doing so, I have developed the numerical tools for exploring different designs, delineating the fabrication recipes. Such recipes include the type of fiber employed, their relative positions, the fusion process of the total structure and the tapering process. Incorporating eigenmode expansion (EME) and coupled-mode theory (CMT) numerical method, the developed tool enables for testing different fused fiber configurations yielding a paramount design metric labeled as adiabatic criterion which renders information on the feasibility of a proposed design. This tool, packaged as a full-fledged open-sourced software, was tested against theoretical predictions with great accuracy and has been instrumental in the development of practical and more complex components including 2-, 3- and 4-modes MSPL as it was demonstrated in Chapter 4.

Secondly, I explored different avenues to model the interaction of structured field with turbid media taking account of the light source, the interaction process and the collection with the detector which can be either coherent or incoherent. Such interactions are inherently difficult to solve due to the vectorial nature of light fields and can become prohibitively slow to compute. It is thus necessary to adequately choose the mathematical and computational framework to encompass the problem. As it was highlighted in Chapter 5 and 7, I examined two different analysis methods which are the single scattering approach using Lorenz-Mie scattering mathematical approach and turbid medial scattering using the Born approximation. Both methods are disparate in how they comprehend the fundamental interaction. The Lorenz-Mie framework provides an exact yet truncated expression for the near and far-field solutions of a single scattering event, tailored to a specific scatterer geometry. On the other hand, the Born approximation offers an approximate solution for interactions within a vo-

lume with a continuously distributed refractive index, positing of minimal variation in the refractive index within that volume. Using the developed numerical models, I was able to extract predictions that were later experimentally corroborated.

Thirdly, with the MSPL designed for OCT system, I developed a 2-mode few-mode optical coherence tomography (FM-OCT) using the first two modes of an optical fiber, i.e., $LP_{01}$ and $LP_{11}$. Those modes sporting opposite symmetries on one axis, they were predicted to delineate individual scatterers in a very differently (a concept termed the scatterer footprint). This first prediction on the scatterer footprint being a function of the collection mode and scatterer geometry was experimentally validated to make a first proof-of-concept on sub-resolution sensing mechanisms. Furthermore, it was observed that the geometry of the scatterers also contributed to variations in the coupling behavior with the different modes. The gist of this section of the thesis is that the modal coupling tends to be equivalent for scatterer significantly smaller than the wavelength, conversely, larger scatterers demonstrate a propensity for preferential coupling with specific modes conditional on their precise geometry.

## 9.2 Outlook

This dissertation presents a methodical investigation to develop a framework for advancing MSPLs in biomedical imaging applications. It primarily seeks to define the fundamental interaction principles of these systems. Establishing this initial foundation is crucial for the evolution of imaging technology, emphasizing the need for ongoing research to apply theoretical discoveries in practical settings.

The study detailed herein includes both simulation and experimental analysis to shed light on how structured fields interact with biological tissues. This research is key to more widely incorporating photonic lantern technology into biomedical imaging. In support of these research efforts, this thesis has also led to the creation and refinement of numerical tools, which have been made available as open-source for broader academic use.

At the heart of this research is the empirical demonstration of a new contrast mechanism based on the geometry of scatterers, specifically their form factor and refractive index. Subsequent studies aim to further delineate this mechanism's boundaries, facilitating the design of advanced sensing systems. While the current iteration of this technology has been applied within the realm of biomedical imaging, its utility extends to a variety of other disciplines that rely on phase-sensitive detection methods.

# REFERENCES


[1] Mehreen Adhi and Jay S Duker. Optical coherence tomography–current and future applications. *Current opinion in ophthalmology*, 24(3) :213, 2013.

[2] Leonardo A Ambrosio and Hugo E Hernández-Figueroa. Integral localized approximation description of ordinary bessel beams and application to optical trapping forces. *Biomedical optics express*, 2(7) :1893–1906, 2011.

[3] James L Arbuckle. Amos™ 7.0 user's guide. *Amos Development Corporation*, 1995.

[4] Bruce Archambeault, Omar M. Ramahi, and Colin Brench. *The Finite-Difference Time-Domain Method*, pages 35–67. Springer US, Boston, MA, 1998.

[5] Xavier Attendu, Roosje M. Ruis, Caroline Boudoux, Ton G. van Leeuwen, and Dirk J. Faber. Simple and robust calibration procedure for k-linearization and dispersion compensation in optical coherence tomography. *Journal of Biomedical Optics*, 24(5) :1 – 11, 2019.

[6] Egidijus Auksorius, Dawid Borycki, and Maciej Wojtkowski. Multimode fiber enables control of spatial coherence in fourier-domain full-field optical coherence tomography for in vivo corneal imaging. *Opt. Lett.*, 46(6) :1413–1416, Mar 2021.

[7] V. Backman, R. Gurjar, K. Badizadegan, I. Itzkan, R. R. Dasari, L. T. Perelman, and M. S. Feld. Polarized light scattering spectroscopy for quantitative measurement of epithelial cellular structures in situ. *IEEE Journal of Selected Topics in Quantum Electronics*, 5(4) :1019–1026, 1999.

[8] V Backman, Michael B Wallace, LT Perelman, JT Arendt, R Gurjar, MG Müller, Q Zhang, G Zonios, E Kline, T McGillican, et al. Detection of preinvasive cancer cells. *Nature*, 406(6791) :35–36, 2000.

[9] Vadim Backman, Adam Wax, and Hao Zhang. *A Laboratory Manual in Biophotonics*. CRC Press, United States, 2017.

[10] Tatyana A Bashkatova, Alexey N Bashkatov, Vyacheslav I Kochubey, and Valery V Tuchin. Light-scattering properties for spherical and cylindrical particles : a simple approximation derived from mie calculations. In *Saratov Fall Meeting 2000 : Optical Technologies in Biophysics and Medicine II*, volume 4241, pages 247–259. International Society for Optics and Photonics, 2001.

[11] Paul Bassan, Achim Kohler, Harald Martens, Joe Lee, Edward Jackson, Nicholas Lockyer, Paul Dumas, Michael Brown, Noel Clarke, and Peter Gardner. Rmies-emsc

correction for infrared spectra of biological cells : Extension using full mie theory and gpu computing. *Journal of biophotonics*, 3(8-9) :609–620, 2010.

[12] Simon Bolduc Beaudoin. Révision du processus de fabrication de coupleurs fusionnés à quelques fibres. Master's thesis, École Polytechnique de Montréal, 12 2018.

[13] Moritz Beller, Georgios Gousios, and Andy Zaidman. Travistorrent : Synthesizing travis ci and github for full-stack research on continuous integration. In *2017 IEEE/ACM 14th International Conference on Mining Software Repositories (MSR)*, pages 447–450. IEEE, 2017.

[14] Sebastian Berisha, Thomas van Dijk, Rohit Bhargava, P Scott Carney, and David Mayerich. Bim-sim : Interactive simulation of broadband imaging using mie theory. *Frontiers in physics*, 5 :5, 2017.

[15] T. A. Birks, I. Gris-Sánchez, S. Yerolatsitis, S. G. Leon-Saval, and R. R. Thomson. The photonic lantern. *Adv. Opt. Photon.*, 7(2) :107–167, Jun 2015.

[16] T. A. Birks, I. Gris-Sánchez, S. Yerolatsitis, S. G. Leon-Saval, and R. R. Thomson. The photonic lantern. *Adv. Opt. Photon.*, 7(2) :107–167, June 2015.

[17] T. A. Birks, B. J. Mangan, A. Díez, J. L. Cruz, and D. F. Murphy. "photonic lantern" spectral filters in multi-core fibre. *Opt. Express*, 20(13) :13996–14008, Jun 2012.

[18] Timothy A Birks, I Gris-Sánchez, Stephanos Yerolatsitis, SG Leon-Saval, and Robert R Thomson. The photonic lantern. *Advances in Optics and Photonics*, 7(2) :107–167, 2015.

[19] Timothy A Birks and Youwei W Li. The shape of fiber tapers. *Journal of lightwave technology*, 10(4) :432–438, 1992.

[20] Joss Bland-Hawthorn, SC Ellis, SG Leon-Saval, R Haynes, Martin M Roth, H-G Löhmannsröben, AJ Horton, J-G Cuby, Tim A Birks, JS Lawrence, et al. A complex multi-notch astronomical filter to suppress the bright infrared sky. *Nature communications*, 2(1) :581, 2011.

[21] Craig Bohren and Donald R. Huffman. *Angular Dependence of Scattering*, chapter 13, pages 381–428. John Wiley & Sons, Ltd, 2007.

[22] Craig F Bohren and Donald R Huffman. *Absorption and scattering of light by small particles*. John Wiley & Sons, 2008.

[23] Tami C Bond, Gazala Habib, and Robert W Bergstrom. Limitations in the enhancement of visible light absorption due to mixing state. *Journal of Geophysical Research : Atmospheres*, 111(D20), 2006.

[24] Jacques Bures. *Optique guidée : fibres optiques et composants passifs tout-fibre*. Presses inter Polytechnique, 2009.

[25] John Charles Butcher. A history of runge-kutta methods. *Applied numerical mathematics*, 20(3) :247–260, 1996.

[26] Guillem Carles, Paul Zammit, and Andrew R. Harvey. Holistic monte-carlo optical modelling of biological imaging. *Scientific Reports*, 9, 2019.

[27] Kevin J Chalut, Michael G Giacomelli, and Adam Wax. Application of mie theory to assess structure of spheroidal scattering in backscattering geometries. *JOSA A*, 25(8) :1866–1874, 2008.

[28] Liang Chen, Huiyi Guo, Siyu Chen, Zhi Wang, and Yan ge Liu. Mode-group selective photonic lanterns for multiplexing multi-order orbital angular momentum modes. *Opt. Express*, 31(15) :25128–25142, Jul 2023.

[29] Debaditya Choudhury, Duncan K McNicholl, Audrey Repetti, Itandehui Gris-Sánchez, Shuhui Li, David B Phillips, Graeme Whyte, Tim A Birks, Yves Wiaux, and Robert R Thomson. Computational optical imaging with a photonic lantern. *Nature communications*, 11(1) :5217, 2020.

[30] Kyungwon Chun, Huioon Kim, Hyounggyu Kim, Kil Su Jung, and Youngjoo Chung. Gmes : a python package for solving maxwell's equations using the fdtd method. *Computer Physics Communications*, 184(4) :1272–1279, 2013.

[31] R Correia, S James, SW Lee, SP Morgan, and S Korposh. Biomedical application of optical fibre sensors. *Journal of Optics*, 20(7) :073003, 2018.

[32] Yann Cotte, M. Fatih Toy, Nicolas Pavillon, and Christian Depeursinge. Microscopy image resolution improvement by deconvolution of complex fields. *Opt. Express*, 18(19) :19462–19478, September 2010.

[33] Martin Poinsinet de Sivry-Houle, Simon Bolduc Beaudoin, Simon Brais-Brunet, Mathieu Dehaes, Nicolas Godbout, and Caroline Boudoux. All-fiber few-mode optical coherence tomography using a modally-specific photonic lantern. *Biomedical Optics Express*, 12(9) :5704–5719, 2021.

[34] Martin Poinsinet de Sivry-Houle, Simon Bolduc Beaudoin, Simon Brais-Brunet, Mathieu Dehaes, Nicolas Godbout, and Caroline Boudoux. All-fiber few-mode optical coherence tomography using a modally-specific photonic lantern. *Biomed. Opt. Express*, 12(9) :5704–5719, Sep 2021.

[35] Rodrigo Itzamna Becerra Deana, Martin Poinsinet de Sivry, Simon Bolduc Beaudoin, Caroline Boudoux, Stéphane Virally, and Nicolas Godbout. Short mode-selective photonic lanterns using double-clad fibers. In Lynda E. Busse and Yakov Soskind, editors,

*Photonic Instrumentation Engineering X*, volume PC12428, page PC1242802. International Society for Optics and Photonics, SPIE, 2023.

[36] Rebekah A. Drezek, Adrienne Dunn, and Rebecca Richards-Kortum. Light scattering from cells : finite-difference time-domain simulations and goniometric measurements. *Applied optics*, 38 16 :3651–61, 1999.

[37] Madeleine S. Durkee, Grace K. Fletcher, Camella Carlson, Kanci Matheson, Sarah K. Swift, Duncan J. Maitland, Jeffrey D. Cirillo, and Kristen C. Maitland. Light scattering by pulmonary alveoli and airway surface liquid using a concentric sphere model. *Opt. Lett.*, 43(20) :5001–5004, Oct 2018.

[38] Pablo Eugui et al. Beyond backscattering : optical neuroimaging by brad. *Biomedical Optics Express*, 9(6) :2476–2494, 2018.

[39] Pablo Eugui, Antonia Lichtenegger, Marco Augustin, Danielle J Harper, Martina Muck, Thomas Roetzer, Andreas Wartak, Thomas Konegger, Georg Widhalm, Christoph K Hitzenberger, Adelheid Woehrer, and Bernhard Baumann. Beyond backscattering : optical neuroimaging by brad. *Biomedical optics express*, 9(6) :2476–2494, 2018.

[40] Pablo Eugui, Conrad Merkle, Danielle J. Harper, Antonia Lichtenegger, Marco Augustin, Martina Muck, Adelheid Wöhrer, Christoph K. Hitzenberger, and Bernhard Baumann. Simultaneous bright and dark field OCT with a polarization sensitive detection (Conference Presentation). In James G. Fujimoto and Joseph A. Izatt, editors, *Optical Coherence Tomography and Coherence Domain Optical Methods in Biomedicine XXIII*, volume 10867. International Society for Optics and Photonics, SPIE, 2019.

[41] Reginald Eze and Sunil Kumar. Laser transport through thin scattering layers. *Applied optics*, 49 :358–68, 01 2010.

[42] Zeinab Sanjabi Eznaveh, Juan Carlos Alvarado Zacarias, Jose Enrique Antonio Lopez, Kai Shi, Giovanni Milione, Yongmin Jung, Benn C. Thomsen, David J. Richardson, Nicolas Fontaine, Sergio G. Leon-Saval, and Rodrigo Amezcua Correa. Photonic lantern broadband orbital angular momentum mode multiplexer. *Opt. Express*, 26(23) :30042–30051, Nov 2018.

[43] Alireza Fardoost, He Wen, Huiyuan Liu, Fatemeh Ghaedi Vanani, and Guifang Li. Optimizing free space to few-modefiber coupling efficiency. *Applied optics*, 58(13) :D34–D38, 2019.

[44] A F Fercher, W Drexler, C K Hitzenberger, and T Lasser. Optical coherence tomography - principles and applications. *Reports on Progress in Physics*, 66(2) :239, jan 2003.

[45] Benjamin A Flusberg, Eric D Cocker, Wibool Piyawattanametha, Juergen C Jung, Eunice LM Cheung, and Mark J Schnitzer. Fiber-optic fluorescence imaging. *Nature methods*, 2(12) :941–950, 2005.

[46] Fabrizio Frezza, Fabio Mangini, and Nicola Tedeschi. Introduction to electromagnetic scattering : tutorial. *JOSA A*, 35(1) :163–173, 2018.

[47] B. Frieden. Laser speckle and related phenomena. *IEEE Journal of Quantum Electronics*, 20(12) :1533–1533, 1984.

[48] Dominic F. G. Gallagher and Thomas P. Felici. Eigenmode expansion methods for simulation of optical propagation in photonics : pros and cons. In Yakov S. Sidorin and Ari Tervonen, editors, *Integrated Optics : Devices, Materials, and Technologies VII*, volume 4987, pages 69 – 82. International Society for Optics and Photonics, SPIE, 2003.

[49] Irene Georgakoudi, Brian C. Jacobson, Jacques Van Dam, Vadim Backman, Michael B. Wallace, Markus G. Müller, Qingguo Zhang, Kamran Badizadegan, Don Sun, Gordon A. Thomas, Lev T. Perelman, and Michael S. Feld. Fluorescence, reflectance, and light-scattering spectroscopy for evaluating dysplasia in patients with barrett's esophagus. *Gastroenterology*, 120(7) :1620 – 1629, 2001.

[50] Antonis Giannopoulos. Modelling ground penetrating radar by gprmax. *Construction and building materials*, 19(10) :755–762, 2005.

[51] Nicolas Godbout and Simon Bolduc Beaudoin. Multi-clad optical fiber with taper portion, and optical fiber device having same. wo patent 2019148276a1, 2019.

[52] Andrew J Gomes, Sarah Ruderman, Mart DelaCruz, Ramesh K Wali, Hemant K Roy, and Vadim Backman. In vivo measurement of the shape of the tissue-refractive-index correlation function and its applicationto detection of colorectal field carcinogenesis. *Journal of biomedical optics*, 17(4) :047005–047005, 2012.

[53] Joseph W Goodman. *Introduction to Fourier optics*. Roberts and Company publishers, 2005.

[54] Frederik Gorlitz, Patrick Hoyer, Henning Falk, Lars Kastrup, Johann Engelhardt, and Stefan W Hell. A sted microscope designed for routine biomedical applications. *Progress In Electromagnetics Research*, 147 :57–68, 2014.

[55] Gérard Gouesbet and Gérard Gréhan. *Generalized lorenz-mie theories*, volume 31. Springer, 2011.

[56] Gaël Guennebaud, Benoît Jacob, et al. Eigen v3. http ://eigen.tuxfamily.org, 2010.

[57] Huiyi Guo, Liang Chen, Zekun Shi, Wenzhe Chang, Letian Gu, Zhi Wang, and Yan-ge Liu. Ultra-low-loss 5-lp mode selective coupler based on fused biconical taper technique. *Optics Express*, 31(11) :18050–18062, 2023.

[58] Dave Hale. Implementing an anisotropic and spatially varying matérn model covariance with smoothing filters. *CWP Report*, 815, 2013.

[59] Martin Hammer, Dietrich Schweitzer, Bernhard Michel, Eike Thamm, and Achim Kolb. Single scattering by red blood cells. *Appl. Opt.*, 37(31) :7410–7418, Nov 1998.

[60] Ian M. Hammond, Alec M. Hammond, and Ryan M. Camacho. Deep learning-enhanced, open-source eigenmode expansion. *Opt. Lett.*, 47(6) :1383–1386, Mar 2022.

[61] Quentin S Hanley, Peter J Verveer, and Thomas M Jovin. Spectral imaging in a programmable array microscope by hadamard transform fluorescence spectroscopy. *Applied spectroscopy*, 53(1) :1–10, 1999.

[62] Charles R. Harris, K. Jarrod Millman, Stéfan J. van der Walt, Ralf Gommers, Pauli Virtanen, David Cournapeau, Eric Wieser, Julian Taylor, Sebastian Berg, Nathaniel J. Smith, Robert Kern, Matti Picus, Stephan Hoyer, Marten H. van Kerkwijk, Matthew Brett, Allan Haldane, Jaime Fernández del Río, Mark Wiebe, Pearu Peterson, Pierre Gérard-Marchant, Kevin Sheppard, Tyler Reddy, Warren Weckesser, Hameer Abbasi, Christoph Gohlke, and Travis E. Oliphant. Array programming with NumPy. *Nature*, 585(7825) :357–362, September 2020.

[63] L. G. Henyey and J. L. Greenstein. Diffuse radiation in the Galaxy. *Astrophys. J.*, 93 :70–83, 1941.

[64] Dora Juan Juan Hu, Linbo Liu, Hui Dong, and Hailiang Zhang. Design of a broadband fiber optic mode coupler for multimode optical coherence tomography. In *Photonics*, volume 10, page 162. MDPI, 2023.

[65] Xiaobo Hu, Meng-Xuan Dong, Zhi-Han Zhu, Wei Gao, and Carmelo Rosales-Guzmán. Does the structure of light influence the speckle size ? *Scientific Reports*, 10, 01 2020.

[66] Bin Huang, Nicolas K Fontaine, Roland Ryf, Binbin Guan, Sergio G Leon-Saval, R Shubochkin, Y Sun, R Lingle, and Guifang Li. All-fiber mode-group-selective photonic lantern using graded-index multimode fibers. *Optics express*, 23(1) :224–234, 2015.

[67] Bin Huang, Nicolas K. Fontaine, Roland Ryf, Binbin Guan, Sergio G. Leon-Saval, R. Shubochkin, Y. Sun, R. Lingle, and Guifang Li. All-fiber mode-group-selective photonic lantern using graded-index multimode fibers. *Opt. Express*, 23(1) :224–234, Jan 2015.

[68] D Huang et al. Optical coherence tomography. *Science*, 254(5035) :1178–1181, 1991.

[69] Hendrik Christoffel Hulst and Hendrik C van de Hulst. *Light scattering by small particles*. Courier Corporation, 1981.

[70] Irving Itzkan, Le Qiu, Hui Fang, Munir M. Zaman, Edward Vitkin, Ionita C. Ghiran, Saira Salahuddin, Mark Modell, Charlotte Andersson, Lauren M. Kimerer, Patsy B. Cipolloni, Kee-Hak Lim, Steven D. Freedman, Irving Bigio, Benjamin P. Sachs, Eugene B. Hanlon, and Lev T. Perelman. Confocal light absorption and scattering spectroscopic microscopy monitors organelles in live cells with no exogenous labels. *Proceedings of the National Academy of Sciences*, 104(44) :17255–17260, 2007.

[71] Steven L Jacques. Optical properties of biological tissues : a review. *Physics in Medicine and Biology*, 58(11) :R37–R61, May 2013.

[72] Steven L Jacques, Jessica C Ramella-Roman, and Kenneth Lee. Imaging skin pathology with polarized light. *Journal of biomedical optics*, 7(3) :329–340, 2002.

[73] Wenzel Jakob, Jason Rhinelander, and Dean Moldovan. pybind11–seamless operability between c++ 11 and python. *URL : https ://github. com/pybind/pybind11*, 2017.

[74] Ik-Kyung Jang, Guillermo Tearney, Briain MacNeill, Masamichi Takano, Fabian Moselewski, Nicusor Iftimia, Milen Shishkov, Stuart Houser, Hans Aretz, Elkan Halpern, and Brett Bouma. In vivo characterization of coronary atherosclerotic plaque by use of optical coherence tomography. *Circulation*, 111 :1551–5, 03 2005.

[75] Cesar Jauregui, Jens Limpert, and Andreas Tünnermann. High-power fibre lasers. *Nature photonics*, 7(11) :861–867, 2013.

[76] Wenjie Jiang, Xianye Li, Xinglei Peng, and Baoqing Sun. Imaging high-speed moving targets with a single-pixel detector. *Optics Express*, 28(6) :7889–7897, 2020.

[77] Keiji Kataoka. Estimation of coupling efficiency of optical fiber by far-field method. *Optical Review - OPT REV*, 17 :476–480, 09 2010.

[78] Hwanmun Kim, Hossein Dehghani, Iman Ahmadabadi, Ivar Martin, and Mohammad Hafezi. Floquet vortex states induced by light carrying an orbital angular momentum. *Physical Review B*, 105(8) :L081301, 2022.

[79] Jeehyun Kim, Eunha K. Kim, Donald T. Miller, and Thomas E. Milner. Speckle reduction in OCT with multimode source fiber. In Israel Gannot, editor, *Optical Fibers and Sensors for Medical Applications IV*, volume 5317, pages 246 – 250. International Society for Optics and Photonics, SPIE, 2004.

[80] Y. Koike and K. Koike. 8.11 - optical fibers. In Krzysztof Matyjaszewski and Martin Möller, editors, *Polymer Science : A Comprehensive Reference*, pages 283–304. Elsevier, Amsterdam, 2012.

[81] Alexander Kokhanovsky. Volume 4 : Light scattering and radiative transfer. In Alexander A. Kokhanovsky, editor, *Springer Series in Light Scattering*. Springer, 2019.

[82] Moritz Kreysing, Dino Ott, Michael J Schmidberger, Oliver Otto, Mirjam Schürmann, Estela Martín-Badosa, Graeme Whyte, and Jochen Guck. Dynamic operation of optical fibres beyond the single-mode regime facilitates the orientation of biological cells. *Nature communications*, 5(1) :1–6, 2014.

[83] Suzanne Lacroix, Francois Gonthier, and Jacques Bures. Modeling of symmetric 2× 2 fused-fiber couplers. *Applied optics*, 33(36) :8361–8369, 1994.

[84] B Lamouroux and B Prade. Three-dimensional beam-propagation-method treatment of a monomode optical-fiber half-coupler. *JOSA A*, 4(12) :2228–2232, 1987.

[85] Boris Lande and Wayne Mitzner. Analysis of lung parenchyma as a parametric porous medium. *Journal of Applied Physiology*, 101(3) :926–933, 2006.

[86] Philip Laven. Mieplot (a computer program for scattering of light from a sphere using mie theory & the debye series). *http ://www. philiplaven. com/mieplot. htm*, 2011.

[87] Richard B Lehoucq, Danny C Sorensen, and Chao Yang. *ARPACK users' guide : solution of large-scale eigenvalue problems with implicitly restarted Arnoldi methods*. SIAM, 1998.

[88] R. Leitgeb, C. K. Hitzenberger, and A. F. Fercher. Performance of fourier domain vs. time domain optical coherence tomography. *Opt. Express*, 11(8) :889–894, Apr 2003.

[89] R. Leitgeb, M. Wojtkowski, A. Kowalczyk, C. K. Hitzenberger, M. Sticker, and A. F. Fercher. Spectral measurement of absorption by spectroscopic frequency-domain optical coherence tomography. *Opt. Lett.*, 25(11) :820–822, June 2000.

[90] Sergio G. Leon-Saval, Alexander Argyros, and Joss Bland-Hawthorn. Photonic lanterns : a study of light propagation in multimode to single-mode converters. *Opt. Express*, 18(8) :8430–8439, Apr 2010.

[91] Sergio G Leon-Saval, Alexander Argyros, and Joss Bland-Hawthorn. Photonic lanterns. *Nanophotonics*, 2(5-6) :429–440, 2013.

[92] Sergio G. Leon-Saval, Nicolas K. Fontaine, and Rodrigo Amezcua-Correa. Photonic lantern as mode multiplexer for multimode optical communications. *Optical Fiber Technology*, 35 :46–55, 2017. Next Generation Multiplexing Schemes in Fiber-based Systems.

[93] Wei Li, Ksenia Abrashitova, and Lyubov V. Amitonova. Super-resolution multimode fiber imaging with an untrained neural network. *Opt. Lett.*, 48(13) :3363–3366, Jul 2023.

[94] Bingyang Liang, Fei Shen, Shao meng Wang, Yuanguo Zhou, Yang Yang, Kaiyang Cheng, Guangmin Zhang, Yu Zheng, Qing Huo Liu, and Yubin Gong. Reconstruction of three-dimensional objects in layered composite structures from multimode orbital angular momentum. *Physical Review E*, 105(2) :025302, 2022.

[95] Zhiyu Liao, Faris Sinjab, Hany M Elsheikha, and Ioan Notingher. Optical sectioning in multifoci raman hyperspectral imaging. *Journal of Raman Spectroscopy*, 49(10) :1660–1667, 2018.

[96] Joonoh Lim, Huafeng Ding, Mustafa Mir, Ruoyu Zhu, Krishnarao Tangella, and Gabriel Popescu. Born approximation model for light scattering by red blood cells. *Biomedical optics express*, 2(10) :2784–2791, 2011.

[97] SC Lim and Lee P Teo. Generalized whittle–matérn random field as a model of correlated fluctuations. *Journal of Physics A : Mathematical and Theoretical*, 42(10) :105202, 2009.

[98] Finn Lindgren, David Bolin, and Håvard Rue. The spde approach for gaussian and non-gaussian fields : 10 years and still running. *Spatial Statistics*, 50 :100599, 2022.

[99] Di Liu, Chuanbin Ge, Yi Xin, Qin Li, and Ran Tao. Dispersion correction for optical coherence tomography by the stepped detection algorithm in the fractional fourier domain. *Optics express*, 28(5) :5919–5935, 2020.

[100] Q. H. Liu. The pseudospectral time-domain (pstd) method : a new algorithm for solutions of maxwell's equations. In *IEEE Antennas and Propagation Society International Symposium 1997. Digest*, volume 1, pages 122–125 vol.1, 1997.

[101] JD Love, WM Henry, WJ Stewart, RJ Black, S Lacroix, and F Gonthier. Tapered single-mode fibres and devices. part 1 : Adiabaticity criteria. *IEE Proceedings J (Optoelectronics)*, 138(5) :343–354, 1991.

[102] IK Ludlow and J Everitt. Inverse mie problem. *JOSA A*, 17(12) :2229–2235, 2000.

[103] FDTD Lumerical. Solutions, 2016.

[104] Alois Mair, Alipasha Vaziri, Gregor Weihs, and Anton Zeilinger. Entanglement of the orbital angular momentum states of photons. *Nature*, 412(6844) :313–316, 2001.

[105] Shampy Mansha, Parikshit Moitra, Xuewu Xu, Tobias WW Mass, Rasna Maruthiyodan Veetil, Xinan Liang, Shi-Qiang Li, Ramón Paniagua-Domínguez, and Arseniy I Kuznetsov. High resolution multispectral spatial light modulators based on tunable fabry-perot nanocavities. *Light : Science & Applications*, 11(1) :141, 2022.

[106] Christian Maurer, Alexander Jesacher, Stefan Bernet, and Monika Ritsch-Marte. What spatial light modulators can do for optical microscopy. *Laser & Photonics Reviews*, 5(1) :81–101, 2011.

[107] Katherine M McKinnon. Flow cytometry : an overview. *Current protocols in immunology*, 120(1) :5–1, 2018.

[108] Nizan Meitav, E. Ribak, and Shy Shoham. Point spread function estimation from projected speckle illumination. *Light : Science & Applications*, 5 :e16048, 03 2016.

[109] Dirk Merkel. Docker : lightweight linux containers for consistent development and deployment. *Linux journal*, 2014(239) :2, 2014.

[110] Gustav Mie. Beiträge zur optik trüber medien, speziell kolloidaler metallösungen. *Annalen der physik*, 330(3) :377–445, 1908.

[111] Gustav Mie. Beiträge zur optik trüber medien, speziell kolloidaler metallösungen. *Annalen der physik*, 330(3) :377–445, 1908.

[112] K Jarrod Millman and Michael Aivazis. Python for scientists and engineers. *Computing in Science & Engineering*, 13(2) :9–12, 2011.

[113] Michael I Mishchenko, Larry D Travis, and Andrew A Lacis. *Scattering, absorption, and emission of light by small particles*. Cambridge university press, 2002.

[114] John A Nelder and Roger Mead. A simplex method for function minimization. *The computer journal*, 7(4) :308–313, 1965.

[115] Antonio Alvaro Ranha Neves and Dario Pisignano. Effect of finite terms on the truncation error of mie series. *Optics letters*, 37(12) :2418–2420, 2012.

[116] Danny Noordegraaf, Peter M. W. Skovgaard, Martin D. Nielsen, and Joss Bland-Hawthorn. Efficient multi-mode to single-mode coupling in a photonic lantern. *Opt. Express*, 17(3) :1988–1994, Feb 2009.

[117] Travis E. Oliphant. Python for scientific computing. *Computing in Science Engineering*, 9(3) :10–20, 2007.

[118] Ying Pan, Jens-Peter Volkmer, Kathleen E Mach, Robert V Rouse, Jen-Jane Liu, Debashis Sahoo, Timothy C Chang, Thomas J Metzner, Lei Kang, Matt Van De Rijn, et al. Endoscopic molecular imaging of human bladder cancer using a cd47 antibody. *Science translational medicine*, 6(260) :260ra148–260ra148, 2014.

[119] Ovidio Peña-Rodríguez, Pedro Pablo González Pérez, and Umapada Pal. Mielab : a software tool to perform calculations on the scattering of electromagnetic waves by multilayered spheres. *International Journal of Spectroscopy*, 2011, 2011.

[120] Martin Plöschner, Tomáš Tyc, and Tomáš Čižmár. Seeing through chaos in multimode fibres. *Nature Photonics*, 9(8) :529–535, 2015.

[121] Martin Poinsinet de Sivry-Houle. DataVisual : A python tool for high-dimensionality dataset visualization. `https://pypi.org/project/DataVisual/`, 2021.

[122] Martin Poinsinet de Sivry-Houle. MartinPdeS/PyMieSim : First release of Mie Scattering simulation software PyMieSim. https://doi.org/10.5281/zenodo.4556074, February 2021.

[123] Martin Poinsinet de Sivry-Houle, Pierre-Alexandre Aube, Nicolas Godbout, and Caroline Boudoux. Pymiesim : an open source library for fast and flexible light scattering simulations. In *Optical Interactions with Tissue and Cells XXXIII ; and Advanced Photonics in Urology*, page PC1195802. SPIE, 2022.

[124] Martin Poinsinet de Sivry-Houle and Pierre-Alexandre Aubé. PyOptik : A python package for material refractive index library. https://pypi.org/project/PyOptik/, 2021.

[125] Martin Poinsinet de Sivry-Houle, Simon Bolduc Beaudoin, Simon Brais-Brunet, Mathieu Dehaes, Nicolas Godbout, and Caroline Boudoux. All-fiber few-mode optical coherence tomography using a modally-specific photonic lantern. *Biomedical Optics Express*, 12(9) :5704–5719, 2021.

[126] Martin Poinsinet de Sivry-Houle and Caroline Boudoux. Martinpdes/pymiesim : Pymiesim beta. https://github.com/MartinPdeS/PyMieSim, 12 2022.

[127] Mikhail N. Polyanskiy. Refractive index database.

[128] Richard Potton. Reciprocity in optics. *Rep. Prog. Phys.*, 67 :717–754, 05 2004.

[129] Scott Prahl. Miepython.

[130] Juncheng Qiu and Jianqi Shen. Beam shape coefficient calculation for a gaussian beam : localized approximation, quadrature and angular spectrum decomposition methods. *Applied optics*, 57(2) :302–313, 2018.

[131] Jörg Reitterer. *Numerical analysis of optical multi-core waveguides*. PhD thesis, 2010.

[132] David J Richardson, John M Fini, and Lynn E Nelson. Space-division multiplexing in optical fibres. *Nature photonics*, 7(5) :354–362, 2013.

[133] Jeremy D Rogers, İlker R Çapoğlu, and Vadim Backman. Nonscalar elastic light scattering from continuous random media in the born approximation. *Optics letters*, 34(12) :1891–1893, 2009.

[134] Oleg Romanov, Alexei Tolstik, Noé Ortega-Quijano, Felix Fanjul-Velez, and Jose Arce-Diego. Finite-difference time-domain simulation of light propagation in 2d scattering media. *Nonlinear Phenomena in Complex Systems*, 12 :267 – 274, 01 2009.

[135] Elena A Romanova. Scalar approximation feasibility analysis near the cutoff frequency of he1n fibre mode with account of material losses. *Optics communications*, 208(1-3) :91–96, 2002.

[136] Philip J Rosenfeld. Optical coherence tomography and the development of antiangiogenic therapies in neovascular age-related macular degeneration. *Investigative ophthalmology & visual science*, 57(9) :OCT14–OCT26, 2016.

[137] Stefan Rothe, Karl-Ludwig Besser, David Krause, Robert Kuschmierz, Nektarios Koukourakis, Eduard Jorswieck, and Jürgen W Czarske. Securing data in multimode fibers by exploiting mode-dependent light propagation effects. *Research*, 6 :0065, 2023.

[138] Ernest Rutherford. Lxxix. the scattering of $\alpha$ and $\beta$ particles by matter and the structure of the atom. *The London, Edinburgh, and Dublin Philosophical Magazine and Journal of Science*, 21(125) :669–688, 1911.

[139] Christian Schwab, Sergio G Leon-Saval, Christopher H Betters, Joss Bland-Hawthorn, and Suvrath Mahadevan. Single mode, extreme precision doppler spectrographs. *Proceedings of the International Astronomical Union*, 8(S293) :403–406, 2012.

[140] Subodh Kumar Sharma. *A review of approximate analytic light-scattering phase functions*, pages 53–100. Springer Berlin Heidelberg, Berlin, Heidelberg, 2015.

[141] Subodh Kumar Sharma. *Elastic scattering of electromagnetic radiation : Analytic solutions in diverse backgrounds*. CRC Press, 02 2018.

[142] Li Shen, Lin Gan, Chen Yang, Weijun Tong, Songnian Fu, Deming Liu, and Ming Tang. Highly mode selective 3-mode photonic lantern through geometric optimization. In *Optical Fiber Communication Conference*, page W2A.14. Optica Publishing Group, 2018.

[143] Bruce W. Smith, Donis G. Flagello, Joseph R. Summa, and Lynn F. Fuller. Comparison of scalar and vector diffraction modeling for deep-UV lithography. In John D. Cuthbert, editor, *Optical/Laser Microlithography*, volume 1927, pages 847 – 857. International Society for Optics and Photonics, SPIE, 1993.

[144] A .W. Snyder and J. Love. *Optical Waveguide Theory*. Springer, 1 edition, 1983.

[145] Zachary A Steelman, Derek S Ho, Kengyeh K Chu, and Adam Wax. Light-scattering methods for tissue diagnosis. *Optica*, 6(4) :479–489, 2019.

[146] Daan Stellinga, David B Phillips, Simon Peter Mekhail, Adam Selyem, Sergey Turtaev, Tomáš Čižmár, and Miles J Padgett. Time-of-flight 3d imaging through multimode optical fibers. *Science*, 374(6573) :1395–1399, 2021.

[147] John William Strutt. *On the Light from the Sky, its Polarization and Colour*, volume 1 of *Cambridge Library Collection - Mathematics*, page 87–103. Cambridge University Press, 2009.

[148] Benjamin J Sumlin, William R Heinson, and Rajan K Chakrabarty. Retrieving the aerosol complex refractive index using pymiescatt : A mie computational package with visualization capabilities. *Journal of Quantitative Spectroscopy and Radiative Transfer*, 205 :127–134, 2018.

[149] Benjamin J. Sumlin, William R. Heinson, and Rajan K. Chakrabarty. Retrieving the aerosol complex refractive index using pymiescatt : A mie computational package with visualization capabilities. *Journal of Quantitative Spectroscopy and Radiative Transfer*, 205 :127–134, January 2018.

[150] Wenbo Sun, Norman G Loeb, and Bing Lin. Light scattering by an infinite circular cylinder immersed in an absorbing medium. *Applied optics*, 44(12) :2338–2342, 2005.

[151] Richard Swinbank and R James Purser. Fibonacci grids : A novel approach to global modelling. *Quarterly Journal of the Royal Meteorological Society : A journal of the atmospheric sciences, applied meteorology and physical oceanography*, 132(619) :1769–1793, 2006.

[152] Tatsuki Tahara, Xiangyu Quan, Reo Otani, Yasuhiro Takaki, and Osamu Matoba. Digital holography and its multidimensional imaging applications : a review. *Microscopy*, 67(2) :55–67, 2018.

[153] A Timothy, W Li Youwei, et al. The shape of fiber tapers. *J. Lightwave Technol*, 10 :432, 1992.

[154] Ling-Hsuan Tsai, Po Nien Yang, Chung-Chih Wu, and Hoang Yan Lin. Quantifying scattering coefficient for multiple scattering effect by combining optical coherence tomography with finite-difference time-domain simulation method. *Journal of Biomedical Optics*, 23(8) :1 – 9, 2018.

[155] Vladimir Turzhitsky, Le Qiu, Irving Itzkan, Andrei A Novikov, Mikhail S Kotelev, Michael Getmanskiy, Vladimir A Vinokurov, Alexander V Muradov, and Lev T Perelman. Spectroscopy of scattered light for the characterization of micro and nanoscale objects in biology and medicine. *Applied spectroscopy*, 68(2) :133–154, 2014.

[156] Edwin van der Pol, Leonie de Rond, Frank AW Coumans, Elmar L Gool, Anita N Böing, Auguste Sturk, Rienk Nieuwland, and Ton G van Leeuwen. Absolute sizing and label-free identification of extracellular vesicles by flow cytometry. *Nanomedicine : Nanotechnology, Biology and Medicine*, 14(3) :801–810, 2018.

[157] Edwin van der Pol, Leonie de Rond, Frank AW Coumans, Elmar L Gool, Anita N Böing, Auguste Sturk, Rienk Nieuwland, and Ton G van Leeuwen. Absolute sizing and label-free identification of extracellular vesicles by flow cytometry. *Nanomedicine : Nanotechnology, Biology and Medicine*, 14(3) :801–810, 2018.

[158] Guido Van Rossum and Fred L Drake Jr. *Python tutorial*. Centrum voor Wiskunde en Informatica Amsterdam, The Netherlands, 1995.

[159] MR Rashidian Vaziri, A Omidvar, B Jaleh, and N Partovi Shabestari. Investigating the extrinsic size effect of palladium and gold spherical nanoparticles. *Optical Materials*, 64 :413–420, 2017.

[160] Amado M Velázquez-Benítez, J Enrique Antonio-López, Juan C Alvarado-Zacarías, Nicolas K Fontaine, Roland Ryf, Haoshuo Chen, Juan Hernández-Cordero, Pierre Sillard, Chigo Okonkwo, Sergio G Leon-Saval, et al. Scaling photonic lanterns for space-division multiplexing. *Scientific reports*, 8(1) :8897, 2018.

[161] Amado M Velázquez-Benítez, J Enrique Antonio-López, Juan C Alvarado-Zacarías, Nicolas K Fontaine, Roland Ryf, Haoshuo Chen, Juan Hernández-Cordero, Pierre Sillard, Chigo Okonkwo, Sergio G Leon-Saval, et al. Scaling photonic lanterns for space-division multiplexing. *Scientific reports*, 8(1) :8897, 2018.

[162] Amado M. Velázquez-Benítez, K. Yanín Guerra-Santillán, Raúl Caudillo-Viurquez, J. Enrique Antonio-López, Rodrigo Amezcua-Correa, and Juan Hernández-Cordero. Optical trapping and micromanipulation with a photonic lantern-mode multiplexer. *Opt. Lett.*, 43(6) :1303–1306, Mar 2018.

[163] Luwei Wang, Wei Yan, Runze Li, Xiaoyu Weng, Jia Zhang, Zhigang Yang, Liwei Liu, Tong Ye, and Junle Qu. Aberration correction for improving the image quality in sted microscopy using the genetic algorithm. *Nanophotonics*, 7(12) :1971–1980, 2018.

[164] Yan Wang and Li Bai. Accurate monte carlo simulation of frequency-domain optical coherence tomography. *International Journal for Numerical Methods in Biomedical Engineering*, 35(4) :e3177, 2019.

[165] Peter Whittle. On stationary processes in the plane. *Biometrika*, pages 434–449, 1954.

[166] Warren J Wiscombe. Improved mie scattering algorithms. *Applied optics*, 19(9) :1505–1509, 1980.

[167] Feng Xu, Kuanfang Ren, Gérard Gouesbet, Gérard Gréhan, and Xiaoshu Cai. Generalized lorenz-mie theory for an arbitrarily oriented, located, and shaped beam scattered by a homogeneous spheroid. *JOSA A*, 24(1) :119–131, 2007.

[168] Ji Yi and Vadim Backman. Imaging a full set of optical scattering properties of biological tissue by inverse spectroscopic optical coherence tomography. *Opt. Lett.*, 37(21) :4443–4445, November 2012.

[169] Ji Yi and Vadim Backman. Imaging a full set of optical scattering properties of biological tissue by inverse spectroscopic optical coherence tomography. *Optics letters*, 37(21) :4443–4445, 2012.

[170] Qian Zhao, Ji Zhou, Fuli Zhang, and Didier Lippens. Mie resonance-based dielectric metamaterials. *Materials today*, 12(12) :60–69, 2009.

[171] Xiaoping ZHENG and HUA Nan. Review and outlook of 30 years of optical network development. *Telecommunications Science*, 32(5) :24, 2016.

# APPENDIX A SCIENTIFIC CONTRIBUTION

**Peer-reviewed scientific articles**

* **Martin Poinsinet de Sivry-Houle**, *et al.* "SuPyMode : An open-source library for design and optimization of fiber optic components". Opt. Continuum 3, 242-255 (2024)
* **Martin Poinsinet de Sivry-Houle**, *et al.* (2023). PyMieSim : an open-source library for fast and flexible far-field Mie scattering simulations. Optics Continuum, 2(3), 520-534.
* **Martin Poinsinet de Sivry-Houle**, *et al.* (2021). All-fiber few-mode optical coherence tomography using a modally-specific photonic lantern. Biomedical Optics Express, 12(9), 5704-5719.
* Xavier Attendu, Marie Hélène Bourget, **Martin Poinsinet de Sivry-Houle**, and Caroline Boudoux (2019). "Coregistered optical coherence tomography and frequency encoded multispectral imaging for spectrally sparse color imaging." Journal of Biomedical Optics vol. 25, no. 3.

**Oral presentation**

* **Poinsinet de Sivry-Houle, Martin**, *et al.* "PyMieSim : simulating incoherent and coherent detection of light scattering". SPIE BIOS, San Francisco, CA, USA [Jan. 2024]
* **Poinsinet de Sivry-Houle, Martin**, *et al.* "SuPyMode : an open-source Python library for design and optimization of fiber couplers". Physics and Simulation of Optoelectronic Devices XXXI, San Francisco, CA, USA [Jan. 2023]
* **Poinsinet de Sivry-Houle, Martin**, *et al.* "PyMieSim : an open-source library for fast and flexible light scattering simulations". Optical Interactions with Tissue and Cells XXXIII ; and Advanced Photonics in Urology ;, San Francisco, CA, USA [Jan. 2021]
* **Martin Poinsinet de Sivry-Houle**, Simon Bolduc *et al.* "All-fiber few-mode OCT using a photonic lantern". Proc. SPIE10487, Optical Coherence Tomography and Coherence Domain Optical Methods in Biomedecine XXIV, 11228-9, San Francisco, CA, USA [Jan. 2020]

**Poster presentation**

* **Martin Poinsinet de Sivry-Houle**, *et al.* "PyMieSim : An open-source library for fast and flexible light scattering simulations.". Optica Biophotonics Congress : Optics in the Life Sciences, Vancouver, British Columbia, Canada [March 2023].

* **Martin Poinsinet de Sivry-Houle**, *et al.* "Design of Photonic lanterns component using SuPyMode, an open-sourced Python library.". Optics and Photonics in Medicine and Biology Gordon Research Seminar, Bates College in Lewiston, Maine, United States [July 2022].
* **Martin Poinsinet de Sivry-Houle**, *et al.* "PyMieSim : An open-source library for fast and flexible light scattering simulations.". Presentation for innovation day Montreal (SPIE/OSA), Montréal, QC, Canada. [Sept. 2021].
* Xavier Attendu, **Martin Poinsinet de Sivry-Houle**, *et al.* "Color OCT : Combined Optical Coherence Tomography and Multispectral Reflectance Imaging". Poster session presented at Star-A-Com, Montréal, QC, Canada. [jan. 2020].
* Xavier Attendu, **Martin Poinsinet de Sivry-Houle**, *et al.* "Color OCT : Combined Optical Coherence Tomography and Multispectral Reflectance Imaging". Poster session presented at SPIE Photonics West, San Francisco, CA, USA [sep. 2018].
* Xavier Attendu, **Martin Poinsinet de Sivry-Houle**, *et al.* (2018, September). "Color OCT : Combined Optical Coherence Tomography and Multispectral Reflectance Imaging". Poster session presented at SPIE Photonics North, Quebec City, Qc, Canada.

**Patent**

* **Martin Poinsinet de Sivry-Houle**, Caroline Boudoux, Lucien Weiss, Rodrigo Bercerra, Guillaume Ramadier. "Illumination device for super-resolution microscopy". DIV-1009 [Provisional patent # 63/618,495]
* **Martin Poinsinet de Sivry-Houle**, Nicolas Godbout, Caroline Boudoux, Simon Bolduc Beaudoin. "All-fiber multimodal interferometer for imaging technique". DIV-855 [accepted jan. 2020]

**Open-source software**

* SuPyMode `https://github.com/MartinPdeS/SuPyMode`
* PyMieSim `https://github.com/MartinPdeS/PyMieSim`
* FiberFusing `https://github.com/MartinPdeS/FiberFusing`
* PyFinitDiff `https://github.com/MartinPdeS/PyFinitDiff`
* PyFiberModes `https://github.com/MartinPdeS/PyFiberModes`

# APPENDIX B PROOF # 1 : PROPERTY OF THE FOURIER TRANSFORM OVER LAPLACIAN OPERATOR

Starting with the inverse Fourier transform of a generic function, $f(\boldsymbol{r})$ to which we apply the Laplacian operator.

$$f(\boldsymbol{r}) = \mathscr{F}^{-1}\left\{\tilde{f}(\boldsymbol{k})\right\}$$

$$f(\boldsymbol{r}) = \frac{1}{2\pi}\int_{\mathbb{R}^3} d\boldsymbol{k}\tilde{f}(\boldsymbol{k})e^{i\boldsymbol{k}\cdot\boldsymbol{r}}$$

$$(a+\Delta)f(\boldsymbol{r}) = \frac{1}{2\pi}\int_{\mathbb{R}^3} d\boldsymbol{k}(a+\Delta)\tilde{f}(\boldsymbol{k})e^{i\boldsymbol{k}\cdot\boldsymbol{r}}$$

$$(a+\Delta)f(\boldsymbol{r}) = \frac{1}{2\pi}\int_{\mathbb{R}^3} d\boldsymbol{k}\tilde{f}(\boldsymbol{k})(a+\Delta)e^{i\boldsymbol{k}\cdot\boldsymbol{r}}$$

$$(a+\Delta)f(\boldsymbol{r}) = \frac{1}{2\pi}\int_{\mathbb{R}^3} d\boldsymbol{k}\tilde{f}(\boldsymbol{k})\left(a-\|\boldsymbol{k}\|^2\right)e^{i\boldsymbol{k}\cdot\boldsymbol{r}}$$

$$(a+\Delta)f(\boldsymbol{r}) = (a-\|\boldsymbol{k}\|^2)\frac{1}{2\pi}\int_{\mathbb{R}^3} d\boldsymbol{k}\tilde{f}(\boldsymbol{k})e^{i\boldsymbol{k}\cdot\boldsymbol{r}}$$

$$(a+\Delta)^2 f(\boldsymbol{r}) = (a+\Delta)(a-\|\boldsymbol{k}\|^2)\frac{1}{2\pi}\int_{\mathbb{R}^3} d\boldsymbol{k}\tilde{f}(\boldsymbol{k})e^{i\boldsymbol{k}\cdot\boldsymbol{r}}$$

$$(a+\Delta)^2 f(\boldsymbol{r}) = (a-\|\boldsymbol{k}\|^2)(a+\Delta)\left[\frac{1}{2\pi}\int_{\mathbb{R}^3} d\boldsymbol{k}\tilde{f}(\boldsymbol{k})e^{i\boldsymbol{k}\cdot\boldsymbol{r}}\right]$$

$$(a+\Delta)^2 f(\boldsymbol{r}) = (a-\|\boldsymbol{k}\|^2)^2\mathscr{F}^{-1}\left\{\tilde{f}(\boldsymbol{k})\right\}$$

Thus, we can generalize this to the $n^{th}$ order :

$$(a+\Delta)^n f(\boldsymbol{r}) = (a-\|\boldsymbol{k}\|^2)^n\mathscr{F}^{-1}\left\{\tilde{f}(\boldsymbol{k})\right\}$$

# APPENDIX C DERIVATION OF THE ADIABATIC CRITERION

In this section, we derive the equations leading to the formulation of the adiabatic criterion as it is employed by the SuPyMode library to assess the different designs of fiber optics components. In the scalar approximation, the mode coupling is commonly defined as

$$C_{ij} = \frac{\pi k^2}{\Delta\beta_{ij}\sqrt{\beta_i\beta_j}} \int_A \hat{\psi}_i(r,\theta)\, \hat{\psi}_j(r,\theta) \frac{\partial}{\partial z} n^2(z,r,\theta)\, r\, \mathrm{d}r\mathrm{d}\theta \quad , \tag{C.1}$$

where $\mathrm{C}_{ij}$ is the coupling between the modes $i$ and $j$, $\hat{\psi}_i$ and $\beta_i$ are respectively the L2-normalized mode field and propagation constant of the mode $i$, [24] and $\Delta\beta_{ij} = \beta_i - \beta_j$ is the difference between the propagation constants of the two modes. In the equation above, $k$ is the wavenumber, $n(z,r,\theta)$ is the refractive index, and $(z,r,\theta)$ are the cylindrical coordinates with longitudinal propagation in direction $z$.
However, for homothetic transformations of the structure refractive index profile, we have the relation

$$n(z,r,\theta) = n[z_0, a(z)r, \theta]\,, \tag{C.2}$$

where we have assumed that the fiber is untapered at $z = z_0$. We have also defined the taper ratio

$$a = \frac{\rho_0}{\rho}, \tag{C.3}$$

where $\rho_0 = \rho(z_0)$ is the distance from the center of the homotety to an arbitrary point on the original, untapered structure, and $\rho$ is the distance between the same points on the homothetically tapered structure. Hence, $\rho$ and $\rho_0$ are not absolute quantities, and only their ratio is significant. A widely used metric is the inverse taper ratio (ITR), defined at any given longitudinal position as

$$\mathrm{ITR} = \frac{1}{a} = \frac{\rho}{\rho_0}. \tag{C.4}$$

Using that result, we can rewrite the derivative of $n^2$ with respect to $z$ as shown in Eq. C.5.

$$\begin{aligned}\frac{\partial n^2}{\partial z} &= \frac{\partial n^2(z_0, ar, \theta)}{\partial z} \\ &= \frac{\partial n^2(z_0, ar, \theta)}{\partial ar}\frac{\partial ar}{\partial z} + \frac{\partial n^2(z_0, ar, \theta)}{\partial \theta}\underbrace{\frac{\partial \theta}{\partial z}}_{0} \\ &= \frac{\partial n^2(z_0, ar, \theta)}{\partial ar}\left(r\,\frac{\partial a}{\partial z} + a\,\underbrace{\frac{\partial r}{\partial z}}_{0}\right) \\ &= r\,\frac{\partial n^2(z_0, ar, \theta)}{\partial ar}\,\frac{\partial a}{\partial z}.\end{aligned} \tag{C.5}$$

Inserting Eq.C.5 in Eq.C.1, we get

$$\begin{aligned}C_{ij} &= \frac{\pi k^2}{\Delta\beta_{ij}\sqrt{\beta_i\beta_j}}\int_A \hat{\psi}_i(r,\theta)\,\hat{\psi}_j(r,\theta)\,\frac{\partial n^2(z_0, ar, \theta)}{\partial ar}\frac{\partial a}{\partial z}\,r^2\,\mathrm{d}r\,\mathrm{d}\theta \\ &= \frac{\pi k^2}{\Delta\beta_{ij}\sqrt{\beta_i\beta_j}}\left(\frac{1}{a}\frac{\partial a}{\partial z}\right)\int_A \hat{\psi}_i(r,\theta)\,\hat{\psi}_j(r,\theta)\,\frac{\partial n^2(z_0, ar, \theta)}{\partial r}\,r^2\,\mathrm{d}r\,\mathrm{d}\theta \\ &= \frac{-\pi k^2}{\Delta\beta_{ij}\sqrt{\beta_i\beta_j}}\left(\frac{1}{\rho}\frac{\partial \rho}{\partial z}\right)\int_A \hat{\psi}_i(r,\theta)\,\hat{\psi}_j(r,\theta)\,\frac{\partial n^2(z_0, ar, \theta)}{\partial r}\,r^2\,\mathrm{d}r\,\mathrm{d}\theta.\end{aligned} \tag{C.6}$$

It is important to note that it is the logarithmic differential $\mathrm{d}\rho/\rho$ that appears naturally in this formula. As noted above, the absolute differential $\mathrm{d}\rho$ is indeed not physically relevant, given the relative nature of the length scale $\rho$.

From Eq. C.6 we can define the normalized coupling coefficient as

$$\begin{aligned}\tilde{C}_{ij}(a) &= C_{ij}\left(\frac{1}{\rho}\frac{\partial \rho}{\partial z}\right)^{-1} \\ &= \frac{-\pi k^2}{\Delta\beta_{ij}\sqrt{\beta_i\beta_j}}\int_A \hat{\psi}_i(r,\theta)\,\hat{\psi}_j(r,\theta)\,\frac{\partial n^2(0, ar, \theta)}{\partial r}\,r^2\,\mathrm{d}r\,\mathrm{d}\theta,\end{aligned} \tag{C.7}$$

which does not depend on the longitudinal profile of the coupler.

# APPENDIX D MODE COUPLING : ANALYTICAL SOLUTION

For circular symmetric structures composed of n interfaces, analytical solution for the mode coupling can be derived in the form

$$\bar{C}_{ij}(z) = \frac{1}{2}\frac{k^2}{\Delta\beta_{ij}\sqrt{\beta_i\beta_j}}\sum_{m=1}^{n}\left[\rho_i^2(n_{m-}^2 - n_{m+}^2)\hat{\Psi}_i(\rho_m)\hat{\Psi}_j(\rho_m)\right], \tag{D.1}$$

where the index $m$ represents the structure circular interfaces, $m-$ and $m+$ are associated to the interior and exterior part of the interface, respectively and $\rho_m$ is the radius of the $m$-th interface [24]. As such, for a single-clad fiber, which comprises two interfaces, the equation becomes

$$\bar{C}_{ij}(z) = \frac{1}{2}\frac{k^2}{\Delta\beta_{ij}\sqrt{\beta_i\beta_j}}\left[\rho_c^2(n_c^2 - n_g^2)\hat{\Psi}_i(\rho_c)\hat{\Psi}_j(\rho_c) + \rho_g^2(n_g^2 - n_e^2)\hat{\Psi}_i(\rho_g)\hat{\Psi}_j(\rho_g)\right], \tag{D.2}$$

where the subscript $c$, $g$, and $e$ relate to the core, clad, and environment of the fiber, respectively.

# APPENDIX E CODING EXAMPLE FOR MODE PROPAGATION

To exemplify the computing capabilities of the library, Figure E.1 presents a Python script that simulates the propagation of two degenerated modes in a symmetrical 2x2 fiber coupler. In the code snippet, the workflow class is first employed to initialize the eigenmode expansion computation using the user-defined parameters. With the supermodes computed, the call to the *propagate_supermodes* method initiates the Runge-Kutta solver to compute the modes' amplitude along the longitudinal axis through the profile provided by the user.

```python
from SuPyMode.workflow import Workflow, fiber_catalogue, configuration, Boundaries2D, AlphaProfile

clad_structure = configuration.ring.FusedProfile_02x02

fiber0 = fiber_catalogue.SMF28(wavelength=1.55e-6)
fiber1 = fiber_catalogue.SMF28(wavelength=1.55e-6)

workflow = Workflow(
    fiber_list=[fiber0, fiber1],
    clad_structure=clad_structure,
    fusion_degree=0.90,
    wavelength=1.55e-6,
    resolution=200,
    x_bounds="left-centering",
    y_bounds="top-centering",
    boundaries=[
        Boundaries2D(right="symmetric", bottom='symmetric'),
        Boundaries2D(right="anti-symmetric", bottom='symmetric')
    ],
    generate_report=False,
    debug_mode=True,
    n_sorted_mode=6
)

profile = AlphaProfile()

profile.add_taper_segment(
    alpha=0,
    initial_heating_length=5e-3,
    stretching_length=2e-3,
)

profile.initialize()

amplitudes, z, _ = superset.propagate(
    profile=profile,
    initial_amplitude=[1, 0, 0, 0, 0, 0],
    add_coupling=True,
    max_step=superset.wavelength / 400,
)
```

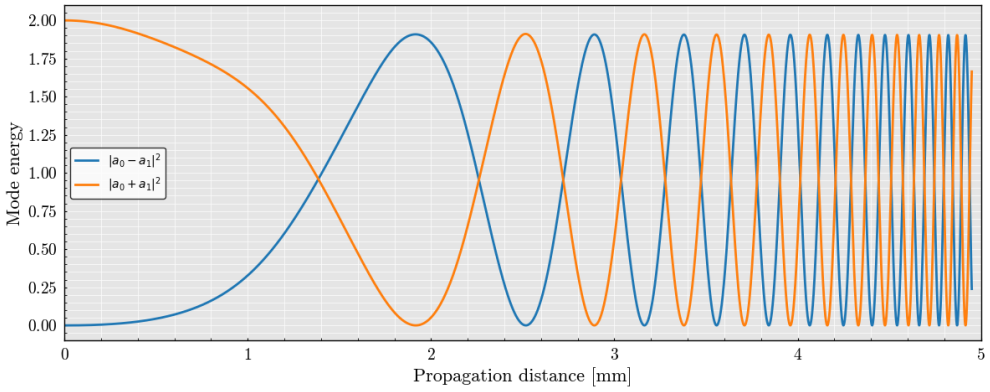



FIGURE E.1 SuPyMode code snippet and simulation for 2x2 coupler. The considered design employs two SMF28 fibers in a symmetrical (left-right) configuration. The boundary condition is defined such as to compute both symmetric and antisymmetric supermodes.